Prediction of Leaf Area Index using the Integration of the Thermal Infrared with Visible and Near-Infrared Data acquired with an UAV for a Mixed Forest

PHILIP STOBBELAAR
May, 2021

SUPERVISORS:
Dr. E. Neinavaz
Dr. P. Nyktas

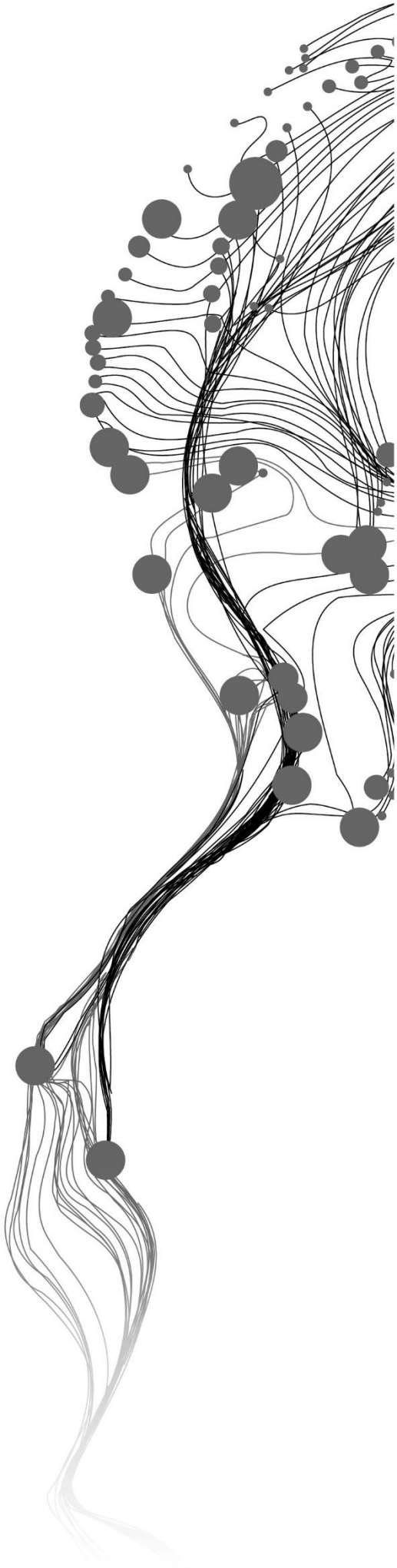

Prediction of Leaf Area Index using the Integration of the Thermal Infrared with Visible and Near-Infrared Data acquired with an UAV for a Mixed Forest

PHILIP STOBBELAAR
Enschede, The Netherlands, May, 2021

Thesis submitted to the Faculty of Geo-Information Science and Earth Observation of the University of Twente in partial fulfilment of the requirements for the degree of Master of Science in Geo-information Science and Earth Observation.
Specialization: Spatial Engineering

SUPERVISORS:
Dr. E. Neinavaz
Dr. P. Nyktas

THESIS ASSESSMENT BOARD:
Dr. R.G. Nijmeijer (Chair)

ABSTRACT

The leaf area index (LAI) is one of the most important biophysical variables, providing crucial information about vegetation and its processes. The LAI is invaluable for climate and biodiversity studies, being part of the essential climate variables (ECVs) as well as the remote-sensing-enabled essential biodiversity variables (RS-enabled EBVs), as it is needed for many environmental models and can be of use for stakeholders like agriculturalists, foresters, and ecologists. Due to its importance, it is essential to be able to accurately measure or predict the LAI. The most common methods make use of remote sensing, and so far, LAI has been successfully estimated using spectral reflectance in the visible and near-infrared (0.4 – 1.3 μm, VNIR) and the short wave infrared (1.4 – 3 μm, SWIR) domains. However, the possibility of using the characteristics of vegetation in the thermal infrared (3 – 14 μm, TIR) for LAI estimation has not been researched as much. With studies under laboratory settings proving that the TIR data can be of interest when predicting LAI on the canopy level, there is a need for research in other environments and different settings.

In this study, the prediction of LAI with the integration of VNIR and TIR data was investigated for a mixed forest, the Haagse Bos located in the North of Enschede, the Netherlands. During the field campaign in September 2021, in-situ LAI measurements were carried out. Simultaneously, VNIR and TIR images were captured by means of an unmanned aerial system (UAS). To assess the capabilities of integrating TIR with VNIR data for LAI prediction, land surface temperature (LST) and land surface emissivity (LSE) were calculated. For analysis using LST, data from two different separate flight heights of the UAS (85 m and 120 m) were used to assess the effect of altitude on the LAI prediction accuracy. LSE was calculated using the normalised difference vegetation index (NDVI) threshold method, which makes use of emissivity values for vegetation and bare soil, the NDVI, and the percentage of vegetation cover (P_V). P_V was taken from two different approaches, from in-situ data as well as from a canopy height model (CHM). The LAI prediction analysis was done by examining the relationship of LAI with nine different vegetation indices as well as with the use of partial least squares regression (PLSR). Analysis using vegetation indices as well as using PLSR was done by comparing the LAI prediction accuracy obtained using only VNIR reflectance spectra and when integrating the VNIR reflectance spectra with either LST or LSE.

The highest prediction accuracy obtained between LAI and VNIR data was (R^2 = 0.5815, RMSE = 0.6972) using reduced simple ratio (RSR) vegetation index. Prediction accuracy of LAI was not improved with the integration of LST and VNIR data using vegetation indices; however, it was increased when VNIR data integrated with LSE (RSR: R^2 = 0.7458, RMSE = 0.5081). The best result was obtained with LST integration with the VNIR reflectance spectra using PLSR with LST from the 85 m altitude (R^2 = 0.5565, $RMSE_{CV}$ = 0.7998). However, the integration of VNIR data with LSE significantly improved the results using PLSR (R^2 = 0.7907, $RMSE_{CV}$ = 0.8351). This indicates that LST is not beneficial for LAI prediction when integrating with reflectance spectra when using vegetation indices or PLSR.

Additional results also showed that differentiation of plots by dominant species could improve LAI prediction accuracy with PLSR, especially when integrating LSE with VNIR data. Th study confirms outcomes of previous research, stating that information of the TIR domain shows promising results when integrating with reflectance data to predict LAI. An important finding is that while LST is not suitable for improving the LAI prediction accuracy, LSE seems to be a beneficial addition. Consequently, further research should aim to increase the knowledge on the relationship between LAI and LSE, focusing on different approaches and different environments to fill the existing scientific gap.

ACKNOWLEDGEMENTS

Throughout the writing of this thesis, I got a lot of support and assistance. Working on this research project during a global pandemic was very challenging, and I couldn't have done it without having a great number of awesome people around me.

I would first like to thank my supervisors, Dr. Elnaz Neinavaz and Dr. Panagiotis Nyktas, whose expertise, constructive feedback, and constant words of encouragement were invaluable for my research. Our weekly meetings helped me greatly, I don't know where I would be without your input. I want to thank you both for your patient support and the opportunities you gave me. In times that I was worried about my progress, you were always very optimistic and pushed me in the right direction. From our meetings in person for my fieldwork to the countless video calls we had, I'm very grateful for all the help I got from you.

I would like to thank my parents, for their love and support. Although we couldn't see each other most of the time, our phone calls with updates from home were always a welcome part of my week. I know I can always count on you. Thank you to my lovely girlfriend Shih Ting, you were always there for me in this time, always so supportive and believing in me. I would also like to thank my good friend and roommate Martijn, you struggled together with me, had always an open ear for my problems and tried to help me find solutions. Of course, I also thank you for making sure that I had a lot of distraction from my work.

Finally, I would like to thank all my friends in Enschede who I could see at ITC as well as my friends back in Munich who I met virtually. With all the fun we had together this last year, I'm very grateful to have you all, you helped me stay sane, and I know I can always count on you.

TABLE OF CONTENTS

LIST OF FIGURES

LIST OF TABLES

1. INTRODUCTION

Although there is still too much denial by many individuals, there is a robust scientific consensus that the global climate is changing, and the earth is warming (Anderegg et al., 2010). Research to find causes and effects of anthropogenic climate change has come a long way, supported by numerous research studies and reports, as well as the International Panel on Climate Change (IPCC), which was set up by the United Nations and tries to combine all known facts on the matter in its synthesis reports which are created to provide policy makers with a comprehensive summary of all papers related to climate change (IPCC, n.d.). As a result of climate change, the biodiversity of many ecosystems is threatened (IPCC, 2014). To study the effects and causes of climate change, there is a need for global, harmonised observation to deliver regular, timely data on biodiversity change (Pereira et al., 2012).

In order to understand and predict the transformation of the climate, the Global Climate Observing System (GCOS) developed the concept of essential climate variables (ECVs) (Bojinski et al., 2014). The concept was defined because of the need for global observation of the climate, to be able to understand the changes in our climate, with datasets that are adhering to quality standards, are easy to interpret, and open source (Bojinski et al., 2014; Doherty et al., 2009; Shapiro et al., 2010). ECVs are physical, chemical, or biological variables, classified into atmospheric, oceanic, and terrestrial classes, and are identified based on the criteria of relevance, feasibility, and cost-effectiveness (Bojinski et al., 2014). Many studies presented in the IPCC make use of ECVs (Doherty et al., 2009). Due to the relevance of these variables for climate research, the ability to monitor them with high accuracy is of utmost importance. One of the terrestrial ECVs is the leaf area index (LAI). This research will focus on attempting to increase LAI prediction accuracy using remote sensing.

1.1. Leaf area index

The LAI is one of the most important vegetation biophysical variables in climate and biodiversity studies (Zheng and Moskal, 2009). It is a crucial input for forest ecosystem models, as it helps to estimate productivity and biomass, which are indicators of forest health (Pope and Treitz, 2013). For broadleaf canopies, LAI is a dimensionless variable and is defined as "the one-sided green leaf area per unit ground surface area (LAI = leaf area/ground area, m^2/m^2)" (Chen and Black, 1992; Watson and Watson, 1953). LAI provides information on how much area is available to plants for photosynthesis, as it can be assumed that their leaves contain chlorophyll. In addition to the information about the gas exchange, LAI can also inquire about evaporation, transpiration, carbon absorption and assimilation, and the interception of solar radiation, wind, and precipitation (Zheng and Moskal, 2009).

1.1.1. Leaf area index as an essential variable

Inspired by ECVs, the concept of essential biodiversity variables (EBVs) was developed to provide a globally harmonised observation system on biodiversity change (Pereira et al., 2013). To ensure continuous monitoring of forest health and biodiversity worldwide, specific vegetation parameters should be agreed on to use for models, and LAI is one of those (Skidmore and Pettorelli, 2015). When looking at

variables that can be used for climate and biodiversity assessments, it is hard to ignore the LAI, as it indicates radiation and precipitation interception, energy conversion, and water balance (Bréda, 2003; Zheng and Moskal, 2009), as well as key indicators of plant health (Zheng and Moskal, 2009). Also, yield and fertiliser efficiency are related to LAI (Addai and Alimiyawo, 2015), as well as the net primary production of ecosystems (Bonan, 1993; Matsushita et al., 2004). Therefore, LAI is on the list of variables suggested as remote sensing-enabled EBVs, which are relevant for satellite observation (Skidmore and Pettorelli, 2015). Besides, other EBVs, such as canopy chlorophyll content, were found to be spatially correlated to LAI values (Darvishzadeh et al., 2008). Stakeholders benefitting from the monitoring of LAI could be found everywhere; examples are farmers, foresters, ecologists, and climate or biophysical modellers (Bréda, 2003).

For observation and monitoring of many ecosystem structures and functions, LAI is indispensable (Asner et al., 2003). As the leaf area determines how much light or rain gets intercepted, it also stimulates the within- and below-canopy microclimates (Bréda, 2003; Zheng and Moskal, 2009). LAI is necessary as an input for many environmental models, as the exchange of energy and the gases carbon dioxide and oxygen between ecosystems and the atmosphere happens through the leaves (Song, 2013). As LAI is essential for many purposes, it is vital to be able to measure, calculate, and predict LAI on all possible scales with the highest accuracy. In this study, LAI was estimated using remote sensing data over the visible-near infrared (0.4 – 1.3 μm, VNIR) and thermal infrared (3 – 14 μm, TIR) domains by means of UAS (Unmanned Aerial System).

1.1.2. Methods to measure leaf area index

Given the theoretically simple calculation of the LAI, the area of vegetation divided by the area of associated background, it would be conceivable that the determination should not pose too many problems in practice. However, in reality, the procedure is more complicated because of its spatial (horizontal and vertical) and temporal variability as annual cycles and inter-annual variability interact with the structure, composition, and heterogeneity of plants (Bréda, 2003).

Methods for estimating the LAI can be divided into destructive and non-destructive methods. In destructive methods, the area of the leaves is measured directly after cutting the plant or calculated with a ratio of a parameter with the help of a coefficient (Bréda, 2003). Destructive methods are the most accurate ones and, therefore, suitable for the calibration, evaluation, and validation of indirect methods because they relate directly to the leaf area and thus reflect the actual leaf area index (Bréda, 2003). Non-destructive methods derive the LAI from radiation measurements from the vegetation using the radiation transfer theory (Anderson, 1971; Ross, 1981). These methods make use of statistical and probabilistic approaches to the distribution and pattern of leaf elements in the vegetation (Jones, 1992). Although errors will arise if a parameter is measured indirectly, these methods are popular because of their speed and simplicity, and their results are reliable (Danner et al., 2015).

Collecting LAI in-situ data, whether destructive or non-destructive, is laborious, time-consuming, and not suitable for large areas (Zheng and Moskal, 2009). For large areas, remote sensing approaches are essential for the estimation of the LAI. With the help of satellite imagery, air-borne sensors, and UAS, the retrieval of the LAI from remote sensing data is probably the only feasible method for large areas (Song, 2013).

So far, the prediction of the LAI utilizing remote sensing has been addressed excessively (Brown et al., 2000; Chang et al., 2019; Darvishzadeh et al., 2008; Pope and Treitz, 2013; Song, 2013; Zheng and Moskal, 2009). This includes VNIR and short-wave infrared (1.4 – 3 μm, SWIR) data. The physiological and structural properties of leaves determine their naturally low reflectivity for the visible (0.4 – 0.7 μm, VIS) wavelengths, except for green light. In addition to the VIS domain, a high reflectivity of the vegetation in the near-infrared (0.7 – 1.4 μm, NIR) enables remote sensing to capture detailed information about the living, photosynthetically active plant populations and thus helps to understand the exchange between plant ecosystems and the atmosphere (Zheng and Moskal, 2009). Differences in spectral reflectance of vegetation with changing values of the LAI are not prominent in the VIS but show variations in the NIR, and the SWIR, with maximum values and differences in the NIR (Asner, 1998; Darvishzadeh et al., 2008).

There are multiple approaches to estimate LAI through the vegetation spectral information using remote sensing data (Zheng and Moskal, 2009). These include the use of vegetation indices, regression models, physical models, and artificial neural networks. A limiting factor for the estimation of LAI through vegetation indices using remote sensing data can be spectral saturation at high LAI values (Chen and Cihlar, 1996; Gower et al., 1999). With high LAI values, canopy reflectance is strongly influenced by leaf optical properties, and LAI increases cannot be detected anymore (Asner, 1998).

1.2. Thermal infrared

1.2.1. Thermal infrared remote sensing

Another method to predict LAI is the use of TIR remote sensing data (Neinavaz et al., 2019, 2016a, 2016b). TIR remote sensing data uses the radiation emitted by objects in the TIR range of the electromagnetic spectrum (Prakash, 2000). According to Planck's law, every object with a temperature above 0 Kelvin emits electromagnetic radiation; Wien's law states that with increasing temperature, the intensity of the radiation emitted increases. Most objects on earth (e.g., vegetation, soil, water, people) emit TIR radiation in the spectral range of 3 – 14 μm (Jensen, 2009).

As spectral information in the TIR region mainly consists of radiative emission of objects rather than reflection (Neinavaz et al., 2016a), TIR data can be acquired at any time of the day. The atmosphere is mostly transparent for the TIR wavelengths as it offers a large atmospheric window (Clerbaux et al., 2011); however, atmospheric correction still has to be performed using radiative transfer models with atmospheric profiles to reduce the effects of absorption, emission, and scattering by particles in the atmosphere (Meier et al., 2011). At very low altitude acquisitions, the atmospheric effects can be avoided (Messina and Modica, 2020), benefitting remote sensing using UAS.

TIR data has great potential in illuminating biophysical and biochemical characteristics of vegetation (Ullah, 2013). Primary absorption features and leaf structure parameters can be observed in TIR regions (Ribeiro da Luz, 2006). Through different spectral features in the TIR domain, plant species can be distinguished (Ribeiro da Luz and Crowley, 2010). Especially at the canopy level, there is scarce information available regarding the emissivity of vegetation in the TIR domain (Neinavaz, 2017). The reason for this is mainly technical. Sensors operating in the TIR domain must be able to capture the relatively low variance in emissivity values of plants (Neinavaz et al., 2016a; Ribeiro da Luz and Crowley, 2007). For accurate TIR measurements, sensors with a high signal to noise ratio are required (Kirkland et al., 2002; Ribeiro da Luz and Crowley, 2010). Furthermore, the knowledge about spectral features of

plants in connection with plant physiology and organic chemistry lacks for many researchers in the TIR region (Quattrochi and Luvall, 1999). Especially with satellite data, TIR data mostly has a relatively coarse spatial resolution (Neinavaz, 2017; Quattrochi and Luvall, 1999).

The energy leaves receive from the incident solar radiation is distributed over three different outputs: the reflection of incoming radiation, evapotranspiration, and heat (Gates, 1980). Most of the incoming energy is transferred to heat (McKinney and Schoch, 2003), and as heat is seen as radiation in the TIR domain, part of the energy of leaves can be detected with TIR data. The temperature of leaves is mainly regulated through transpiration (Drake et al., 1970), and there is a nearly linear relation between transpiration and leaf area (Vertessy et al., 1995). Analogous, also evaporation is linked to leaf area (van den Hurk et al., 2003). The more leaf area is available for a plant, the more it can regulate its temperature over the leaf surface. Therefore, through heat regulation, a correlation between thermal emissivity values and leaf area can be seen.

Most studies that use TIR data for vegetation studies concentrate on the calculation of land surface temperature (LST) and land surface emissivity (LSE) (Gomis-Cebolla et al., 2018; Göttsche and Hulley, 2012; Jacob et al., 2017; Jiménez-Muñoz et al., 2006; Li et al., 2013a). LST is the radiative skin temperature of the land surface and gives information about physical processes of surface energy (Li et al., 2013a). LSE shows the percentage of radiation that is emitted by an element on the land surface in the TIR domain and is a measure of the radiant energy of the surface (Sobrino et al., 2001). With an increasing amount of vegetation, LSE also increases, a positive correlation between LSE and the normalized difference vegetation index (NDVI) has been found (Sobrino et al., 2008). Between LST and NDVI, there is a weak negative correlation (Kumar and Shekhar, 2015; Zhang et al., 2009).

1.2.2. Applying thermal infrared data for leaf area index estimation

The possibilities of the estimation of LAI with the TIR data is not yet fully explored (Neinavaz et al., 2019, 2016a, 2016b), at least not as much as with VNIR/SWIR data. Estimating the LAI using TIR data has been carried out under controlled laboratory conditions (Neinavaz et al., 2016a, 2016b) and in the mixed temperate forest on landscape-level utilizing Landsat-8 image (Neinavaz et al., 2019). The research was done on the relation between LAI and LSE as well as LST. Research in the controlled environment shows that with increasing LAI, the emissivity over the TIR domain rises (Neinavaz et al., 2016b). Also, with similar LAI values, different species could be distinguished by their TIR emissivity spectra (Neinavaz et al., 2016b). The relation between LAI and LSE was found to be much stronger than between LAI and LST (Neinavaz et al., 2019). This research also focuses on the relation of LST and LSE with LAI and how the integration of these variables can increase the accuracy in LAI prediction.

A significant advantage of the TIR compared to VNIR/SWIR data when looking at LAI estimation is the lack of saturation that occurs with VNIR/SWIR data for high LAI values; saturation in the TIR region happens at higher LAI values under laboratory conditions (Neinavaz et al., 2016b). Prediction accuracy of the LAI can be improved by integrating the TIR and VNIR/SWIR data (Neinavaz et al., 2019); however, this requires to be investigated thoroughly in various ecosystems using different platforms (Neinavaz et al., 2019). This knowledge gap will be addressed in this study.

1.3. Unmanned aerial systems

In recent years, thermal imaging using UAS has improved due to the development of smaller thermal sensors and unmanned aerial vehicles (UAV) technology (Chen et al., 2016; Colomina and Molina, 2014). UAS are defined by the Federal Aviation Administration (FAA) as pilotless aircraft (Chen et al., 2016). While thermal remote sensing using UAS was first used for military purposes (Kostrzewa et al., 2003), it has found its way towards more common uses like forest fire detection, as well as scientific uses (Rufino and Moccia, 2005; Scholtz et al., 2011).

Remote sensing data is mainly obtained using satellites, air-borne, and UAV platforms on which different sensors can be mounted. A UAS consists of three components; the UAV, the ground control station, and the control system that links and communicates between them (Colomina and Molina, 2014). Although acquiring satellite images is the easiest option, UAS data is often more suitable to the user, as the sensors and the time of flight can be chosen regarding the needs of the research and repeated when and how often as desired for smaller areas (Mitchard, 2016). In comparison to the use of manned aircraft, UAS have the considerable benefit of being less expensive. Advantages of UAS are that various sensors can be switched quickly and even mounted simultaneously, leading to the possibility of quick, inexpensive, and reliable acquirement of high-resolution data for the multitemporal assessment of parameters in different ecosystems (Lausch et al., 2017; Maes et al., 2017). The most prominent advantage of UAS compared to spaceborne platforms is the high spatial resolution, which is possible due to the low altitude.

Restraints of UAS are their limited battery life, leading to short flights, as well as their payload (Maes et al., 2017). Hyperspectral, cooled TIR cameras provide the highest radiometric accuracy (Boubanga-Tombet et al., 2019); however, they are heavy, costly, and consume a lot of power (Döpper et al., 2020). Until recently, only uncooled TIR cameras could be mounted on a UAS (Jensen et al., 2014), leading to more noise and, therefore, less sensitivity (Luhmann et al., 2013). Countering this downside, however, is the low flight altitude of UAS (Kuenzer and Dech, 2013). This is because noise mainly results from atmospheric absorption and emission effects, minimalised with low-altitude measurements (Messina and Modica, 2020).

In recent years, with the advance of UAS technology and their more general availability, research has also been conducted to retrieve LAI with the use of UAS (Chang et al., 2019; Fumera, 2020; Guo et al., 2018; Kanning et al., 2018; Li et al., 2019; D. Zhang et al., 2019; W. Zhu et al., 2019a; X. Zhu et al., 2019a). Most of these studies were performed for the agricultural area, and only a few studies have been addressed the LAI retrieval for forest ecosystem using UAS (Comba et al., 2020; Duan et al., 2019; W. Zhu et al., 2019b; Zhu et al., 2018; X. Zhu et al., 2019b). Regarding TIR technology and UAS, applications concern mostly the detection of crop water stress, identifying drainage networks in fields, identification of pathology symptoms, monitoring, and yield estimation in agricultural uses (Messina and Modica, 2020). In forest environments, UAS with TIR sensors have been used to get information about wildfires (Valero et al., 2017). No research yet has been done to estimate LAI using UAS with the integration of the VNIR and TIR data, neither for agricultural nor forest areas. Using a thermal sensor together with a multispectral sensor and fusing their data can be beneficial and help to inquire knowledge for different field of studies (Messina and Modica, 2020; J. Zhang et al., 2019).

1.4. Definition of the research problem

As mentioned before, LAI is one of the most important vegetation biophysical variables and is needed as an input for most biodiversity and climate models. There are already various approaches for the estimation of the LAI. Estimating the LAI with TIR data can help to understand the link between canopy emissivity spectra and the processes that are related to the leaf area. Only recently, some research has been done to investigate the integration of the VNIR and TIR remote sensing data to predict LAI. It was concluded that it is possible to use TIR data to enhance the prediction accuracy of LAI; however, the estimation of LAI by means of TIR and VNIR data using a UAS platform had not yet been addressed for a forest environment.

1.5. Analysis of the research problem with regard to the wicked problem framework

In accordance with the wicked problem framework (Georgiadou and Reckien, 2018; Hoppe, 2010) (Table 1), the problem of this research can be classified as a moderately structured problem. In the past, there was disagreement between researchers on the usability of TIR data for vegetation studies, as the unavailability of applicable devices with high signal to noise performance and the complexity of spectral features of vegetation led to misinterpretations (Kirkland et al., 2002; Ribeiro da Luz and Crowley, 2010; Ullah et al., 2012). An example of contrary findings in the research field of TIR data for vegetation studies can be seen at the beginnings of TIR data research. It was stated that upper and lower leaf surfaces, as well as young and old leaves, could be distinguished when looking at TIR reflectance spectra (Gates and Tantraporn, 1952), while other research showed that they could not be distinguished (Wong and Blevin, 1967), leading to the initial belief that vegetation is featureless in the TIR domain. The disagreement in the recent decades about the characteristics of plants in the TIR domain by different researchers may lead to the conclusion that there was indeed a wicked problem, with unknown facts and dissensus among stakeholders when the different researchers can be classified as stakeholders. A wicked problem was defined as much-debated political issues with disagreement concerning ethics and divided stakeholders' preferences, while knowledge about the issues at hand is uncertain (Georgiadou and Reckien, 2018). In this study, however, the problem focuses only on scientific research, without political or ethical issues. In that case, it is not a problem to do further research in the case that there is disagreement on results, it is encouraged; therefore, the problem can only be classified as a moderately structured one, with uncertainty of the facts.

When looking at the stakeholders who can benefit from an accurately predictable LAI, such as farmers, foresters, ecologists, and climate or biophysical modellers, it is clear that there is no dissensus. As there is no adverse effect of being able to predict the LAI, there is no stakeholder who would see the outcome of this research as unfavourable. However, there is still uncertainty regarding the facts, concretely regarding how TIR data can increase the prediction accuracy. Since so far, only a few studies included the TIR domain in vegetation studies, there is not yet enough information available on how the inclusion of TIR data can benefit measurements of plant characteristics like LAI. There is a need for further research to be able to increase the knowledge that is available in this topic in order to make the problem a tame and structured one. With plenty of available insight, the stakeholders can apply the methods that have been researched. In this research, the outcome will increase the knowledge that is available on TIR data and how it can be applied. Using two different methods to approach the goal of the research, predicting LAI with the integration of TIR and VNIR data using vegetation indices and partial least squares regression, this research contributes towards the goal of developing methods and approaches for the relevant stakeholders to use.

Table 1: The wicked problem framework as adapted by Georgiadou & Reckien (2018) from Hoppe (2010)

Spatial Knowledge	Policy Goals and Values	
	Consensus among Stakeholders	**Dissensus among Stakeholders**
Certain (facts and cause-effects)	Tame or structured problems ▪ Debate on technicalities ▪ Geo-information tools as a *problem solver*	Moderately structured problems ▪ Participation to debate goals and values ▪ Geo-information tools as a *mediator*
Uncertain (facts and cause-effects)	Moderately structured problems ▪ Participation in debating cause-effects and optimizing the collection of facts ▪ Geo-information tools as *analyst* and/or *advocate*	Wicked or unstructured problems ▪ Endless debate ▪ Geo-information tools as *problem recognizer*

1.6. Research objectives

The overall research objective of the thesis is to assess the possibilities of integrating UAS-obtained TIR and VNIR remote sensing data to estimate the LAI for a mixed forest. The research aims to compare the prediction accuracy of LAI obtained from UAS using different methods, namely vegetation indices and partial least squares regression.

Additional research objectives are:

- Assess the prediction accuracy of the LAI for a mixed forest with the integration of UAS-obtained TIR and VNIR data applying vegetation indices.
- Assess the prediction accuracy of the LAI for a mixed forest using the integration of UAS-obtained TIR and VNIR data using partial least squares regression analysis.
- Assess the effect of UAS-TIR data acquisition at different flight heights and compare the prediction accuracy of the LAI for a mixed forest with the UAS-TIR data from both flight heights.

1.7. Research questions

To evaluate the results of this research based on the research objectives, the following research questions were developed:

- How will the prediction accuracy of the LAI be increased for a mixed forest with the integration of UAS-obtained TIR and VNIR data applying vegetation indices, compared to utilizing only VNIR data?
- How will the prediction accuracy of the LAI be increased for a mixed forest with the integration of UAS-obtained TIR and VNIR data applying partial least squares regression, compared to utilizing only VNIR data?
- What are the effects on the prediction accuracy of the LAI of different flight heights of the UAS for TIR data acquisition for the mixed forest using UAS-TIR data?

2. METHODOLOGY

2.1. General description of the study area

Field measurements were carried out over the area named "Haagse Bos", which is located among the cities of Enschede, Oldenzaal, and Losser, in the province of Overijssel, the Netherlands (Figure 1). The study area used to be a production forest and has an approximate area of 52 ha (calculated using ArcGIS), and is under the management of the "Natuurmonumenten", a Dutch nature conservation organization, the Netherlands.

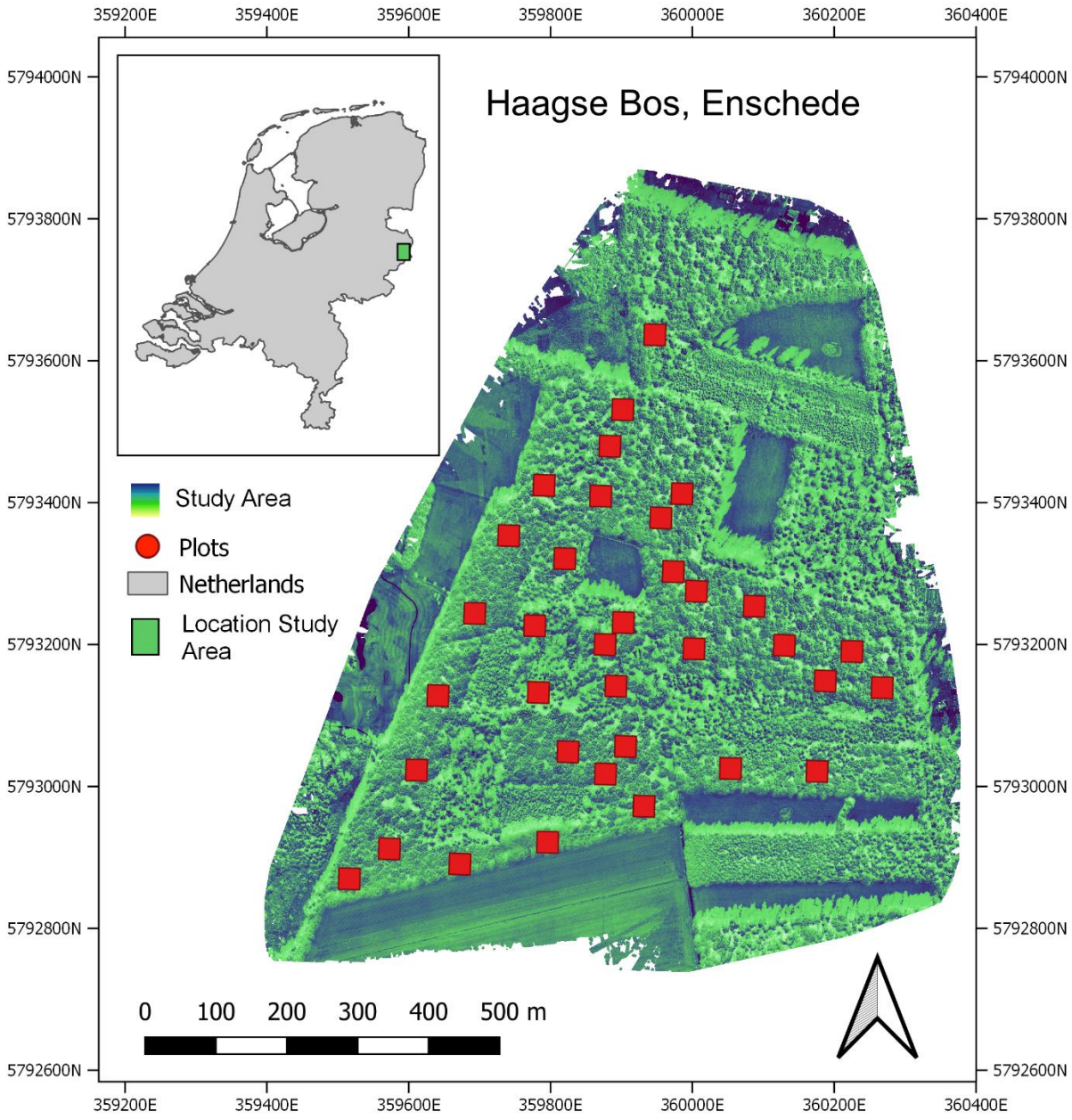

Figure 1: Outline of the study area, with plots for which in-situ data was collected.

Haagse Bos is a mixed vegetation forest with broadleaf and coniferous tree species. Different species that exist in the forest including Scot pine (*Pinus sylvestris*), Douglus fir (*Pseudotsuga menziesii*), Norway spruce (*Picea abies*), European larch (*Larix decidua*), European beech (*Fagus sylavatica*), Oak (*Quercus robur*), European white birch (*Betula pendula*), and Alder (*Alnus)*, as well as broadleaved trees are dominating the forest (Eshetae, 2020). The climate in the area is warm and moderate, with an average annual temperature of 9.1°C and 782 mm of rainfall per year (Climate-Data.org, n.d.). In September 2020, when fieldwork was conducted, the average temperature was 14.5°C, the average amount of rainfall was 48 mm (KNMI, 2021).

2.2. Data acquisition

The field campaign was conducted in September 2020. In this study, the non-destructive method was used to collect LAI data. The ground measurements were carried out from 7th till 17th of September 2020, and UAS flight campaigns for collecting the TIR and multispectral images were executed on September 11th and September 14th, respectively. The random sampling strategy was adopted with the consideration of the accessibility of the plots. Consequently, 35 plots of 30 by 30 m were selected, resulting in 20 plots dominated by beech, 13 plots by oak, and two plots by Fir. Unfortunately, TIR images could only be acquired for 30 plots. Therefore the analysis to predict LAI was performed only with the data for these 30 plots, even when only using reflectance spectra, to allow for comparison of the different methods that are used.

Figure 2: Below-canopy measurement of LAI using the LICOR 2200C.

2.2.1. In-situ measurement of the leaf area index

The centre position of each plot was delineated using a compass and measuring tape, and further was recorded using a GNSS LEICA C15 -Leica (i.e., Global Navigation Satellite System). For each plot, existing species were recorded, and dominant species was determined. The structural forest parameters,

including LAI, number of trees, and the presence of understory or dead wood of the plot, were noted. LAI was measured with the LICOR 2200C plant canopy analyser (LICOR Inc., Lincoln, NE, USA) (Figure 3). The LICOR uses radiation measurements taken with a 148° fisheye sensor (Figure 4). Radiation measurements were carried out above and below the vegetation cover to determine the light transmission from five angles (LI-COR, 2019). The LAI is inferred indirectly through a simple light interception model by inversion of the so-called gap fraction (LI-COR, 2019). If the radiation of the incident light is measured below or within a plant stand, the gap fraction is the portion that is not absorbed by the vegetation and reaches the sensor. Through inversion, the part absorbed by the plant parts is deduced; it is proportional to the area occupied by the leaves (LI-COR, 2019).
In addition to the LAI, the LICOR also measured the diffuse non-interceptive value (DIFN), which indicates the fraction of the sky that is not blocked by foliage (LI-COR, 2019) and is, therefore, the inverse of the percentage of vegetation cover (P_V).

Figure 3: The LICOR 2200C plant canopy analyser (©LICOR Inc.).

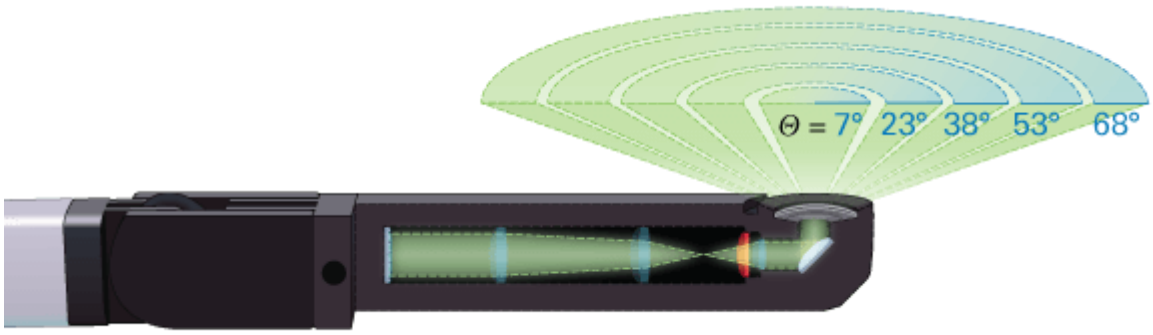

Figure 4: Cross-section of the LICOR 2200C, showing the five concentric rings at different zenith angles for which radiation measurements are detected by the sensor (©LICOR Inc.).

To quantify the LAI for each plot, a total of nine radiation measurements were taken with the LICOR. To prevent direct sunlight from reaching the sensor, a diffuser cap was used. This diffuser cap allows the

sensor to view an angle of 45° (Figure 5). Four reference samples of the above canopy measurements were taken at an open area close to the plot, and five below-canopy measurements, taken at the centre and the corners of the plot, facing inwards. From these nine readings, the LICOR computes the average LAI of the plot.

Figure 5: View of the LICOR 2200C sensor with a 45° diffuser cap (©LICOR Inc.).

2.2.2. Using the unmanned aerial system

For all UAS flights, the UAV used to mount the different sensors was the DJI Phantom 4 (Figure 6). The UAV was manufactured by DJI (Shenzen, China), weighs 1380 gr, and is equipped with a 12.4 Megapixel RGB camera. The creation of flight plans and the control of the UAV during the flight was done with UgCS 4.0 (i.e., Universal ground Control Software) drone control software (i.e., SPH Engineering, Latvia). The horizontal hover accuracy range of the UAV with GPS positioning is ±1.5 m (DJI, n.d.). Both the thermal and the multispectral camera were mounted on the bottom of the UAV facing directly downwards, connected by cable to the Flight Controller for electricity.

Figure 6: The UAV used for the flights, the DJI Phantom 4 (©DJI).

For capturing the multispectral images, the UAS flew across the whole study area, capturing a total of 17344 images, which could then be stitched together to create orthomosaics and reflectance maps using Pix4d, a photogrammetry software by Pix4d S.A. (Prilly, Switzerland). Due to the high battery consumption of the FLIR camera, which prevents long flights, and the inability of Pix4d to generate orthomosaics of good quality from images captured by the FLIR, TIR images were only captured while hovering over the plots.

2.2.3. Thermal infrared image collection with the FLIR Vue Pro R

The TIR images were gathered with the FLIR Vue Pro R camera (Figure 7), designed for UAV integration and data collection. The camera uses an uncooled V0x Microbolometer sensor, which has a spectral range from 7.5 – 13.5 μm and an image size of 640 x 512 pixels. The camera has a weight of 113.4 gr and is manufactured by FLIR Systems, Inc. (Wilsonville, OR, USA). The model used in this study is equipped with a 19 mm lens with a field of view of 32° x 26° and is focused on infinity (FLIR Systems Inc, 2016). The FLIR camera calculates the absolute land surface temperature (LST), saved in 14-bit tiff-files with a scale factor as a digital number (DN). The measurement accuracy is given with ± 5°C (FLIR Systems Inc, 2016). This introduces insecurity into the dataset; however, with all TIR images being collected on the same day, the error affects all measurements similarly. The values for the different plots are therefore comparable.

Figure 7: The FLIR Vue Pro R thermal camera (©FLIR Systems Inc.).

As it was desired to create stable images, the UAV flew at a desired height, and move from plot to plot, and then only take images above the plots while hovering. Two different flight heights, 85 m and 120 m above ground were used to capture TIR images. (Figure 8). For both flight altitudes, the plots in the study area were covered by three flights, and multiple images were taken per plot. Although the UAV flight plan covered all 35 plots for which data collection was done, images were only created for 30 plots.

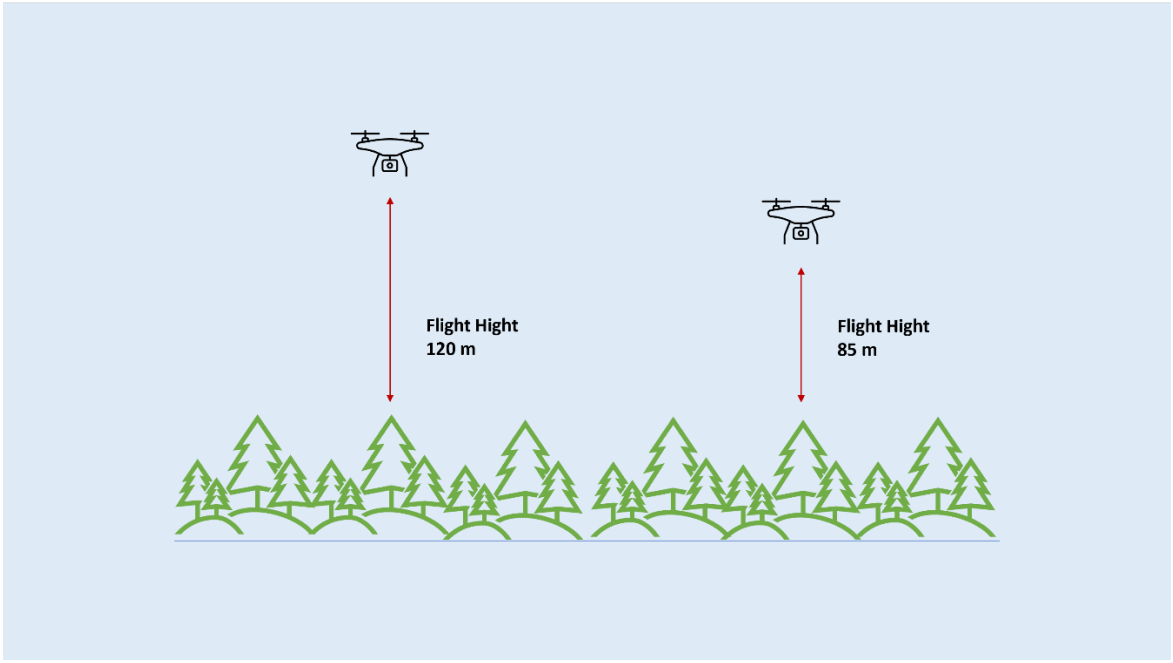

Figure 8: Visualisation of the different flight heights (i.e., 120 and 80 m) for image acquisition by the UAS for TIR data.

2.2.4. Visible and near-infrared image collection with the Parrot Sequoia

The multispectral camera mounted on the UAV to capture reflectance in the VNIR region of the electromagnetic spectrum was a Parrot Sequoia, manufactured by Parrot Drones SAS (Paris, France), which includes a 16 Megapixel RGB sensor as well as four 1.2 Megapixel monochrome sensors for the four different spectral bands: green (0.55 µm), red (0.66 µm), red-edge (0.735 µm), and NIR (0.79 µm). The red-edge band has a 0.01 µm bandwidth, whilst the other three bands have a bandwidth of 0.04 µm. For the multispectral sensors, the image size is 1280 x 960 pixels, and the focal length is 3.98 mm. The Parrot Sequoia weighs 72 g (Cowley et al., 2017).

With the Parrot Sequoia, it is possible to take multiple high-quality images while the UAV is flying. Therefore, the flights were planned to span the complete study area to create reflectance maps for all spectral bands for the whole area. The flight height was 120 m above the ground, flight speed was 6.5 m/s, and images were taken every 1.5 seconds. Images were recorded as 16-bit TIFF files as well as JPG files. Before every flight, images of calibration panels were taken to be able to create accurate reflection maps.

Figure 9: The Parrot Sequoia multispectral camera, with an indication of its five different sensors (©HORUS Dynamics).

2.3. Unmanned aerial vehicle image pre-processing

With the coordinates measured with the GNSS, a map of all plots was created in ArcGIS (Redlands, CA, USA) (Figure 1). As the coordinates show only the centre of every plot, the outline had to be created by first making a buffer with a radius of 15 m around the centre point and then laying a north-facing square around it. These squares now show the outline of all plots in the study area and are used to extract values per plot.

Using Pix4d, the images from the Parrot Sequoia multispectral sensor were stitched together to create reflectance maps for all four spectral bands. The reflectance maps were created using values for calibration from the calibration panels. The stitching process included matching key points from images together, creating a point cloud, orthomosaics (Figure 10), and reflectance maps. For the analysis, calculations were done with the complete reflectance maps and the average reflectance values per plot, which were extracted by calculating zonal statistics using ArcGIS.

2.3.1. Image quality assessment and pre-processing of thermal images

Multiple thermal images were captured for every plot during the flight campaign. For each plot, all images were visually analysed and compared to each other. The sharpest image with the best overlap with the obtained multispectral images of the corresponding plot was selected for further analysis. This was done for both flight altitudes. Due to the spatial resolution, the images captured with the FLIR camera show an area of 53.1 by 41.5 m for the flight height of 85 m and an area of 75 by 58.5 m for the flight height of 120 m. Therefore, the plots of 30 by 30 m needed to be clipped from the images. Using trigonometric equations, the pixels that needed to be cut away were calculated, and ArcGIS was used to extract the plots from the images to assure a good overlay of all used data.

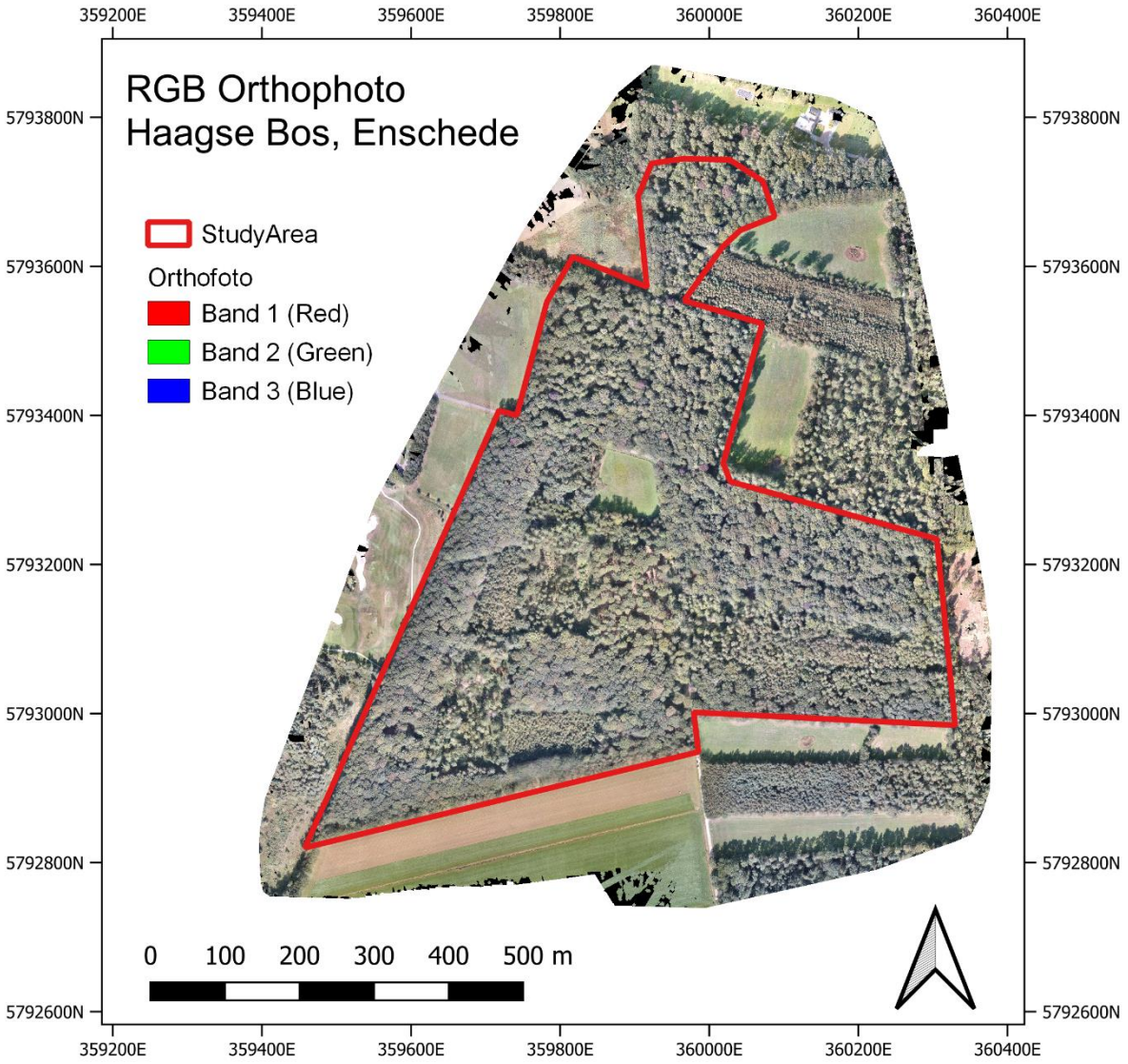

Figure 10: RGB-orthophoto created with Pix4d from Parrot Sequoia images.

2.3.2. Estimation of land surface temperature

The images recorded by the FLIR Vue Pro in the tiff file format show the data in the TIR domain as a digital number (DN) for every pixel. The DN is an expression of the temperature that is measured by the sensor, stored with a scale factor. The temperature that is calculated by the camera is dependent on radiometric settings like target emissivity or background temperature. The DN can be converted to the land surface temperature (LST) in °C by the following formula (FLIR Systems Inc, 2021):

$$LST = 0.04 * DN - 273.15 \quad (1)$$

Using the raster calculator in ArcGIS, LST was then calculated for these selected TIR images. For both flight heights, the average LST value for each plot was extracted.

2.3.3. Estimation of land surface emissivity

While LST from the FLIR Vue Pro is determined assuming a constant emissivity value for the whole study area, the land surface emissivity (LSE) varies for heterogeneous surfaces (Li et al., 2013b) and can also differ depending on the type of vegetation (French et al., 2000; Ribeiro da Luz and Crowley, 2007; Ullah et al., 2012). The prediction accuracy for the LAI can be improved when including LSE instead of LST (Neinavaz et al., 2020, 2019). Therefore, another approach used in this study to improve LAI prediction accuracy is to combine LSE with VNIR reflectance spectra.

The simplest way to calculate LSE is by using the popular NDVI-threshold method (Sobrino and Raissouni, 2000; Valor, 1996; Van De Griend and Owe, 1993). The method uses three different equations, depending on the NDVI, which indicates if a pixel is either fully vegetated, fully soil, or part vegetation part soil. For this, NDVI-thresholds are used that dictate which equation should be used to calculate LSE. The equations for calculation of LSE with the NDVI-threshold method are below (equation 2).

Calculation of LSE was done with MATLAB (version R2020b Update 3). Most studies applied the global NDVI-threshold value for fully vegetated pixels of 0.5 ($NDVI_V$) (Oltra-Carrió et al., 2012; Sobrino et al., 2008; Sobrino and Raissouni, 2000). However, in another study using multispectral images obtained by UAS, a value of 0.9 considered for $NDVI_V$; the used threshold value depends on the type of vegetation and study area and has to be evaluated before calculating LSE (Heinemann et al., 2020). The $NDVI_V$ is chosen by using a sample of pixels that are known to be completely vegetated and taking the average NDVI value of it. The same approach was used in this research, and an $NDVI_V$ threshold of 0.89 was found. For full soil pixels, the global NDVI-threshold for soil ($NDVI_S$) of 0.2 (Sobrino et al., 2008) was used. For the calculation of LSE this was not relevant, as none of the plots had pixels with NDVI values below 0.5.

$$LSE = \begin{cases} NDVI < NDVIs & a_\lambda + b_\lambda \rho_{red} \quad (2a) \\ NDVI \geq NDVIv & \varepsilon_{V\lambda} + d_\varepsilon \quad (2b) \\ NDVIs \leq NDVI \leq NDVIs & \varepsilon_{V\lambda} P_V + \varepsilon_{S\lambda} \times (1 - P_V) + d_\varepsilon \quad (2c) \end{cases}$$

In the equations, a_λ and b_λ are channel-dependent regression coefficients, ρ_{red} is the reflectance value of the red band for bare soil, ε_V and ε_S are the emissivity values of vegetation and bare soil in the TIR region, and P_V is the percentage of vegetation cover. The emissivity values for soil and vegetation used to calculate LSE are extracted from the ECOSTRESS spectral library from the California Institute of Technology (Baldridge et al., 2008; Meerdink et al., 2019). d_ε stands as the cavity effect, which can be calculated using the following equation:

$$d_\varepsilon = (1 - \varepsilon_S)(1 - P_V) F \varepsilon_V \quad (3)$$

F is a shape factor, which is assumed to be 0.55, due to diverse geometrical distributions (Sobrino et al., 2004, 1990).

Calculating LSE using the NDVI-threshold method does not only depend on the NDVI-threshold and emissivity values but is also influenced by P_V. In this research, P_V was calculated using two different approaches as follows:

1. P_V is derived from the DIFN measured with the LICOR 2200C during field work. This approach was used because it provides the most accurate value for P_V, as it is measured simultaneously with the LAI.
2. P_V is derived from the amount of vegetation with a canopy height above 15 m, calculated using a Canopy Height Model (CHM). The CHM was created by Luis Figueroa from a point cloud during the stitching process of the VNIR images from the Parrot Sequoia using Pix4d. A value of 15 m was chosen as the threshold for canopy height, as LAI measurements in the field only take the higher canopy into account, disregarding the undergrowth. This approach was used in order to get a value for P_V independent of in-situ measurements.

Using these different approaches to calculate P_V resulted in different values of LSE for every plot: Hereafter, LSE calculated using P_V from DIFN and LSE calculated using P_V from the CHM refer as LSE_{LICOR} and $LSE_{CHM,}$ respectively.

2.4. Estimation of leaf area index

As discussed before, the aim of this study is that whether the combination of the TIR data with VNIR reflectance spectra can improve the prediction accuracy, including the prediction using vegetation indices, as well as the prediction using partial least squares regression (PLSR). To observe an effect, the prediction accuracy including TIR data was compared to the prediction accuracy without it. Therefore, in both approaches, LAI is first estimated using only the reflectance values from the multispectral data and afterwards with both reflectance spectra and LST or LSE. LAI estimation including LST is done for the two datasets from the different flight altitudes.

2.4.1. Leaf area index prediction using vegetation indices

So far, LAI has been successfully predicted in many studies using vegetation indices (Brown, 2000; Huete et al., 2002; Jiang et al., 2008; Stenberg et al., 2004; Xue and Su, 2017). In this study, the most applied vegetation indices considered to be used to estimate LAI successfully are investigated. Due to the availability of reflectance values from four multispectral bands as well as LST and LSE derived from the TIR images, it was decided to use vegetation indices using two as well as three bands. Table 2 shows an overview of the indices used.

The indices using two bands as well as three bands (i.e., RSR) are indices that already have been used by Neinavaz et al. (2019). The other three-band indices, ASR and ANDVI, respectively, were created in this research experimentally. Somvanshi & Kumari (2020) highlighted that indices including a third band can benefit through atmospheric correction, such as is included with indices like the Atmospherically Resistant Vegetation Index (ARVI) and the Enhanced Vegetation Index (EVI). With results improving when including information from a third band in the indices SR and NDVI, it was decided to create the indices ASR and ANDVI.

For all nine vegetation indices shown in Table 2, all possible combinations of the VNIR reflectance spectra were calculated. The resulting maps showed the values of the vegetation indices for the whole study area; the average value per plot was extracted by calculating zonal statistics. Afterwards, the relationship between each vegetation index and corresponding measured LAI has been examined.

Table 2: Vegetation Indices considered in this research

Vegetation Index	Abbreviation	Original Equation	Equation	Reference
Simple Ratio	SR	$*\frac{\rho_{NIR}}{\rho_{Red}}$	$**\frac{\rho_{\lambda1}}{\rho_{\lambda2}}$	(Jordan, 1969)
Modified Simple Ratio	MSR	$\frac{\rho_{NIR}-\rho_{Red}-1}{(\rho_{NIR}/\rho_{Red})^{0.5}+1}$	$\frac{\rho_{\lambda1}-\rho_{\lambda2}-1}{(\rho_{\lambda1}/\rho_{\lambda2})^{0.5}+1}$	(Chen, 1996)
Difference Vegetation Index	SD	$\rho_{NIR}-\rho_{Red}$	$\rho_{\lambda1}-\rho_{\lambda2}$	(Tucker, 1979)
Renormalized Difference Index	RDI	$\frac{\rho_{NIR}-\rho_{Red}}{\sqrt{\rho_{NIR}+\rho_{Red}}}$	$\frac{\rho_{\lambda1}-\rho_{\lambda2}}{\sqrt{\rho_{\lambda1}+\rho_{\lambda2}}}$	(Roujean and Breon, 1995)
Modified Vegetation Index	MVI	$\frac{\rho_{NIR}-1.2\rho_{Red}}{\rho_{NIR}+\rho_{Red}}$	$\frac{\rho_{\lambda1}-1.2*\rho_{\lambda2}}{\rho_{\lambda1}+\rho_{\lambda2}}$	(Paltridge and Barber, 1988)
Normalized Difference Vegetation Index	NDVI	$\frac{\rho_{NIR}-\rho_{Red}}{\rho_{NIR}+\rho_{Red}}$	$\frac{\rho_{\lambda1}-\rho_{\lambda2}}{\rho_{\lambda1}+\rho_{\lambda2}}$	(Rouse, 1974)
Advanced Simple Ratio	ASR	$\frac{\rho_{NIR}-(\rho_{Red}-(\rho_{Blue}-\rho_{Red}))}{\rho_{NIR}+(\rho_{Red}-(\rho_{Blue}-\rho_{Red}))}$	$\frac{\rho_{\lambda1}}{\rho_{\lambda2}+\rho_{\lambda3}}$	(Somvanshi and Kumari, 2020)
Advanced Normalized Difference Vegetation Index	ANDVI	$\frac{\rho_{NIR}-(\rho_{Red}-(\rho_{Blue}-\rho_{Red}))}{\rho_{NIR}+(\rho_{Red}-(\rho_{Blue}-\rho_{Red}))}$	$\frac{\rho_{\lambda1}-(\rho_{\lambda2}+\rho_{\lambda3})}{\rho_{\lambda1}+\rho_{\lambda2}+\rho_{\lambda3}}$	(Somvanshi and Kumari, 2020)
Reduced Simple Ratio	RSR	$***\frac{\rho_{NIR}}{\rho_{Red}}(1-\frac{\rho_{SWIR}-\rho_{SWIRmin}}{\rho_{SWIRmax}-\rho_{SWIRmin}})$	$\frac{\rho_{\lambda1}}{\rho_{\lambda2}}(1-\frac{\rho_{\lambda3}-\rho_{\lambda3_{min}}}{\rho_{\lambda3_{max}}-\rho_{\lambda3_{min}}})$	(Brown et al., 2000)

* Where ρ denotes the reflectance value at a given wavelength λ, NIR is the near-infrared reflectance.

** Where λ_1, λ_2, and λ_3 are the canopy reflectance spectra at different wavebands.

*** ϱ_{SWIR} represents the SWIR reflectance, $\varrho_{SWIRmin}$ and $\varrho_{SWIRmax}$ represent the minimum and maximum values in the SWIR, respectively.

A linear regression for each vegetation indices and the measured LAI values was performed to assess the strength of the relationship between proposed indices and LAI in MATLAB (version R2020b Update 3). The coefficient of determination (R^2) and the root mean squared error (RMSE) for all the different combinations were calculated. The indices that achieved higher accuracies were noted, and the best combinations of bands per index were found.

After finding the best combinations of bands using only VNIR reflectance spectra, new combinations were calculated in which either LST or LSE replaced one of the bands used in each vegetation index. With this procedure, all possible influences by LST and LSE values to vegetation indices were evaluated.

2.4.2. Leaf area index prediction using partial least squares regression

PLSR is a multivariate statistical tool in which the inputs are transformed to form new components to reduce the number of inputs. It combines independent variables to new predictor factors that are not correlated. PLSR has also been applied regularly in remote sensing applications (Cho et al., 2007; Kooistra et al., 2004).

Estimation of LAI using PLSR was done in MATLAB, using the "plsregress"-function (MathWorks Benelux, n.d.). Analogous to LAI estimation using vegetation indices, all multispectral bands are used as inputs for the PLSR function as a reference. Afterwards, LST or LSE is included as an additional input. To inspect the ability of the PLSR model to estimate the LAI using the different inputs, the cross-validated R_{cv}^2 and $RMSE_{cv}$ are calculated using the "leave-one-out method" (Duda et al., 1995). These are values that indicate how well a model can predict samples that are left out of the dataset (Shao, 1993). The analysis is done to observe the number of predictor variables needed to get the most accurate prediction of LAI; the commonly used criterion to include another predictor variable is when it can decrease $RMSE_{cv}$ by 2% (Geladi and Kowalski, 1986). With the least possible predictor variables, a linear model is created to show the correlation between the predicted LAI values and the measured LAI values.

Previous studies have shown that different vegetation species have individual emissivity signatures (French et al., 2000; Ribeiro da Luz and Crowley, 2007; Ullah et al., 2012). Therefore, the assumption can be made that when using TIR data in combination with reflectance spectra for single species to estimate LAI, better results can be achieved. To assess the influence of different vegetation species on the predictability of LAI, PLSR was also applied for plots with oak and beech as their dominant species. This resulted in PLSR analysis using ten plots for oak and 18 plots for beech. The analysis for the plots per dominant species was done analogous to the analysis using the complete dataset with mixed vegetation species plots.

3. RESULTS

3.1. Characteristics of the collected in-situ data

During the field campaign, LAI measurements were taken with the LICOR 2200C. The dominant species and the number of trees per plot were recorded. From the 35 plots in which measurements were done, 21 plots have European beech (*Fagus sylavatica*), 12 plots Oak (*Quercus robur*), and two plots Douglus fir (*Pseudotsuga menziesii*) as the dominant species. Additionally, the diffuse non-interceptive value (DIFN) was measured with the LICOR to infer the percentage of vegetation cover. Over 30 plots, LAI was measured with significant variance, ranging from 1.462 to 5.717. Table 3 shows statistics of the LAI, the DIFN, and the number of trees per plot. In Appendix I, the in-situ data of the individual plots is displayed.

Table 3: Statistical characteristics over all plots in the study area for the measured in-situ data, including leaf area index (LAI), percentage of vegetation cover (P_V), and the number of trees.

Variable	Mean statistics	Mean Std. Error	Min	Max	Std. Deviation
LAI	4.1247	0.2889	1.462	5.717	1.0162
DIFN	0.0584	0.0115	0.0107	0.3838	0.0682
No. of Trees	27.4	1.04	14	39	6.14

3.1.1. Relationship among leaf area index, reflectance spectra, land surface temperature and land surface emissivity

After extracting the mean values of the reflectance spectra for each band per plot, their relationships with the measured LAI were investigated. Figure 11 shows the relation between the measured LAI values and the mean reflectance spectra for each band (i.e., the green, red, red-edge, and NIR bands) using the multispectral camera. As can be seen from the scatterplots, the correlation between the measured LAI and the different reflectance is minimal; the NIR reflectance shows the highest coefficient of determination ($R^2 = 0.18567$) with the LAI value.

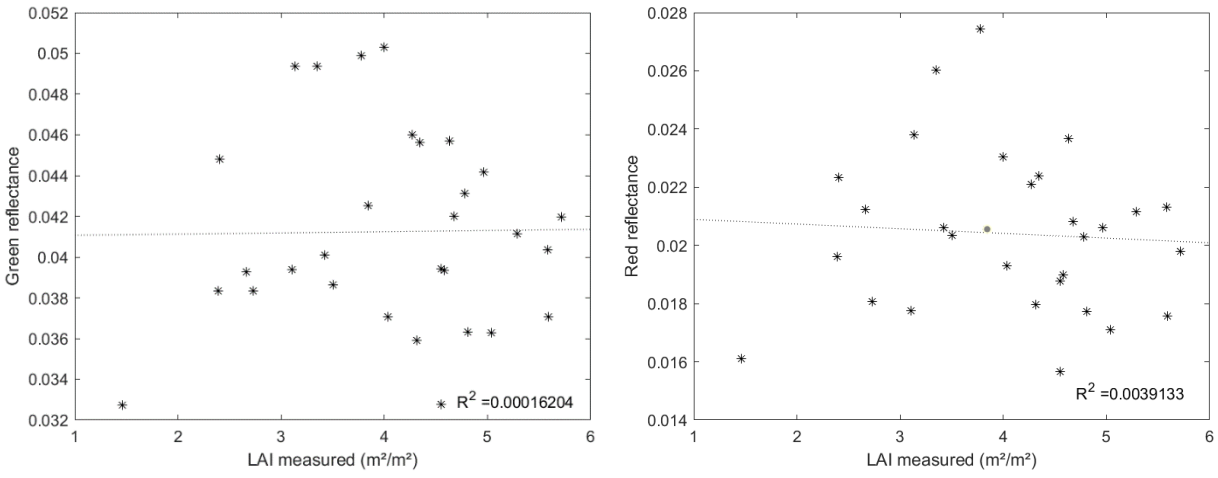

(a) (b)

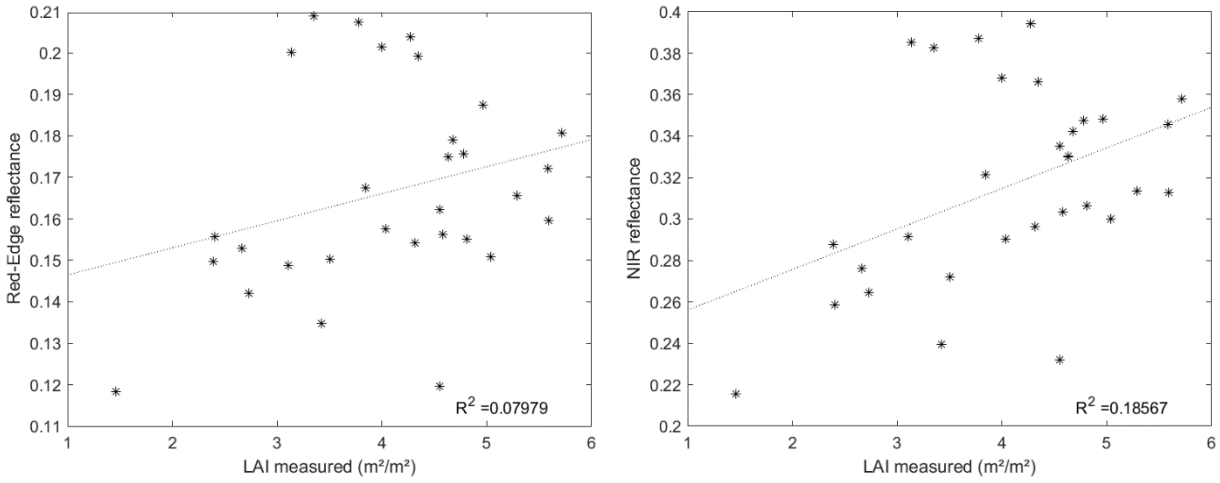

(c) (d)

Figure 11: Scatter plots of in situ measured leaf area index and the green reflectance (a), the red reflectance (b), the red-edge reflectance (c), and the NIR reflectance (d) for 30 plots.

For each plot, the mean LST value was extracted, and its relationship between LAI and LST was studied. Table 4 shows the summary statistics of the LST for the altitudes of 85 m (LST_{85}) and 120 m (LST_{120}) for the 30 plots. For both altitudes, the mean, standard deviation and error, and the minimum and maximum value are similar. However, when looking at LST_{85} and LST_{120} for the individual plots, there is a significant difference in value for most plots (Appendix II), with an average difference of 2.68 °C between LST_{85} and LST_{120}. This difference is also visible for one of the plots (Figure 12). Figure 12 shows an RGB map of the plot (plot 2, see Appendix I and II) and maps of the extracted LST for both flight heights. From the maps, it is visible that the average LST of the displayed plot was detected to be 2.5208 °C (see Appendix II, plot 2) lower at the higher altitude of 120 m than from the 85 m altitude.

Table 4: Statistical characteristics of the land surface temperature (LST), extracted from TIR images from different flight heights, 85 m and 120 m respectively (n=30).

Variable	Mean	Mean Std. Error	Min	Max	Std. Deviation
LST_{85}	21.4954 °C	0.3234 °C	18.3828 °C	25.1935 °C	1.7712 °C
LST_{120}	21.5095 °C	0.324 °C	18.5376 °C	24.8330 °C	1.7745 °C

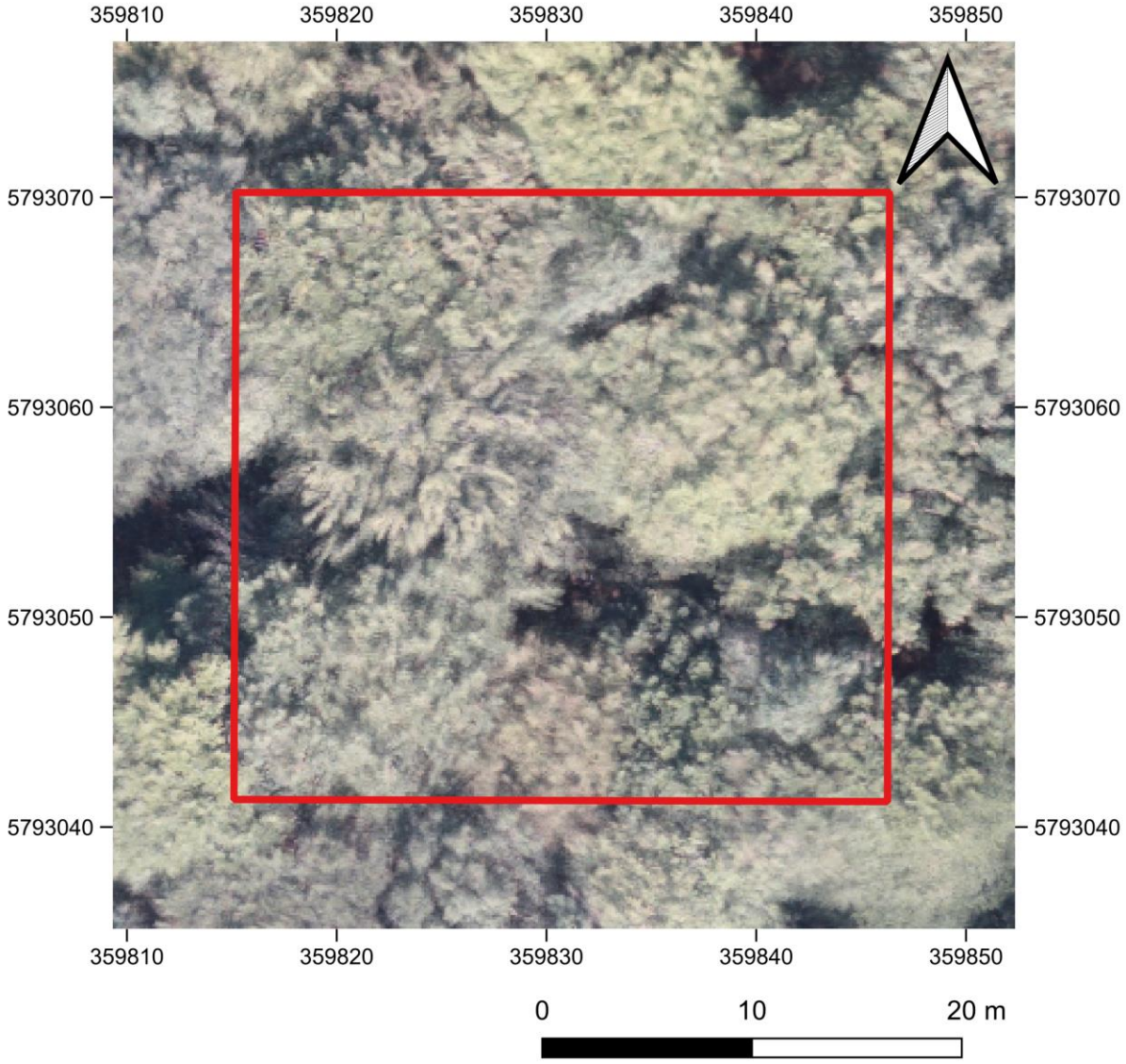
359810
359820
359830
359840
359850
5793070
5793060
5793050
5793040
0
10
20 m

(a)

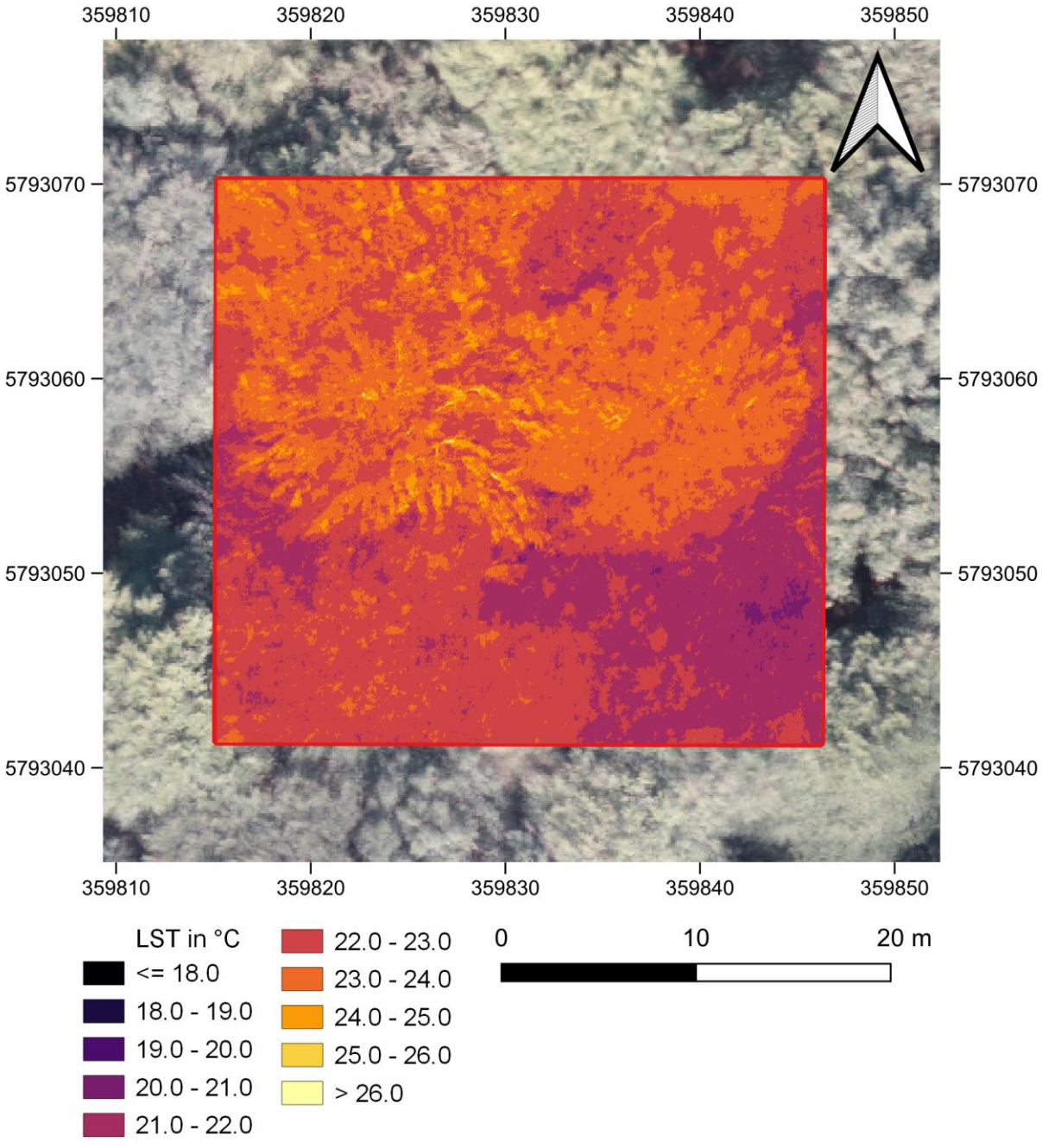
359810
359820
359830
359840
359850
5793070
5793060
5793050
5793040
LST in °C
<= 18.0
18.0 - 19.0
19.0 - 20.0
20.0 - 21.0
21.0 - 22.0
22.0 - 23.0
23.0 - 24.0
24.0 - 25.0
25.0 - 26.0
> 26.0
0
10
20 m

(b)

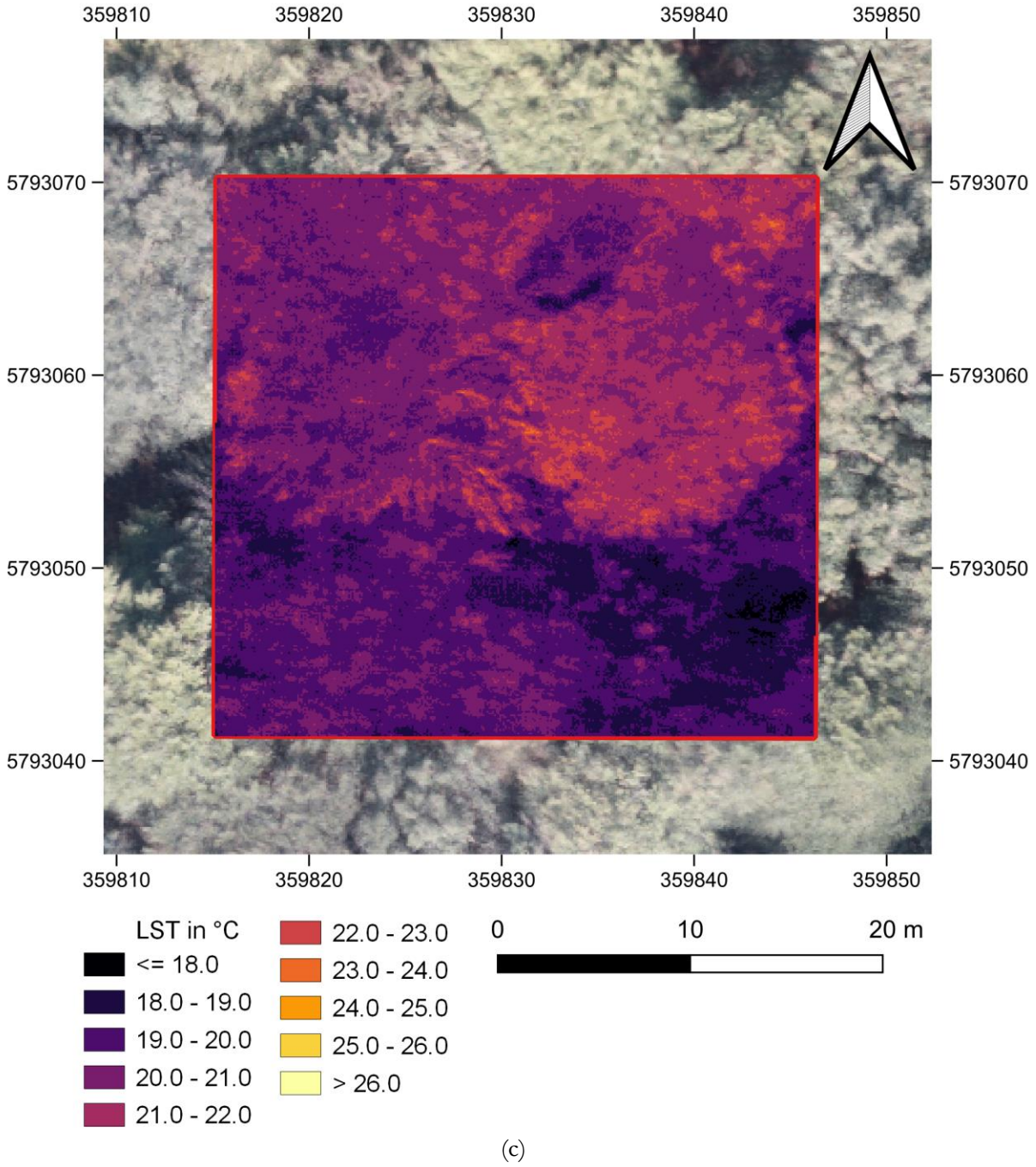

(c)

Figure 12: Maps of a single plot (outlined in red). RGB map (a), Land surface temperature (LST) map from TIR image captured at an 85 m altitude (b), and an LST map from TIR image captured at a 120 m altitude (c).

The relationship between LST and the measured LAI for the different altitudes can be seen in Figure 13. There is no significant fit between LAI and LST for both altitudes; a Pearson correlation coefficient revealed no significant correlation for LST_{85} ($r = -0.09$, P-value ≤ 0.63) and LST_{120} ($r = -0.14$, P-value ≤ 0.45).

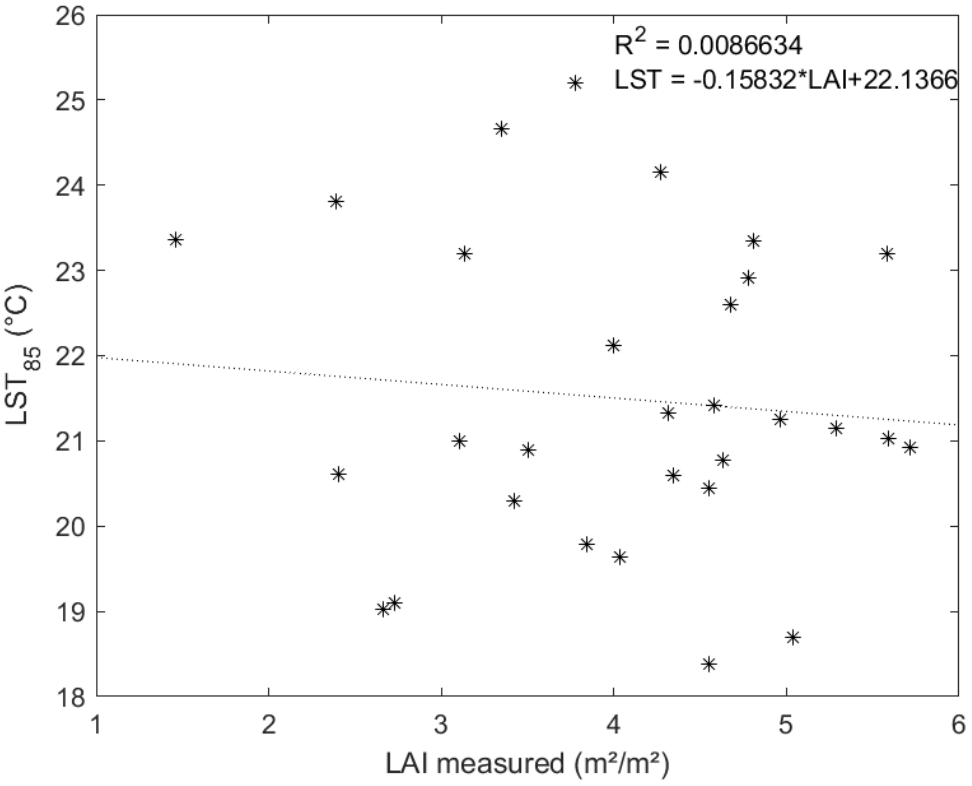

(a)

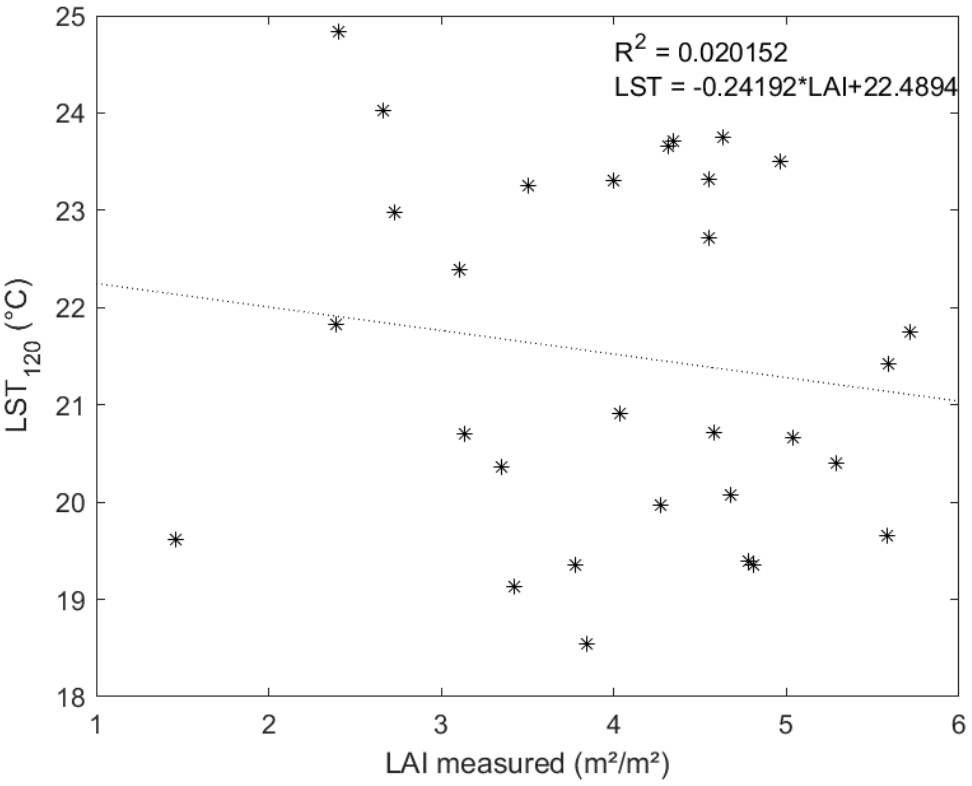

(b)

Figure 13: Scatter plots of in situ measured leaf area index (LAI) and land surface temperature (LST) obtained from an 85 m (LST_{85}) flight height (a), and LST detected from a 120 m (LST_{120}) flight height (b) for 30 plots.

As mentioned previously, LSE was estimated using P_V values that were calculated using different approaches. Table 5 shows the statistics for P_V obtained from both approaches. With the LICOR, a mean P_V of 93.6% vegetation cover was measured over all plots, while P_V estimation using the CHM yields an average of 96.3%. Noticeable is that the LICOR did not detect a plot with a vegetation cover of 100%; for the approach using the CHM, this was the case for some plots. Figure 14 shows the relationship between LAI and P_V from both approaches. Table 6 highlights the difference between the statistical characteristics of the resulting LSE. Due to the slightly higher average in P_V when using the CHM, also the resulting LSE_{CHM} has a higher average (0.986) compared to LSE_{LICOR} with an average of 0.9846.

Table 5: Statistical characteristics of the percentage of vegetation cover (P_V) measured with the LICOR 2200C and estimated using a canopy height model (CHM).

Variable	Mean	Mean Std. Error	Min	Max	Std. Deviation
$P_{V\ LICOR}$	0.936	0.013	0.616	0.989	0.072
$P_{V\ CHM}$	0.963	0.011	0.764	1	0.063

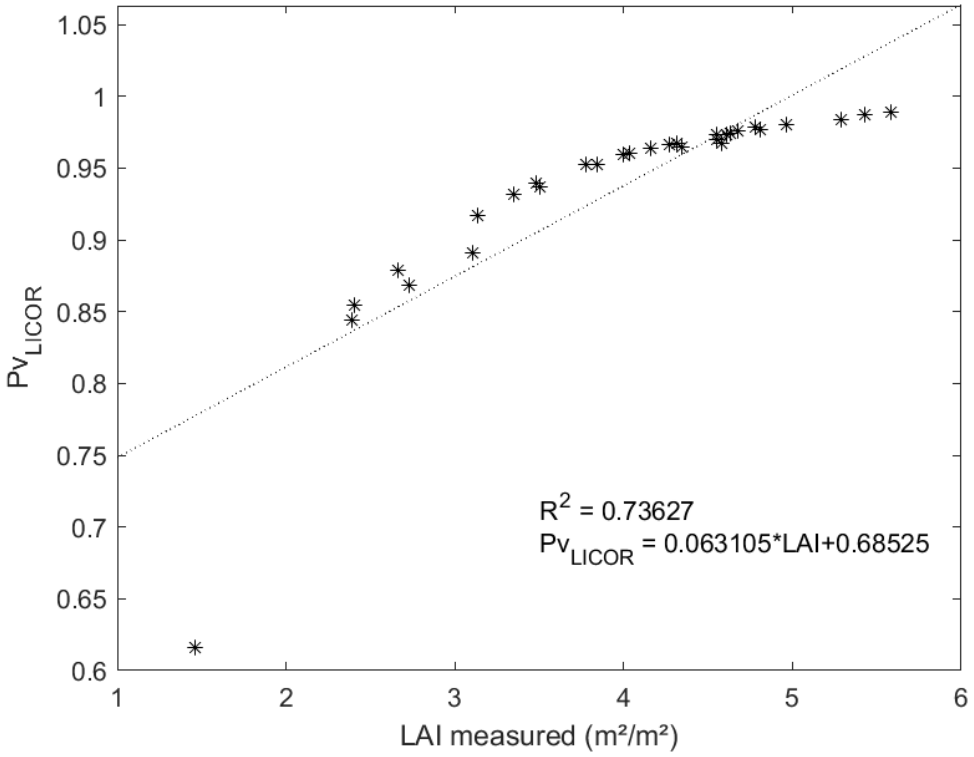

(a)

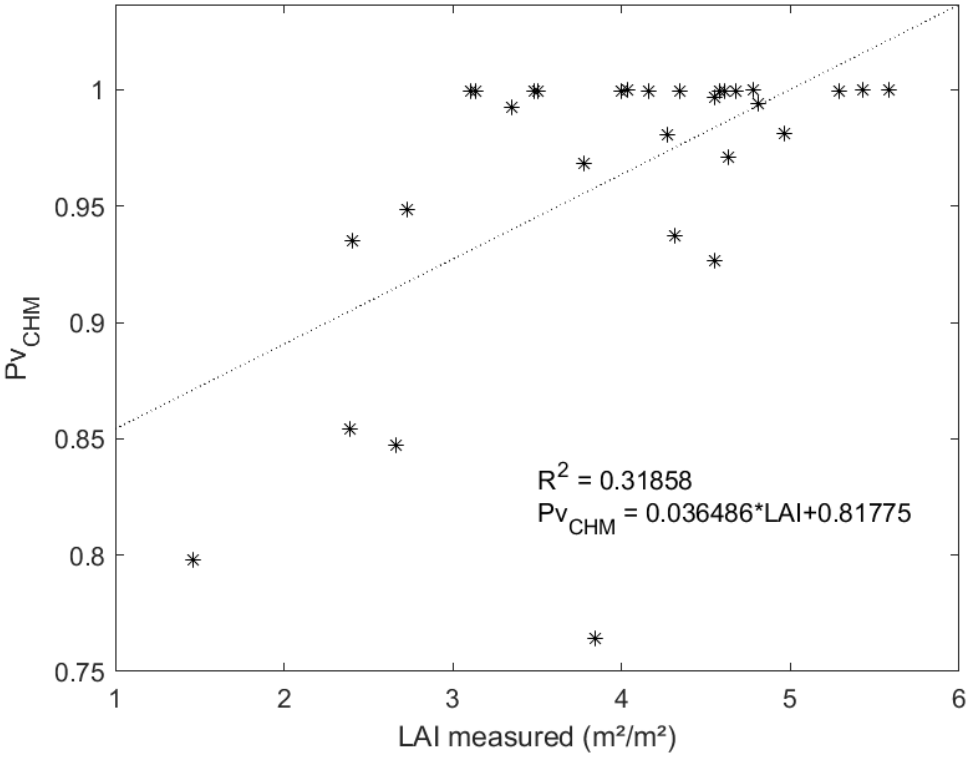

(b)

Figure 14: Scatter plots of in-situ measured leaf area index (LAI) and the percentage of vegetation cover (P_v) derived from measurements of the LICOR 2200C (Pv_{LICOR}) (a) and a canopy height model (CHM) (Pv_{CHM}) (b) for 30 plots.

Table 6: Statistical characteristics of the land surface emissivity (LSE), calculated using the percentage of vegetation cover P_V measured using different approaches (n=30).

Variable	Mean	Mean Std. Error	Min	Max	Std. Deviation
LSE_{LICOR}	0.9846	0.0007	0.9677	0.9874	0.0038
LSE_{CHM}	0.9860	0.0006	0.9755	0.9880	0.0033

In Figure 15, the relationships between the measured LAI and the differently calculated LSE are demonstrated. As shown in Figure 15, there is a significant correlation between LSE and LAI, with the highest R^2 of 0.73627 between LSE_{LICOR} and LAI. Correlation is high between LSE_{LICOR} and LAI when assessing using the Pearson correlation coefficient (r= 0.8581, P-value < 0.001). Comparing LSE_{CHM} with the measured LAI yields an R^2 of 0.31858; correlation is less, but still significant (r= 0.5644, P-value = 0.0012). Furthermore, from both scatterplots, it is visible that saturation occurs. As can be seen from Figure 15a, saturation occurs for LAI values higher than four. In Figure 15b, it can be seen that LSE_{CHM} reaches a maximum of 0.988 for multiple LAI values of three and higher.

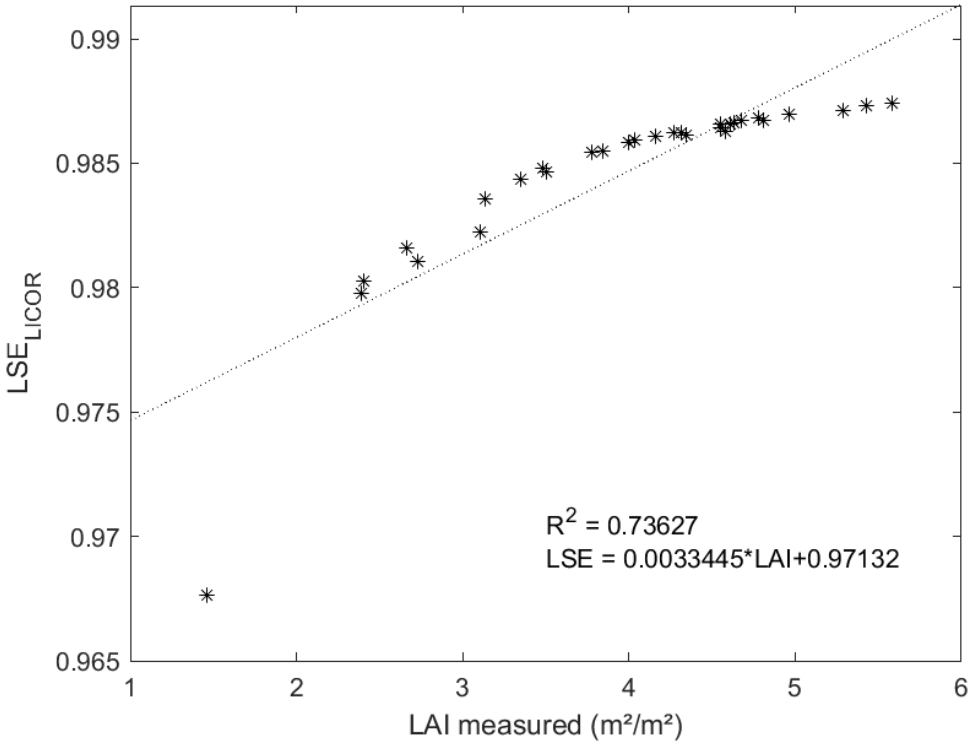

(a)

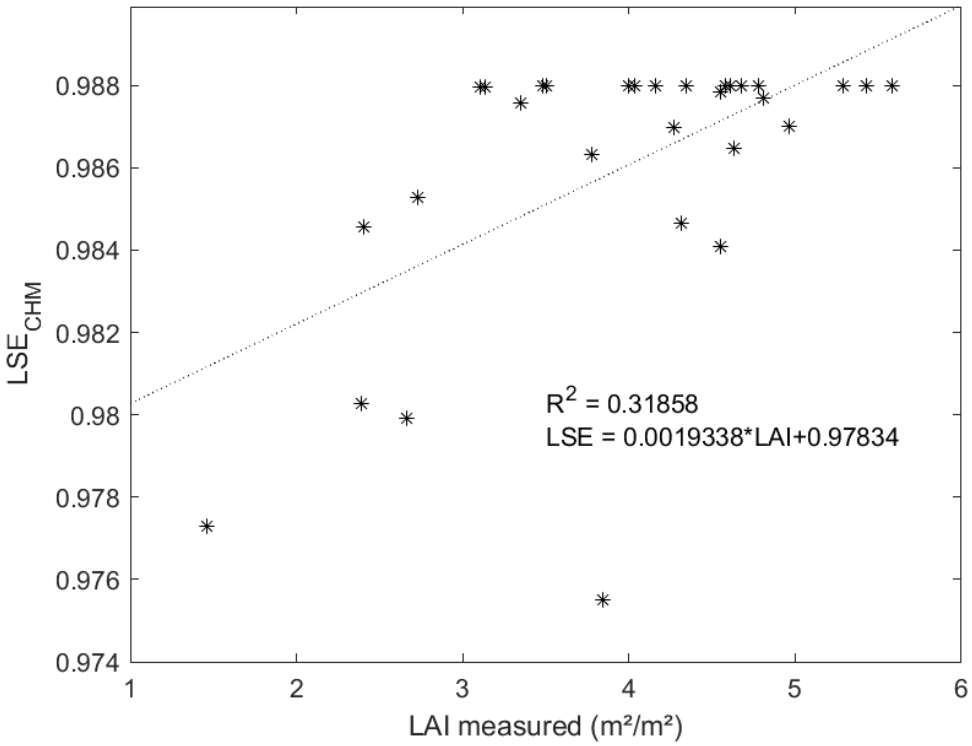

(b)

Figure 15: Scatter plots of in situ measured leaf area index (LAI) and land surface emissivity (LSE) calculated with the percentage of vegetation cover P_V derived using LICOR 2200C (LSE_{LICOR}) (a), and from a canopy height model (CHM) (LSE_{CHM}) (b) for 30 plots.

3.2. Estimated leaf area index using vegetation indices

3.2.1. Leaf area index estimation with vegetation indices using reflectance spectra

The best band combinations of the nine chosen vegetation indices were calculated using the VNIR reflectance spectra (Table 7). From Table 7, it can be inferred that LAI can be predicted with moderate accuracy using vegetation indices using reflectance spectra. The SR, including the NIR and the green band, proves to be the best vegetation index using two spectral bands, with an R^2 of 0.5675 and an RMSE of 0.7088, and slightly more accurate than the MVI and the NDVI. By upgrading the SR with a third band, for both ASR and RSR, LAI prediction accuracy increased compared to the two-band indices. The RSR using the NIR, green, and red-edge bands is shown to be the best predictor of LAI with an R^2 of 0.5815 and an RMSE of 0.6972. The scatter plots in Figure 16 show the measured LAI versus the predicted LAI using the SR and the RSR indices. The scatter plots showing the measured versus the predicted LAI for all the vegetation indices using the reflectance spectra can be found in Appendix III.

Table 7: The coefficients of determination (R^2) and the root mean squared error (RMSE) among the best combinations of vegetation indices using VNIR reflectance spectra and leaf area index.

Vegetation Index	Best Equation	R^2	RMSE
SR	$\frac{\rho_{NIR}}{\rho_{Green}}$	0.5675	0.7088
MSR	$\frac{\rho_{NIR} - \rho_{RedEdge} - 1}{(\rho_{NIR}/\rho_{RedEdge})^{0.5} + 1}$	0.4383	0.8078
SD	$\rho_{NIR} - \rho_{RedEdge}$	0.294	0.9056
RDI	$\frac{\rho_{NIR} - \rho_{RedEdge}}{\sqrt{\rho_{NIR} + \rho_{RedEdge}}}$	0.4162	0.8236
MVI	$\frac{\rho_{NIR} - 1.2\rho_{Green}}{\rho_{NIR} + \rho_{Green}}$	0.5582	0.7165
NDVI	$\frac{\rho_{NIR} - \rho_{Green}}{\rho_{NIR} + \rho_{Green}}$	0.5582	0.7165
ASR	$\frac{\rho_{NIR}}{\rho_{Green} + \rho_{Red}}$	0.5722	0.705
ANDVI	$\frac{\rho_{NIR} - (\rho_{Green} + \rho_{Red})}{\rho_{NIR} + \rho_{Green} + \rho_{Red}}$	0.5645	0.7113
RSR	$\frac{\rho_{NIR}}{\rho_{Green}}(1 - \frac{\rho_{RedEdge} - \rho_{RedEdge_{min}}}{\rho_{RedEdge_{max}} - \rho_{RedEdge_{min}}})$	0.5815	0.6972

3.2.2. Leaf area index estimation with vegetation indices using reflectance spectra and land surface temperature

Afterwards, LST was introduced as another band to be used to calculate the vegetation indices. Table 8 shows the best combinations of bands for the vegetation indices when including LST. The vegetation indices were calculated with LST from both flight heights. It can be seen that the SR is performing the best for both LST_{85} (R^2 = 0.3621) with the NIR reflectance band and LST_{120} (R^2= 0.2312) with the NIR reflectance band for the prediction of LAI. Compared to LAI prediction using vegetation indices with only the reflectance spectra, it can be seen that the vegetation indices, including LST, can predict LAI with lower accuracy. It can be observed that the vegetation indices SR, MVI, NDVI, ASR, and ANDVI, including LST_{85}, obtained slightly higher accuracy than the ones including LST_{120}. The other vegetation indices get very low values ($R^2 \leq 0.1$) when including either LST_{85} or LST_{120}.

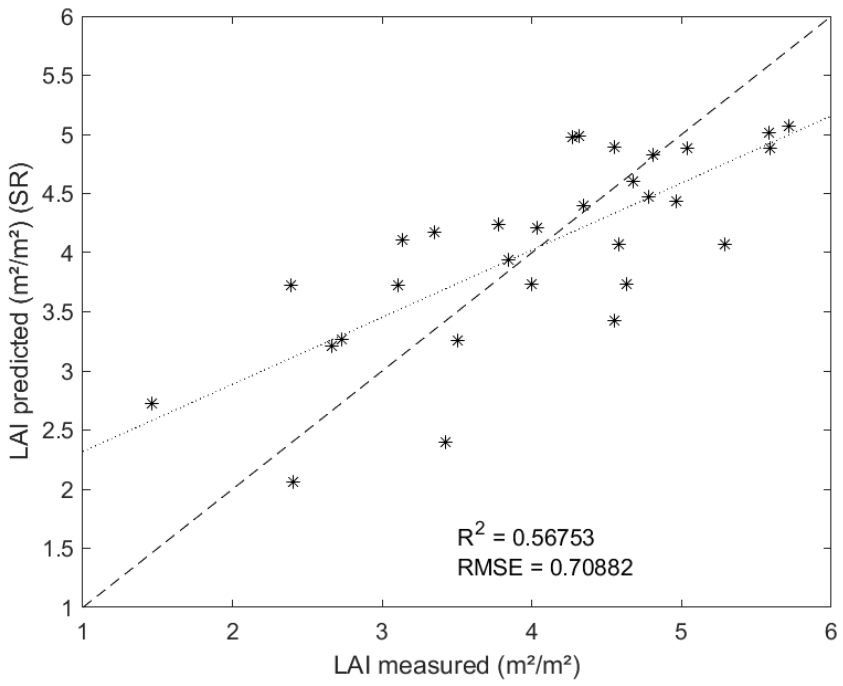

(a)

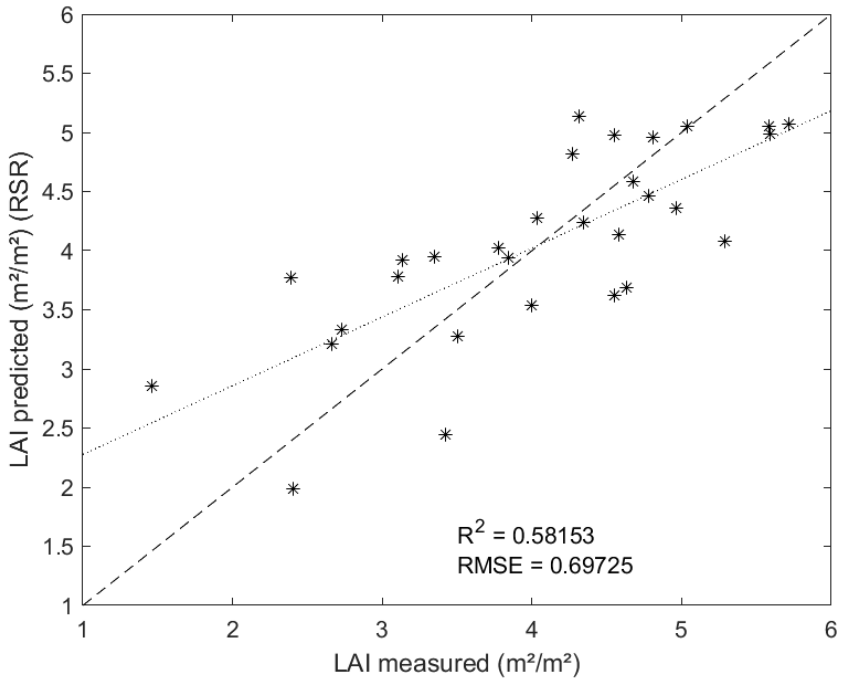

(b)

Figure 16: Scatter plots of in-situ measured leaf area index (LAI) versus the predicted LAI using the simple ratio (SR) (a) and the reduced simple ratio (RSR) (b) with the VNIR reflectance spectra as bands. The dashed lines show the optimal one on one fit, and the dotted lines show the predicted fit.

Table 8: The coefficients of determination (R^2) and the root mean squared error (RMSE) between the best combinations of vegetation indices using VNIR reflectance spectra and land surface temperature (LST) from two different flight heights as one of the inputs, and the leaf area index.

Vegetation Index	Best Equation	85 m flight height		120 m flight height	
		R^2	RMSE	R^2	RMSE
SR	$\frac{LST}{\rho_{NIR}}$	0.3621	0.8609	0.2312	0.945
MSR	$\frac{LST - \rho_{NIR} - 1}{(LST/\rho_{NIR})^{0.5} + 1}$	0.0624	1.0437	0.091	1.0276
SD	$LST - \rho_{NIR}$	0.0112	1.0718	0.0233	1.0652
RDI	$\frac{LST - \rho_{NIR}}{\sqrt{LST + \rho_{NIR}}}$	0.016	1.0692	0.0283	1.0625
MVI	$\frac{LST - 1.2\rho_{NIR}}{LST + \rho_{NIR}}$	0.3222	0.8874	0.1661	0.9843
NDVI	$\frac{LST - \rho_{NIR}}{LST + \rho_{NIR}}$	0.3222	0.8874	0.1661	0.9843
ASR	$\frac{LST}{\rho_{NIR} + \rho_{Red}}$	0.3417	0.8745	0.2152	0.9549
ANDVI	$\frac{\rho_{NIR} - (LST + \rho_{RedEdge})}{\rho_{NIR} + LST + \rho_{RedEdge}}$	0.3238	0.8863	0.1672	0.9836
RSR	$\frac{\rho_{NIR}}{\rho_{Red}}(1 - \frac{LST - LST_{min}}{LST_{max} - LST_{min}})$	0.0677	1.0407	0.0711	1.0388

The following Figure (Figure 17) shows scatter plots of the measured LAI versus the predicted LAI from the best of the vegetation indices using LST_{85} and LST_{120} as one of the inputs, using SR. In Appendix IV, the scatter plots showing the measured versus the predicted LAI for all the vegetation indices using the VNIR reflectance spectra combined with LST.

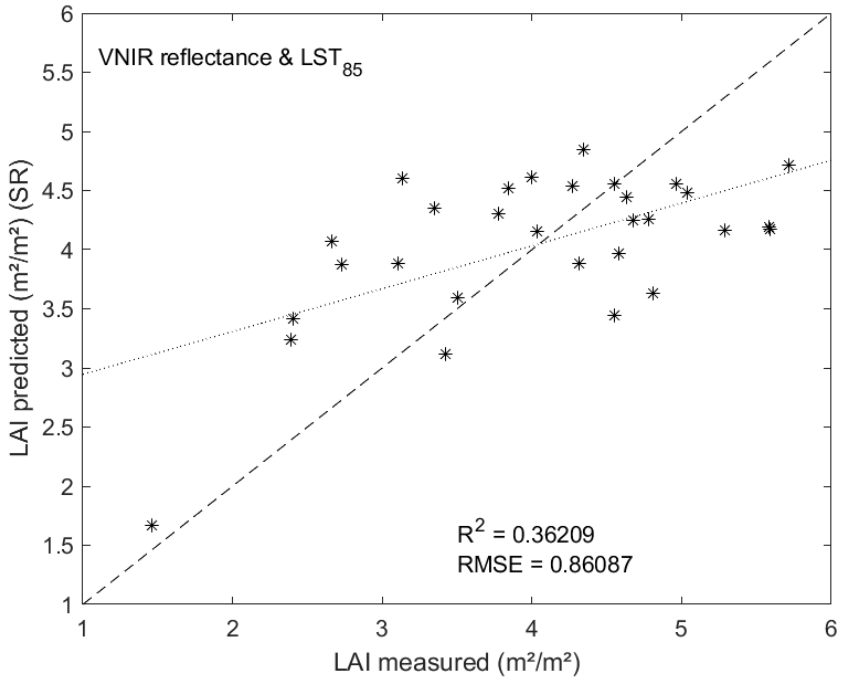

(a)

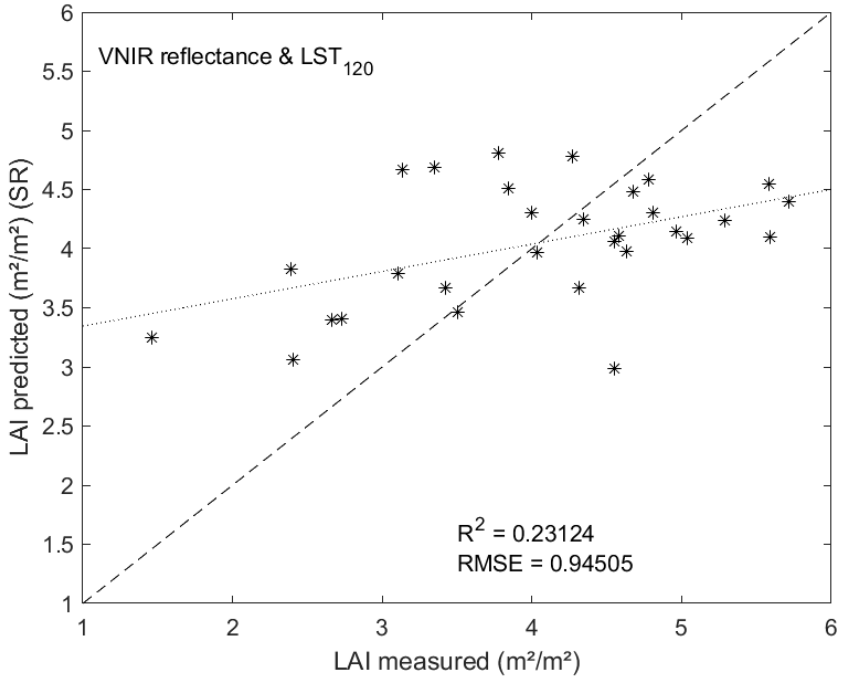

(b)

Figure 17: Scatter plots of in situ measured leaf area index (LAI) versus the predicted LAI using the simple ratio index (SR) including VNIR reflectance spectra and land surface temperature (LST) obtained at 85 m (LST_{85}) (a), and the SR including LST obtained at 120 m (LST_{120}) (b). The dashed lines show the optimal one on one fit, and the dotted lines show the predicted fit.

3.2.3. Leaf area index estimation with vegetation indices using reflectance spectra and land surface emissivity

Analogous to LST, LAI was also predicted using the nine different vegetation indices using LSE as one of the inputs. As mentioned previously, LSE was calculated two times using different values for P_V, leading to two different estimations of LAI. The best combinations of bands for the vegetation indices, including LSE, are shown in Table 9. As shown in Table 9, the combination of the LSE_{LICOR} as an input and VNIR reflectance spectra in the different vegetation indices improved the prediction accuracy of LAI using RSR (R^2=0.7458, RMSE=0.5081).

When comparing the LAI estimation using LSE_{LICOR} and LSE_{CHM}, it can be seen that LSE_{LICOR} achieves better results with the SD (R^2 = 0.614) and the RSR (R^2 = 0.7458). With all other vegetation indices, for both LSE_{LICOR} and LSE_{CHM}, the R^2 and RMSE indicate a low accuracy for the prediction of LAI. Figure 18 shows the measured versus the predicted LAI using the RSR index using VNIR reflectance spectra combined with the LSE. When including LSE_{LICOR} in the LAI estimation using RSR, the predicted LAI saturates at a value of 4.5. Also, for LAI estimation using the RSR, including LSE_{CHM}, it is visible that the predicted LAI reaches a maximum value of approximately 4.5 for multiple samples, for measured LAI values of three and higher. In Appendix V, the scatter plots of the measured versus the predicted LAI for all the vegetation indices using the VNIR reflectance spectra and LSE can be found.

Table 9: The coefficients of determination (R^2) and the root mean squared error (RMSE) among the best combinations of vegetation indices using reflectance spectra and land surface emissivity calculated using two different approaches (LSE_{LICOR} and LSE_{CHM}), for retrieval of the leaf area index.

Vegetation Index	Best Equation	LSE_{LICOR}		LSE_{CHM}	
		R^2	RMSE	R^2	RMSE
SR	$\frac{LSE}{\rho_{NIR}}$	0.2522	0.8714	0.2603	0.8666
MSR	$\frac{LSE - \rho_{NIR} - 1}{(LSE/\rho_{NIR})^{0.5} + 1}$	0.1725	0.9166	0.1901	0.9068
SD	$LSE - \rho_{Red}$	0.6114	0.6281	0.2318	0.8832
RDI	$\frac{LSE-\rho_{NIR}}{\sqrt{LSE+\rho_{NIR}}}$	0.197	0.9029	0.2103	0.8954
MVI	$\frac{LSE-1.2\rho_{NIR}}{LSE+\rho_{NIR}}$	0.2163	0.892	0.2231	0.8882
NDVI	$\frac{LSE-\rho_{NIR}}{LSE+\rho_{NIR}}$	0.2163	0.892	0.2231	0.8882
ASR	$\frac{LSE}{\rho_{NIR}+\rho_{Red}}$	0.2354	0.8811	0.2437	0.8763
ANDVI	$\frac{\rho_{NIR} - (LSE + \rho_{RedEdge})}{\rho_{NIR} + LSE + \rho_{RedEdge}}$	0.2398	0.8786	0.2467	0.8745
RSR	$\frac{\rho_{NIR}}{\rho_{Red}}(1 - \frac{LSE - LSE_{min}}{LSE_{max} - LSE_{min}})$	**0.7458**	0.5081	0.2707	0.8605

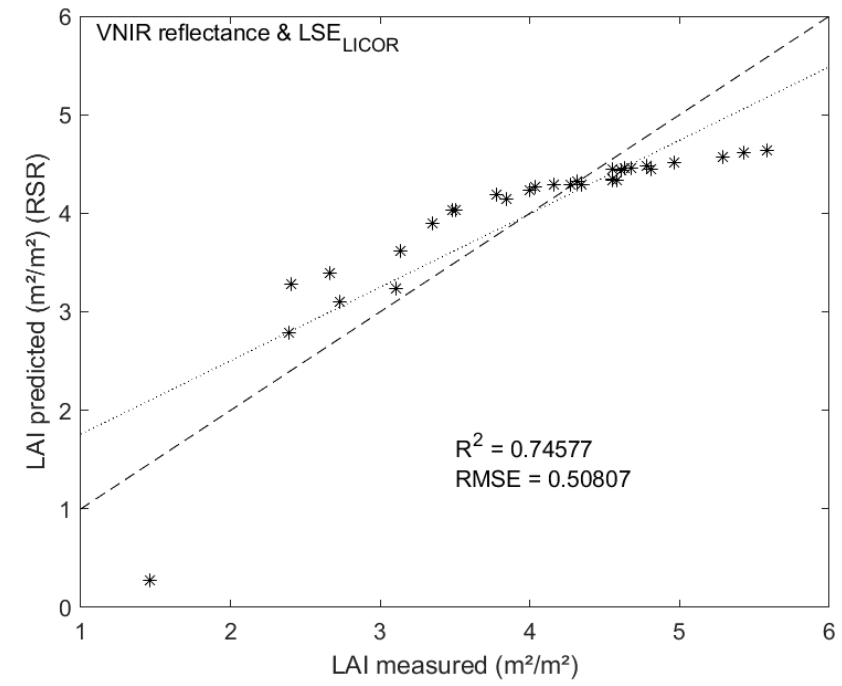

(a)

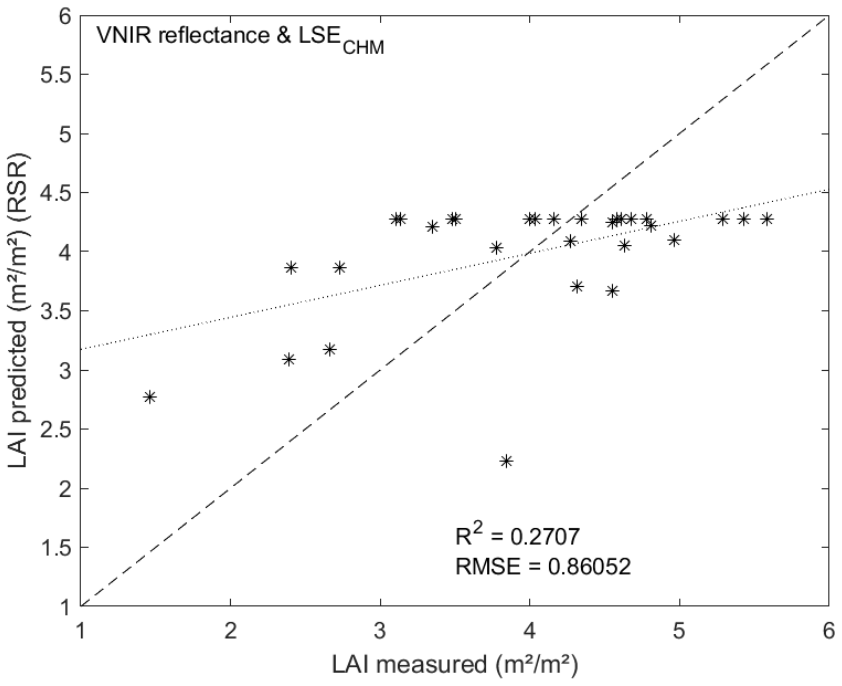

(b)

Figure 18: Scatter plots of in-situ measured leaf area index (LAI) versus the predicted LAI using the reduced simple ratio vegetation index (RSR) with VNIR reflectance spectra and land surface emissivity calculated using two approaches (as mentioned in section 2.3.3): LSE_{LICOR} (a) and LSE_{CHM} (b). The dashed lines show the optimal one on one fit, and the dotted lines show the predicted fit.

3.3. Estimated leaf area index using partial least squares regression

3.3.1. Leaf area index estimation with partial least squares regression using reflectance spectra

Depending on the inputs used for PLSR, the optimal number of factors used to estimate LAI varied. To determine how many factors were needed, the percentage of variance explained by adding more PLS components was consulted, which is equal to R^2. To avoid overfitting by using too many PLS components, the $RSME_{CV}$ was used, as cross-validation indicates how well the model can predict LAI. Extra factors were only considered when $RSME_{CV}$ would not increase. Figure 19 shows the percentage of variance explained of the LAI and the $RSME_{CV}$ with the number of PLS components used, for when only the VNIR reflectance spectra are used as inputs. As R^2 is nearly at its maximum and $RMSE_{CV}$ is at its minimum both for two PLS components, this was the optimal amount of PLS factors to be used in this case.

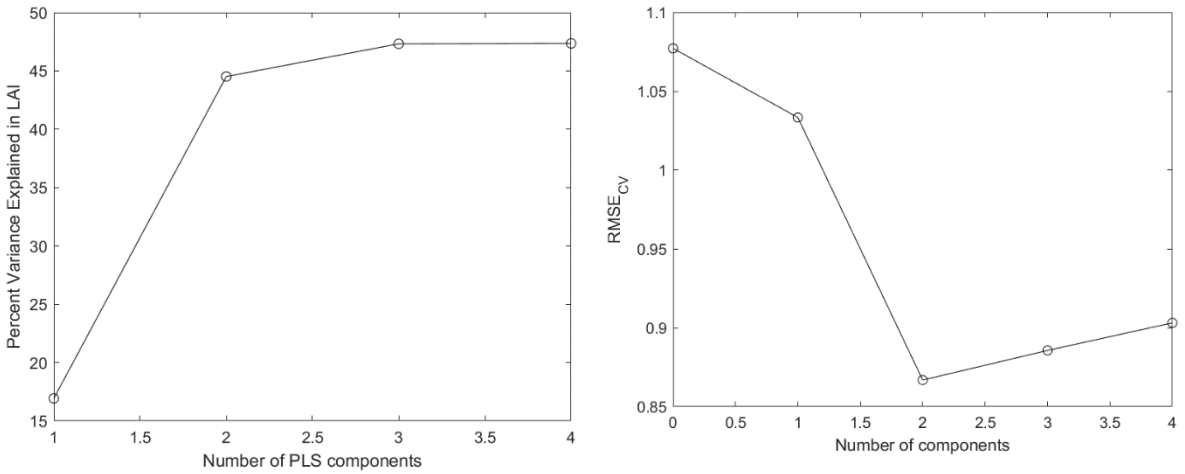

(a) (b)

Figure 19: Percent of variance explained in leaf area index (LAI) (a) and the cross-validated root mean squared error ($RMSE_{CV}$) (b) versus the number of partial least squares (PLS) components used in the partial least squares regression analysis, using the reflectance spectra as inputs.

LAI was then estimated using PLSR with two factors. Figure 20 shows the measured LAI compared with the predicted LAI using PLSR with the VNIR reflectance spectra as inputs. It can be seen that with an R^2 of 0.44517, the LAI prediction accuracy is lower than when using vegetation indices (max R^2=0.5815).

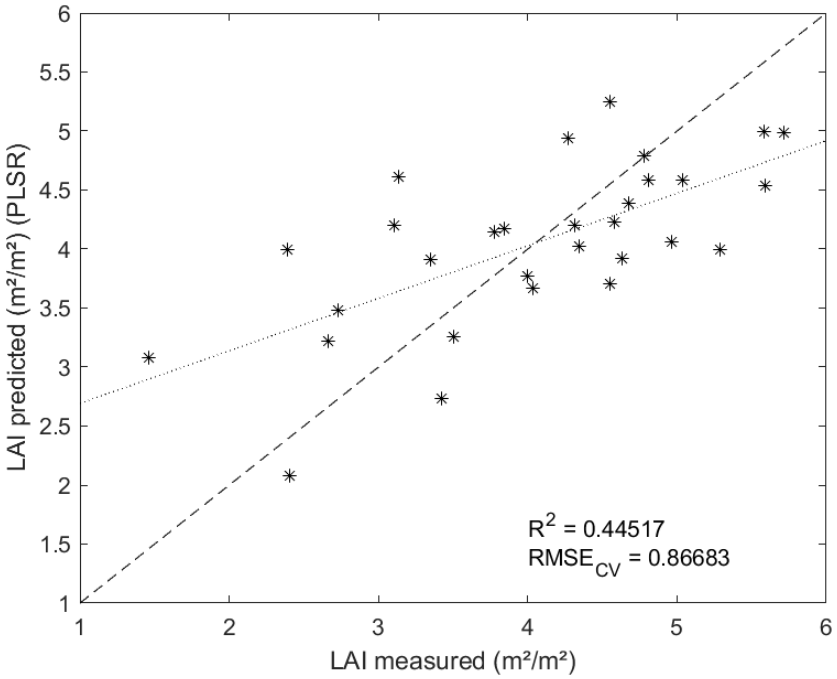

Figure 20: Scatter plot of in-situ measured leaf area index (LAI) versus the predicted LAI using partial least squares regression (PLSR) with two components applying the reflectance spectra as inputs. The dashed line shows the optimal one on one fit, and the dotted line shows the predicted fit.

3.3.2. Leaf area index estimation with partial least squares regression using reflectance spectra and land surface temperature

Following the PLSR analysis using only VNIR reflectance spectra, PLSR was executed with an additional input, LST, derived from both flight heights separately. As can be seen in Table 10, adding LST_{85} as another input increases the R^2 and decreases the $RMSE_{CV}$, indicating that the extra information from the added input helps to increase the prediction accuracy of LAI. Additionally, when adding another input like LST, the optimal number of PLS components increases to three. This is also visualised in Figure 21. Notable is that LST_{120} does not improve the prediction of LAI, which is a similar result as when predicting LAI with the use of vegetation indices and using LST_{120} as an input.

Table 10: The optimal number of partial least squares (PLS) components, the coefficients of determination (R^2), and the cross-validated root mean squared error ($RMSE_{CV}$) for partial least squares regression analysis (n=30).

Inputs	Number PLS components	R^2	$RMSE_{CV}$
Reflectance spectra	2	0.4452	0.8668
Reflectance spectra & LST_{85}	3	0.5565	0.7998
Reflectance spectra & LST_{120}	3	0.4512	0.8969
Reflectance spectra & LSE_{LICOR}	3	0.7907	0.8351
Reflectance spectra & LSE_{CHM}	3	0.3743	0.9767

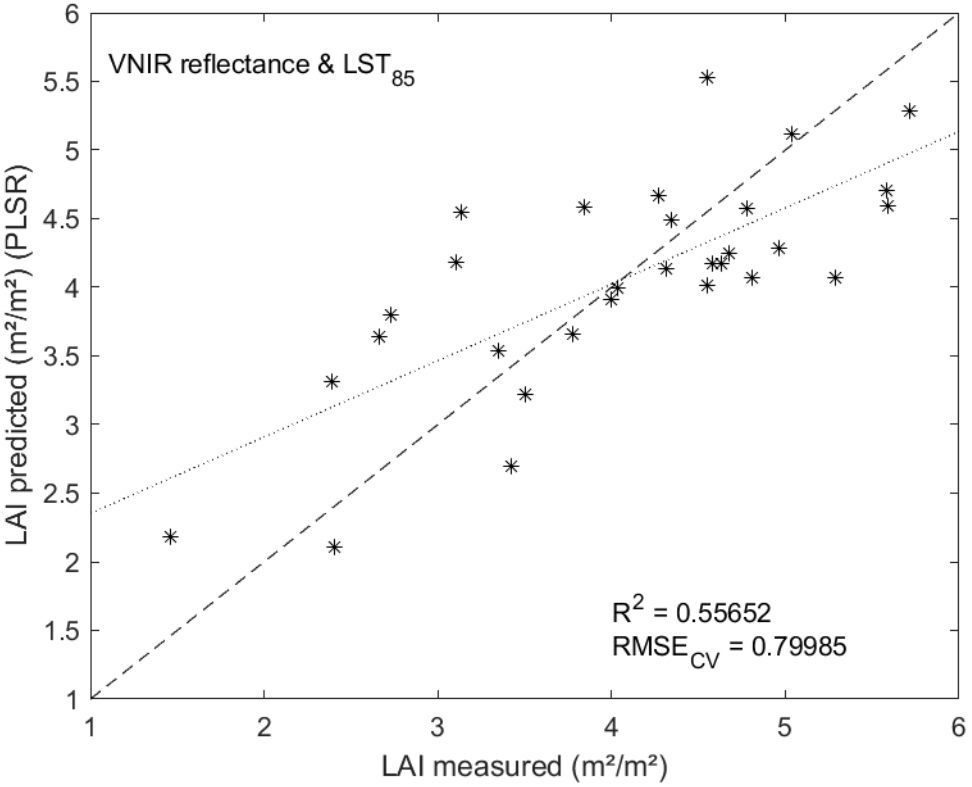

(a)

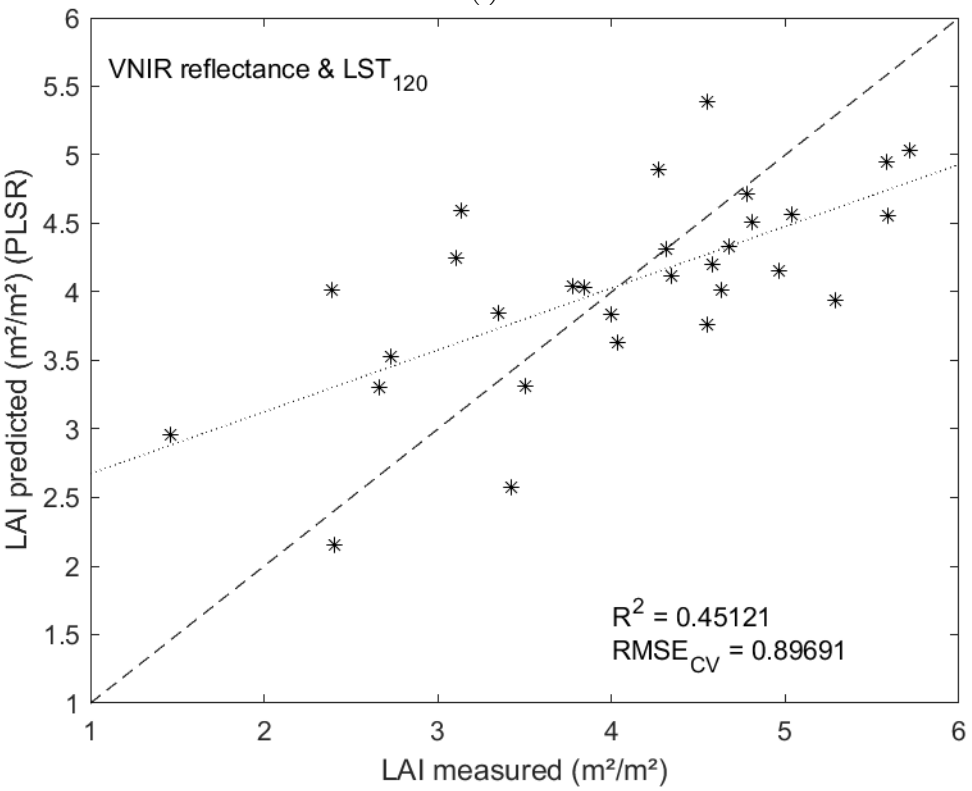

(b)

Figure 21: Scatter plot of in-situ measured leaf area index (LAI) versus the predicted LAI using partial least squares regression (PLSR) and applying the reflectance spectra as well as land surface temperature (LST) from 85 m altitude (LST_{85}) (a), and LST from 120 m altitude (LST_{120}) (b) as inputs. The dashed line shows the optimal one on one fit, and the dotted line shows the predicted fit.

3.3.3. Leaf area index estimation with partial least squares regression using reflectance spectra and land surface emissivity

LSE was also considered and added next to the VNIR reflectance spectra as an input to the PLSR analysis. Figure 22 depicts the ability of LSE in PLSR to successfully predict LAI with relatively high accuracy when using LSE_{LICOR} (R^2 = 0.7907). Similarly to LAI prediction with the RSR, a saturation is visible for LAI values of 4.5 and higher (Figure 22a). Adding LSE_{CHM} as input for PLSR decreases the prediction accuracy compared to using only reflectance spectra, as shown in Table 10 and Figure 22. Compared to the addition of LST to the analysis, the prediction of LAI with the inclusion of LSE_{LICOR} has improved to a much greater extent.

3.3.4. Leaf area index estimation with partial least squares regression considering different dominant species

Furthermore, analysis was done to assess the influence of the main species per plot on the prediction accuracy of LAI using PLSR. For the ten oak plots and the 18 beech plots, analysis was done analogous to the analysis with the complete mixed dataset. Table 11 shows the results of the PLSR analysis differentiated by dominant species. This includes using just the VNIR reflectance spectra as input, including LST, from both flight heights respectively, as well as including LSE from both approaches into the model. As can be seen from Table 11, PLSR analysis using only plots with oak as the dominant species yields lower values for R^2 compared to mixed plots when using only reflectance spectra as well as reflectance spectra and LST as inputs. For the reflectance spectra in combination with LSE_{LICOR}, R^2 is higher (R^2 = 0.9108) and $RMSE_{CV}$ decreases ($RMSE_{CV}$ = 0.4256). When using reflectance spectra and LSE_{CHM} to estimate LAI for oak plots, R^2 increases compared to mixed plots (R^2 = 0.398), however $RMSE_{CV}$ increases ($RMSE_{CV}$ = 1.2588). For plots with beech as their dominant species, the LAI estimation accuracy is slightly higher compared to mixed plots for all inputs, with the best result being achieved when using the VNIR reflectance spectra and LSE_{LICOR} as inputs (R^2 = 0.8766, $RMSE_{CV}$ = 0.4129).

Table 11: The optimal number of partial least squares (PLS) components, the coefficients of determination (R^2), and the cross-validated root mean squared error ($RMSE_{CV}$) for partial least squares regression analysis when analysing by dominant species.

Inputs	Species	Number of plots	Number PLS components	R^2	$RMSE_{CV}$
Reflectance spectra	Mixed	30	2	0.4452	0.8668
Reflectance spectra & LST_{85}			3	0.5565	0.7998
Reflectance spectra & LST_{120}			3	0.4512	0.8969
Reflectance spectra & LSE_{LICOR}			3	0.7907	0.8351
Reflectance spectra & LSE_{CHM}			3	0.3743	0.9767
Reflectance spectra	Oak	10	2	0.3243	0.775
Reflectance spectra & LST_{85}			3	0.3395	0.8448
Reflectance spectra & LST_{120}			3	0.3357	0.945
Reflectance spectra & LSE_{LICOR}			3	0.9108	0.4256
Reflectance spectra & LSE_{CHM}			2	0.398	1.2588
Reflectance spectra	Beech	18	3	0.5298	0.8566
Reflectance spectra & LST_{85}			3	0.5592	0.8626
Reflectance spectra & LST_{120}			4	0.5323	0.9013
Reflectance spectra & LSE_{LICOR}			3	0.8766	0.4129
Reflectance spectra & LSE_{CHM}			3	0.6589	0.7167

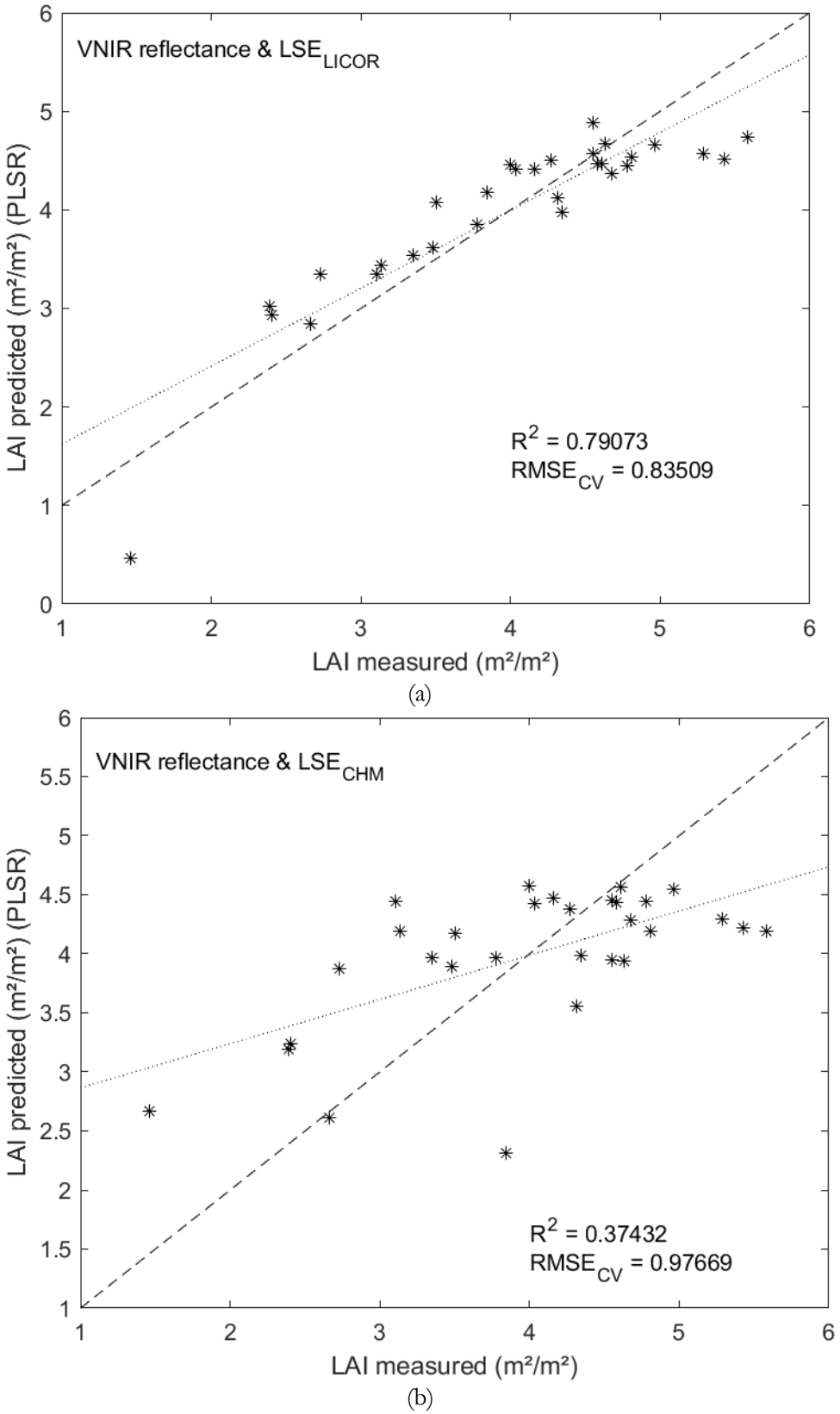

Figure 22: Scatter plot of in-situ measured leaf area index (LAI) versus the predicted LAI using partial least squares regression (PLSR) applying the reflectance spectra as well as land surface emissivity (LSE) calculated using two approaches (as inputs: LSE_{LICOR} (a), and LSE_{CHM} (b). The dashed line shows the optimal one on one fit, and the dotted line shows the predicted fit.

4. DISCUSSION

This research was the first to estimate LAI with the integration of TIR and VNIR remote sensing data collected with a UAS for a mixed forest. This study shows that the prediction accuracy of LAI can be improved to some extent, depending on the methods and quality of the dataset. This emphasises previous findings for integration of TIR with VNIR/SWIR data using Landsat-8 images, stating that there is a high potential to improve the LAI prediction accuracy (Neinavaz et al., 2019). This section discusses the different outcomes of the research, analysing the results in the workflow order.

4.1. Analysis of data collection

4.1.1. In-situ data

To analyse the LAI prediction accuracy using remote sensing data captured by sensors mounted to a UAV, the in-situ data collected during fieldwork in this research is assumed to be correct, showing the actual LAI. While the operation of the LICOR 2200C is based on some assumptions, measurements that are performed with it are accepted and used in many studies regarding LAI as a reference (Bréda, 2003; Danner et al., 2015). The collected data shows that the lowest values for LAI were measured in plots with Fir as the dominant species (1.462 and 2.408), plots with Oak or Beech as the dominant species show similar values ranging from approximately 2.4 to 5.7 (Appendix I). High LAI values above 5 were found in plots with either very tall trees or plots with more than 30 trees (Appendix I). However, the number of trees does not have much influence on LAI when looking at all plots; this is due to the different size and crown projected area per tree.

4.1.2. Images collected by means of UAS

A remarkable difference has been observed in LST measured for the different flight altitudes for all plots (Appendix II). In previous research, it was noticed that atmospheric effects and water vapour can introduce an error in LST calculation (Ogawa et al., 2008; Tonooka and Palluconi, 2005). In contrast, it was stated that atmospheric correction is not needed for very low altitudes (Messina and Modica, 2020). Therefore, the LST difference for the UAS flight heights of 85 m and 120 m may come partly from the atmospheric conditions. Another aspect that could influence the LST values of the two altitudes is the temporal difference of image acquisition. UAS flights to capture the TIR images were performed for parts of the study area first with an altitude of 85 m and directly afterwards with an altitude of 120 m, leading to a time difference of approximately 20 minutes between the captures. Although this time difference would not lead to a noticeable difference in the true LST, the sensor measurements could be influenced by it, as thermal cameras can have an adjustment period in which the measurements can fluctuate (Berni et al., 2009; Sagan et al., 2019).

4.2. Relationship among leaf area index, reflectance spectra, land surface temperature and land surface emissivity

4.2.1. Relationship among leaf area index and reflectance spectra

Previous studies using hyperspectral sensors have shown that a change in LAI causes high variation in NIR reflectance, while effects in the VIS domain are relatively small (Asner, 1998; Darvishzadeh et al.,

2009). This is also reflected in this research; the linear regression models between LAI and reflectance in green (0.55 μm) and red (0.66 μm) bands show an R^2 of less than 0.01. The correlation between LAI and the red-edge reflection (0.735 μm) was 0.08, while the relation between LAI and the NIR reflection (0.79 μm) shows the highest R^2 of 0.19.

4.2.2. Relationship among leaf area index and land surface temperature

Analysing the relationship between LAI and LST, as well as LAI and LSE also confirms findings from preceding research. While the LST was found to be influenced by vegetation in urban areas (Maimaitiyiming et al., 2014), there is no significant relation between LAI and LST (Kumar and Shekhar, 2015; Neinavaz et al., 2019; Zhang et al., 2009). For both flight altitudes, the correlation between LAI and LST was found very low (R^2 = 0.009 for LST_{85}, R^2 = 0.02 for LST_{120}); our findings revealed a slight negative relation between LAI and LST (Figure 13). This does not yet give information about the quality of data from the different flight heights.

4.2.3. Relationship among leaf area index and land surface emissivity

The relationship between LAI and LSE shows a significant positive correlation for both LSE_{LICOR} and LSE_{CHM}. A literature review reveals that LSE was found to increase with an increase of vegetation (Olioso et al., 2007; Sobrino et al., 2005), and with dense vegetation and increasing LAI, the LSE value is expected to be increased (Jin and Liang, 2006). Also, Neinavaz *et al.* (2019) stated that a strong relation between LAI and LSE exists over mixed temperate forest using satellite image.

The high correlation between LAI and LSE_{LICOR} can be explained by the fact that LSE_{LICOR} is calculated based on P_V in-situ measurements using the LICOR 2200C, which expectedly has a higher accuracy as it was previously revealed that prediction accuracy of P_V affects LSE calculation using the NDVI-threshold method (Neinavaz et al., 2020). This is also visible when comparing Figures 14 and 15, which show the relationship between P_V and LSE with the LAI. For both approaches, using in-situ measurements and CHM-derived data, the R^2 is the same when comparing the relationship between P_V and LSE with the LAI. This indicates that the NDVI-threshold method depends entirely on P_V when the NDVI value falls in between the thresholds for full soil and full vegetation values (Sobrino and Raissouni, 2000), which was the case in this study for all plots.

Notably, there is a saturation in LSE_{LICOR} for LAI values above 4.5. There is one distinct outlier visible in Figure 15a, which belongs to the plot with the lowest LAI measured (1.462) and also the lowest P_V (61%) (plot 3, see Appendix I and II). The plot, with Fir as the dominant species, had only a few tall trees but much understory; LAI measurements were performed on a height of approximately 2 m above the ground, missing most of the understory. LSE_{LICOR} for this plot was very low due to the strong influence of soil emissivity as a background. It can also be assumed that the understory might increase the LSE value, which needs to be further investigated using different approaches.

LAI and LSE_{CHM} are less correlated; however, there is still a significant relationship between the two variables. Figure 15b shows that for multiple plots, the maximum LSE value of 0.988 is reached. This comes forth because the CHM indicates a complete cover of tall vegetation for these plots ($Pv_{CHM} = 1$), as visualised in figure 14b. Therefore, using the NDVI-threshold method, LSE_{CHM} for these plots is only influenced by the emissivity of vegetation and not by the emissivity of the soil. Overall, LSE_{CHM} has higher values than LSE_{LICOR} due to the different derivations of P_V accuracy.

4.3. Leaf area index estimation using vegetation indices

4.3.1. Leaf area index estimation with vegetation indices using reflectance spectra

LAI was predicted broadly using vegetation indices (Broge and Leblanc, 2001; Darvishzadeh et al., 2006; Elvidge and Chen, 1995; Schlerf et al., 2005; Wang et al., 2005; Xue and Su, 2017). Most of the vegetation indices used in this research were adapted from Neinavaz et al. (2019). From the outcomes of that study, it was expected that the MVI performs best to estimate LAI, although with a moderate outcome: an R^2 of 0.408 (Neinavaz et al., 2019). In this research, reflectance data with a higher spatial resolution are used; therefore, it was expected that the results show a higher correlation between the vegetation indices and LAI.

Using the VNIR reflectance spectra, all used vegetation indices could predict LAI with moderate accuracy ($R^2 \geq 0.3$). The best performing index using two bands was the SR ($R^2 = 0.5675$, RMSE = 0.7088), followed by the MVI and NDVI ($R^2 = 0.5582$, RMSE = 0.7165). The MVI and the NDVI score matching results throughout this research due to the formula of the indices being very similar, only differing in one constant. The best performing index using three bands was the RSR ($R^2 = 0.5815$, RMSE = 0.6972). When using only reflectance spectra in the VNIR domain, two bands are sufficient to predict LAI with reasonable accuracy ($R^2 \geq 0.5$). However, applying three bands can slightly improve the prediction accuracy, as atmospheric influence and soil background effects can be reduced (Somvanshi and Kumari, 2020; Zhu et al., 2010).

When looking at the scatterplots of the best performing vegetation indices, the SR and the RSR (Figure 16), it can be seen that the slope of the linear regression line (0.57 for SR, 0.58 for RSR) is not as steep as for a perfect fit, meaning that LAI was predicted higher for lower actual LAI values, and lower for higher actual LAI values. For the plot with the lowest measured LAI value (1.462), the LAI was overestimated a lot, getting a predicted LAI value of nearly three. The reason for this is the understory that was present in the plot; while the in-situ measurements did not cover the understory, it is of influence in the images captured by means of UAS. The predicted LAI is not exceeding a value of about five, indicating a saturation for high LAI. According to previous studies, this is expected when estimating LAI using VNIR/SWIR data (Asner et al., 2003; Gower et al., 1999; Sellers, 1985).

4.3.2. Leaf area index estimation with vegetation indices using reflectance spectra and land surface temperature

When comparing the results of LAI prediction using vegetation indices with LST inclusion with reflectance spectra (Table 8) with the results of LAI prediction using vegetation indices with only the reflectance spectra (Table 7), it is clear that the integration of LST did not improve the results. Our findings revealed that the SR (i.e., using LST and NIR reflectance as bands) was the best performing index for both flight heights. In this regard, the predicted LAI only ranges between three and five, with lower LAI values being overestimated and higher LAI values being underestimated.

LST_{120} has a lower accuracy for predicting LAI using vegetation indices than LST_{85} does for the SR, MVI, NDVI, ASR, and ANDVI. Therefore, even though the results of LST_{85} are also not very promising, it is visible that, when evaluating with R^2 and RMSE, LST_{120} scores worse. In other words, it seems that the LST values of the lower altitude are more accurate. As mentioned previously (i.e., section 4.2.2), both LST_{85} and LST_{120} do not have a strong relationship with LAI and their integration with the VNIR reflectance spectra in vegetation indices does not provide promising results. This confirms previous

findings, which stated that the relationship between LAI and LST is not significant, and the integration of LST with reflectance spectra to estimate LAI does not yield accurate results (Neinavaz et al., 2019).

4.3.3. Leaf area index estimation with vegetation indices using reflectance spectra and land surface emissivity

Previously, it was revealed that LSE is having a better relationship with LAI than LST (Neinavaz et al., 2019). Therefore, it was expected that the LAI prediction accuracy using vegetation indices would also yield better results when including LSE as an input. The LAI prediction accuracy was promising (R^2 = 0.7458, RMSE = 0.5081) when using the RSR. However, prediction accuracy was not improved and, in fact, dropped using other vegetation indices in comparison with using only reflectance spectra (Table 9). These indices are mostly ratio-based. This could infer that while LSE has a high correlation with LAI, a ratio between LSE and reflectance spectra reduces its worth and ability to infer about the LAI. The RSR was developed as a vegetation index to improve the SR by reducing the effect of soil background reflectance with the inclusion of a third band, which would filter the results of the SR (Brown et al., 2000). With LSE_{LICOR} as the third band, the prediction accuracy of LAI could be improved when comparing to the SR using only VNIR reflectance spectra. Another benefit of the RSR is that it unifies different vegetation species to estimate LAI, making it a good predictor for mixed areas (Brown et al., 2000). This is also a factor that is of relevance in the study area of this research.

R^2 for LAI estimation with the inclusion of LSE_{CHM} is below 0.3 for all vegetation indices. While P_V calculated using the CHM may give some information about the state of the vegetation, the LSE values calculated with it seem to be inadequate for LAI prediction using vegetation indices. LAI predicted with the RSR as the best performing index using LSE_{LICOR} has an outlier at LAI below 2 (Figure 18). With low LAI, the background emissivity of the soil has a significant influence (Olioso, 1995). Due to the equation used to calculate LSE using the NDVI-threshold method (equation 2c), LSE is more affected by soil emissivity when P_V values are low. For both LAI estimation with LSE_{LICOR} and LSE_{CHM}, a saturation is again visible for LAI values above 4.5 (Figure 18). As previously explained, this is because the LSE calculation with the NDVI-threshold method is highly dependent on P_V (Neinavaz et al., 2020). Previous research found that saturation can occur for high LAI values using emissivity spectra in the TIR domain to predict LAI(Neinavaz et al., 2016b). The fact that saturation occurs in this research confirms these findings.

4.4. Leaf area index estimation using partial least squares regression

4.4.1. Reflectance spectra for leaf area index estimation using partial least squares regression

In addition to the approach using vegetation indices, LAI was successfully estimated using PLSR. In previous research, it was noted that PLSR could improve the LAI prediction accuracy compared to vegetation indices, as PLSR utilizes all available spectral information, while vegetation indices only use two or three inputs (Darvishzadeh et al., 2008; Neinavaz et al., 2016a). However, when using only the VNIR reflectance spectra as input for the PLSR, this research proves the statement wrong. The prediction accuracy of the LAI using PLSR is lower (R^2=0.4452) than the best performing vegetation index (R^2 = 0.5815, RSR). The best performing vegetation indices using VNIR reflectance spectra are ratio-based (i.e., RSR), mainly using vegetation characteristics in the NIR domain in relation to characteristics in the VIS domain. At the same time, PLSR creates a regression model with new variables (PLS components) made of all inputs. Our findings revealed that for LAI values above five, the prediction accuracy is underestimated, while for LAI values below three, the prediction accuracy is overestimated. In particular, for those plots which have lower LAI value and are highly influenced by understory in the plot, the predicted LAI is higher.

4.4.2. Integration of land surface temperature and reflectance spectra for leaf area index estimation using partial least squares regression

Including LST as an additional input for the PLSR analysis yielded different results depending on whether LST_{85} or LST_{120} was used. Adding LST_{85} improved the estimation of LAI compared to using only reflectance spectra and applying vegetation indices. This is in agreement with the findings of Darvishzadeh *et al.* (2008), who showed that PLSR could improve the LAI prediction accuracy compared to vegetation indices over the VNIR and SWIR domains, and Neinavaz *et al.* (2016b), who revealed that PLSR could improve the prediction accuracy of LAI using the integration of VNIR and TIR data. The reason for an improvement to predict LAI with PLSR compared to vegetation indices when integrating LST with reflectance spectra is the limited amount of spectral information available with vegetation indices (Lee et al., 2004), making use of only two or three bands. With PLSR, it has been found that increasing the number of informative components can correspond to more relevant predictor variables (Cramer, 1993). Therefore, when including LST as an extra input to the PLSR model, the optimal number of PLS components increases from two to three compared to using only the reflectance spectra, meaning that LST helps create a third relevant predictor variable. Including LST_{120} as input in PLSR, results also show higher accuracy than when using vegetation indices; however, no improvements compared to PLSR using only reflectance spectra are visible. This indicates that the lower altitude provides better data to integrate into the LAI prediction process.

4.4.3. Integration of land surface emissivity with leaf area index estimation using partial least squares regression

Analogous, LSE was introduced as an input to the PLSR analysis. Our finding demonstrated that the combination of LSE_{LICOR} and reflectance spectra could significantly boost the LAI prediction accuracy (R^2 = 0.7907). As LSE has a significant correlation with LAI (Neinavaz et al., 2019), it was expected that its inclusion with VNIR data into the PLSR model results in predictor variables that can explain the variability of LAI with significant accuracy. Like the addition of LST, the additional variable added with LSE allows the model to create more relevant predictor variables that can explain LAI. In Figure 22a, it can be seen that the predicted fit of estimated LAI compared to the measured LAI is not far from the optimal one on one fit. However, there is still saturation visible for LAI above 4.5, the reasons being the same as previously mentioned when discussing LAI predictability with integration with LSE (sections 4.1.3 and 4.2.3), which is in agreement with previous research (Neinavaz et al., 2016b).

4.4.4. Leaf area index estimation with partial least squares regression considering different dominant species

As TIR data was used previously with success to distinguish different species (Ribeiro da Luz and Crowley, 2010; Ullah et al., 2012) and also LAI was predicted with reasonable accuracy using TIR hyperspectral data under laboratory conditions (Neinavaz et al., 2016a), it was expected that differences in prediction accuracy would also be visible in this research. Research in the laboratory setup also showed that for the mixed dataset, the LAI prediction accuracy dropped compared to when a single species has considered (Neinavaz et al., 2016a).

This research confirmed these previous findings through PLSR analysis differentiated by dominant species. The results revealed that for the oak plots, LAI prediction accuracy did not increase using reflectance spectra with and without integration of LST, whereas by including LSE with reflectance spectra LAI prediction accuracy improved (Table 11). For plots dominant by beech, prediction accuracy was increased using reflectance spectra as well as reflectance spectra in combination with LST or LSE. For

mixed plots, oak plots, and beech plots, the integration of reflectance spectra with LSE_{LICOR} consistently achieved the best result; compared to mixed plots, the accuracy is increased further when analysing only oak or beech plots. This is because emissivity in the TIR domain can be different for plants of different ecological groups and species (Rock et al., 2016). It should, however, be noted that the small sample size of oak plots (n=10) precludes an accurate statistical evaluation.

4.5. Recommendations for further research

An improvement to this research could be made by focusing on the quality of the TIR data collected by the UAS. As was mentioned in section 4.1.2, the collection of TIR images using the FLIR Vue Pro R was done only above the plots, introducing spatial insecurity. A solution would be to cover the study area for TIR data acquisition similar to the data collection with the Parrot Sequoia by taking thousands of images that could be combined to orthomosaics using suitable software. This process would also make the overlay of the TIR and the VNIR data easier. Furthermore, both the images from the FLIR Vue R Pro and the Parrot Sequoia have a relatively high spatial resolution, allowing the plot size to be smaller. This plot size was chosen in this research to allow for comparison with Landsat-8 data, for which the pixel size is 30 by 30 m. Landsat-8 data could not be used in this research, however, as a cloud cover during the overpass of the satellite in the desired time frame prevented the use of its data. If possible, research including Landsat-8 data should be considered. Decreasing the plot size makes LAI in-situ measurements more accurate, and with the same size of the study area, more sample plots can be taken.

A challenge of this research was the calculation of LSE. Since measurements with the FLIR Vue Pro R were directly converted to LST instead of spectral radiance, LSE had to be calculated using the NDVI-threshold method (explained in section 2.3.3), which considered as a practical approach, however, is dependent on the high accuracy of P_V (Neinavaz et al., 2020). In the case that more TIR spectral bands are available, other approaches like the temperature/emissivity separation (TES) algorithm (Gillespie et al., 1998) can be used, which can get more accurate results for the calculation of LSE, and therefore also more accurate predictions of LAI can be expected. Hyperspectral TIR sensors have been proven beneficial to estimate LAI in laboratory conditions (Neinavaz et al., 2016a, 2016b); hence an application with a UAS and a TIR hyperspectral sensor should be able to increase the LAI prediction accuracy as well. Future studies using such a setup could close the gap between small-scale setups like in the laboratory and research in environments using low-resolution satellite data (Gerhards et al., 2018).

The NDVI-threshold method is highly influenced by P_V (Neinavaz et al., 2020). In this research, P_V was obtained from two different approaches, demonstrating its significance and, as a result, its influence on the LSE results. P_V from in-situ measurements yielded very accurate results, while P_V from a CHM got less accurate results. It is also recommended to investigate different approaches to estimate P_V, as in-situ measurements are not always available.

5. CONCLUSION

So far, research on the predictability of LAI with the integration of TIR with VNIR data on a canopy level has only been done using Landsat-8 data (Neinavaz et al., 2019). To further improve the knowledge about the integration of TIR with VNIR data to predict the LAI, this study looked at using images captured by means of UAS for a mixed forest, the Haagse Bos, North of Enschede, the Netherlands. Analysis was done using VNIR reflectance spectra extracted from images of the Parrot Sequoia multispectral sensor, LST extracted from images of the FLIR Vue R Pro TIR camera, LSE calculated using the NDVI-threshold method, and LAI in-situ measurements collected from the LICOR 2200C. Two different approaches were used to estimate LAI: vegetation indices as well as PLSR.

The results of this study demonstrate that it is possible to improve the LAI prediction accuracy when integrating VNIR with TIR data, using both vegetation indices as well as PLSR. Confirming Neinavaz et al. (2019), the relationship between LAI and LST was not found to be significant, while a good relationship between LAI and LSE was proven. This research proves that the integration of LSE with reflectance spectra could significantly improve LAI prediction accuracy when comparing to using only the reflectance spectra; when using vegetation indices, LSE can successfully be included as a third band in the RSR, and PLSR results are increased when adding LSE as an input.

Furthermore, the results also highlight the importance of accurate P_V measurements when calculating LSE with the NDVI-threshold method, as two different approaches were used. LSE from P_V in-situ measurements yielded the best results when integrating with reflectance spectra to estimate LAI, while LSE from P_V estimated through a CHM did not get very good results. In addition, the prediction accuracy of LAI with the integration of LST with reflectance spectra was investigated from two different flight heights. Although LST, regardless of the altitude from which it was obtained, did not yield very accurate results, it was demonstrated that LST from the 85 m altitude performed better than LST from the 120 m altitude, as integration of LST with reflectance spectra using PLSR could marginally increase the LAI prediction accuracy.

Another finding of this research is the improvement of LAI predictability when differentiating by species. PLSR analysis was performed for all plots divided by their dominant species, resulting in two datasets: plots with oak or beech as their dominant species. When using the integration of LSE with reflectance spectra, results improved significantly for both the oak and the beech dataset compared to the complete, mixed dataset. Further research is required to assess the differences in LAI predictability for different vegetation species and environments.

This study proves that TIR remote sensed data could be of great value when assessing vegetation parameters like the LAI, which proves to be valuable for future climate and biodiversity studies and applications. Research should focus on the different approaches to estimate the LAI with the integration of TIR data, especially with LSE integration. TIR hyperspectral sensors could introduce more improved results; also, using different methods to calculate LSE should be looked into.

5.1. Answers to the research questions

- How will the prediction accuracy of the LAI be increased for a mixed forest with the integration of UAS-obtained TIR and VNIR data applying vegetation indices, compared to utilizing only VNIR data?

This research indicates that the LAI prediction accuracy for a mixed forest can be increased by integrating TIR with VNIR data using UAS images applying vegetation indices when using LSE. LST inclusion as input for vegetation indices does not improve the LAI prediction accuracy compared to only using VNIR reflectance spectra. The inclusion of LSE can improve the results of LAI prediction accuracy compared to using only VNIR reflectance spectra, using both vegetation indices and PLSR. When the LAI was estimated using the RSR with LSE as the third band, higher accuracy was obtained ($R^2 = 0.7458$, RMSE = 0.5081). It has to be noted that LSE was calculated using the NDVI-threshold method and is therefore highly dependent on accurate values for P_V, which was measured in-situ for the approach which yielded the mentioned result.

- How will the prediction accuracy of the LAI be increased for a mixed forest with the integration of UAS-obtained TIR and VNIR data applying partial least squares regression, compared to utilizing only VNIR data?

Using PLSR analysis to predict LAI for a mixed forest, the prediction accuracy could be improved by including TIR combined with VNIR data. Compared to using only VNIR reflectance spectra, the LAI prediction accuracy was improved when including LST from TIR images captured from an 85 m flight height; images from a 120 m flight height did not provide LST values able to improve the results. Best results ($R^2 = 0.7907$) were achieved when including LSE, calculated with the NDVI-threshold method using in-situ measured P_V.

- What are the effects on the prediction accuracy of the LAI of different flight heights of the UAS for TIR data acquisition for the mixed forest using UAS-TIR data?

The effect of different flight heights of the UAS on the LAI prediction accuracy for a mixed forest was evaluated by comparing the integration of LST from the different heights (85 m and 120 m) with VNIR reflectance spectra. This was done using vegetation indices as well as with PLSR. With both approaches, integrating LST from the lower flight height achieved better results. For the same plots, the LST values from the different altitudes showed different values, indicating influences of the atmosphere or possible measurement errors.

LIST OF REFERENCES

Addai, I.K., Alimiyawo, M., 2015. Graphical determination of leaf area index and its relationship with growth and yield parameters of Sorghum (Sorghum bicolor L. Moench) as affected by fertilizer application. J. Agron. 14, 272–278. https://doi.org/10.3923/ja.2015.272.278

Anderegg, W.R.L., Prall, J.W., Harold, J., Schneider, S.H., 2010. Expert credibility in climate change. Proc. Natl. Acad. Sci. U. S. A. 107, 12107–12109. https://doi.org/10.1073/pnas.1003187107

Anderson, M.C., 1971. Radiation and crop structure, in: Sestak, Z., Catsky, J., Jarvis, P.G. (Eds.), Plant Photosynthetic Production: Manual of Methods. Junk, W., The Hague, pp. 77–90.

Asner, G.P., 1998. Biophysical and biochemical sources of variability in canopy reflectance. Remote Sens. Environ. 64, 234–253. https://doi.org/10.1016/S0034-4257(98)00014-5

Asner, G.P., Scurlock, J.M.O., A. Hicke, J., 2003. Global synthesis of leaf area index observations: implications for ecological and remote sensing studies. Glob. Ecol. Biogeogr. 12, 191–205. https://doi.org/10.1046/j.1466-822X.2003.00026.x

Baldridge, A.M., Hook, S.J., Grove, C.I., Rivera, G., 2008. The ASTER spectral library version 2.0. Remote Sens. Environ. 113, 711–715. https://doi.org/10.1016/j.rse.2008.11.007

Berni, J.A.J., Zarco-Tejada, P.J., Suárez, L., Fereres, E., 2009. Thermal and narrowband multispectral remote sensing for vegetation monitoring from an unmanned aerial vehicle. IEEE Trans. Geosci. Remote Sens. 47, 722–738. https://doi.org/10.1109/TGRS.2008.2010457

Bojinski, S., Verstraete, M., Peterson, T.C., Richter, C., Simmons, A., Zemp, M., 2014. The concept of essential climate variables in support of climate research, applications, and policy. Bull. Am. Meteorol. Soc. 95, 1431–1443. https://doi.org/10.1175/BAMS-D-13-00047.1

Bonan, G.B., 1993. Importance of leaf area index and forest type when estimating photosynthesis in boreal forests. Remote Sens. Environ. 43, 303–314.

Boubanga-Tombet, S., Marcotte, F., Guyot, É., Chamberland, M., Farley, V., 2019. Toward UAV based compact thermal infrared hyperspectral imaging solution for real-time gas detection identification and quantification (Conference Presentation). SPIE-Intl Soc Optical Eng, p. 36. https://doi.org/10.1117/12.2521191

Bréda, N.J.J., 2003. Ground-based measurements of leaf area index: A review of methods, instruments and current controversies. J. Exp. Bot. https://doi.org/10.1093/jxb/erg263

Broge, N.H., Leblanc, E., 2001. Comparing prediction power and stability of broadband and hyperspectral vegetation indices for estimation of green leaf area index and canopy chlorophyll density. Remote Sens. Environ. 76, 156–172. https://doi.org/10.1016/S0034-4257(00)00197-8

Brown, L., 2000. A Shortwave Infrared Modification to the Simple Ratio for LAI Retrieval in Boreal Forests An Image and Model Analysis. Remote Sens. Environ. 71, 16–25. https://doi.org/10.1016/S0034-4257(99)00035-8

Brown, L., Chen, J.M., Leblanc, S.G., Cihlar, J., 2000. A shortwave infrared modification to the simple ratio for LAI retrieval in boreal forests: An image and model analysis. Remote Sens. Environ. 71, 16–25. https://doi.org/10.1016/S0034-4257(99)00035-8

Chang, C., Song, G., Hao, Y., 2019. Exploring the relationships between normalized difference vegetation index and leaf area index in central taiwan.

Chen, J.M., 1996. Evaluation of vegetation indices and a modified simple ratio for boreal applications. Can. J. Remote Sens. 22, 229–242. https://doi.org/10.1080/07038992.1996.10855178

Chen, J.M., Black, T.A., 1992. Defining leaf area index for non-flat leaves. Plant, Cell Environ. 15, 421–429. https://doi.org/10.1111/j.1365-3040.1992.tb00992.x

Chen, J.M., Cihlar, J., 1996. Retrieving leaf area index of boreal conifer forests using landsat TM images. Remote Sens. Environ. 55, 153–162. https://doi.org/10.1016/0034-4257(95)00195-6

Chen, S., Laefer, D.F., Mangina, E., 2016. State of Technology Review of Civilian UAVs. Recent Patents Eng. 10, 160–174.

Cho, M.A., Skidmore, A., Corsi, F., van Wieren, S.E., Sobhan, I., 2007. Estimation of green grass/herb biomass from airborne hyperspectral imagery using spectral indices and partial least squares regression. Int. J. Appl. Earth Obs. Geoinf. 9, 414–424. https://doi.org/10.1016/j.jag.2007.02.001

Clerbaux, C., Drummond, J.R., Flaud, J.-M., Orphal, J., 2011. Using Thermal Infrared Absorption and Emission to Determine Trace Gases, in: The Remote Sensing of Tropospheric Composition from Space. Springer, Berlin, Heidelberg, pp. 123–151. https://doi.org/10.1007/978-3-642-14791-3_3

Climate-Data.org, n.d. Klimaat Enschede [WWW Document]. URL https://nl.climate-data.org/europa/koninkrijk-der-nederlanden/overijssel/enschede-924/ (accessed 8.6.20).
Colomina, I., Molina, P., 2014. Unmanned aerial systems for photogrammetry and remote sensing: A review. ISPRS J. Photogramm. Remote Sens. https://doi.org/10.1016/j.isprsjprs.2014.02.013
Comba, L., Biglia, A., Ricauda Aimonino, D., Tortia, C., Mania, E., Guidoni, S., Gay, P., 2020. Leaf Area Index evaluation in vineyards using 3D point clouds from UAV imagery. Precis. Agric. 21, 881–896. https://doi.org/10.1007/s11119-019-09699-x
Cowley, D., Moriarty, C., Geddes, G., Brown, G., Wade, T., Nichol, C., 2017. UAVs in Context: Archaeological Airborne Recording in a National Body of Survey and Record. Drones 2, 2. https://doi.org/10.3390/drones2010002
Cramer, R.D., 1993. Partial Least Squares (PLS): Its strengths and limitations. Perspect. Drug Discov. Des. 1, 269–278. https://doi.org/10.1007/BF02174528
Danner, M., Locherer, M., Hank, T., Richter, K., 2015. Measuring Leaf Area Index (LAI) with the LI-Cor LAI 2200C or LAI-2200 (+ 2200Clear Kit) EnMAP Field Guides Technical Report. https://doi.org/10.2312/enmap.2015.009
Darvishzadeh, R., Atzberger, C., Skidmore, A., 2006. Hyperspectral vegetation indices for estimation of leaf area index.
Darvishzadeh, R., Atzberger, C., Skidmore, A.K., Abkar, A.A., 2009. Leaf Area Index derivation from hyperspectral vegetation indicesand the red edge position. Int. J. Remote Sens. 30, 6199–6218. https://doi.org/10.1080/01431160902842342
Darvishzadeh, R., Skidmore, A., Schlerf, M., Atzberger, C., Corsi, F., Cho, M., 2008. LAI and chlorophyll estimation for a heterogeneous grassland using hyperspectral measurements. ISPRS J. Photogramm. Remote Sens. 63, 409–426. https://doi.org/10.1016/j.isprsjprs.2008.01.001
DJI, n.d. Phantom 4 - DJI [WWW Document]. URL https://www.dji.com/nl/phantom-4 (accessed 3.29.21).
Doherty, S.J., Bojinski, S., Henderson-Sellers, A., Noone, K., Goodrich, D., Bindoff, N.L., Church, J.A., Hibbard, K.A., Karl, T.R., Kajfez-Bogataj, L., Lynch, A.H., Parker, D.E., Prentice, C.L., Ramaswamy, V., Saunders, R.W., Smith, M.S., Steffen, K., Stocker, T.F., Thorne, P.W., Trenberth, K.E., Verstraete, M.M., Zwiers, F.W., 2009. Lessons learned from IPCC AR4: Scientific developments needed to understand, predict, and respond to climate change. Bull. Am. Meteorol. Soc. 90, 497–513. https://doi.org/10.1175/2008BAMS2643.1
Döpper, V., Gränzig, T., Kleinschmit, B., Förster, M., 2020. Challenges in UAS-based TIR imagery processing: Image alignment and uncertainty quantification. Remote Sens. 12, 1552. https://doi.org/10.3390/rs12101552
Drake, B.G., Raschke, K., Salisbury, F.B., 1970. Temperature and Transpiration Resistances of Leaves as Affected by Air Temperature, Humidity, and Wind Speed. Plant Physiol. 46, 324 LP – 330. https://doi.org/10.1104/pp.46.2.324
Duan, B., Liu, Y., Gong, Y., Peng, Y., Wu, X., Zhu, R., Fang, S., 2019. Remote estimation of rice LAI based on Fourier spectrum texture from UAV image. Plant Methods 15, 1–12. https://doi.org/10.1186/s13007-019-0507-8
Duda, R.O., Hart, P.E., Stork, D.G., 1995. Pattern Classiication and Scene Analysis 2nd ed. Part 1: Pattern Classiication.
Elvidge, C.D., Chen, Z., 1995. Comparison of broad-band and narrow-band red and near-infrared vegetation indices. Remote Sens. Environ. 54, 38–48. https://doi.org/10.1016/0034-4257(95)00132-K
Eshetae, M.A., 2020. Tree species classification using UAV-RGB images and machine learning algorithms in a mixed temperate forest: a case study of Haagse Bos, Netherlands. University of Twente.
FLIR Systems Inc, 2021. FLIR sUAS cameras Radiometric Information [WWW Document]. URL https://flir.custhelp.com/app/answers/detail/a_id/3108/~/flir-suas-cameras-radiometric-information (accessed 3.2.21).
FLIR Systems Inc, 2016. Vue Pro and Vue Pro R User Guide.
French, A.N., Schmugge, T.J., Kustas, W.P., 2000. Discrimination of senescent vegetation using thermal emissivity contrast. Remote Sens. Environ. 74, 249–254. https://doi.org/10.1016/S0034-4257(00)00115-2
Fumera, J.O., 2020. Estimating corn (Zea mays L.) Lai using UAV-derived vegetation indices.
Gates, D.M., 1980. Biophysical ecology. Springer Verlag, New-York, Inc., Mineola, New York.
Gates, D.M., Tantraporn, W., 1952. The reflectivity of deciduous trees and herbaceous plants in the

infrared to 25 microns. Science (80-.). 115, 613–616. https://doi.org/10.1126/science.115.2997.613
Geladi, P., Kowalski, B.R., 1986. Partial least-squares regression: a tutorial. Anal. Chim. Acta 185, 1–17. https://doi.org/10.1016/0003-2670(86)80028-9
Georgiadou, Y., Reckien, D., 2018. Geo-Information Tools, Governance, and Wicked Policy Problems. ISPRS Int. J. Geo-Information 7, 21. https://doi.org/10.3390/ijgi7010021
Gerhards, M., Schlerf, M., Rascher, U., Udelhoven, T., Juszczak, R., Alberti, G., Miglietta, F., Inoue, Y., 2018. Analysis of Airborne Optical and Thermal Imagery for Detection of Water Stress Symptoms. Remote Sens. 10, 1139. https://doi.org/10.3390/rs10071139
Gillespie, A., Rokugawa, S., Matsunaga, T., Steven Cothern, J., Hook, S., Kahle, A.B., 1998. A temperature and emissivity separation algorithm for advanced spaceborne thermal emission and reflection radiometer (ASTER) images. IEEE Trans. Geosci. Remote Sens. 36, 1113–1126. https://doi.org/10.1109/36.700995
Gomis-Cebolla, J., Jimenez, J.C., Sobrino, J.A., 2018. LST retrieval algorithm adapted to the Amazon evergreen forests using MODIS data. Remote Sens. Environ. 204, 401–411. https://doi.org/10.1016/j.rse.2017.10.015
Göttsche, F.M., Hulley, G.C., 2012. Validation of six satellite-retrieved land surface emissivity products over two land cover types in a hyper-arid region. Remote Sens. Environ. 124, 149–158. https://doi.org/10.1016/j.rse.2012.05.010
Gower, S.T., Kucharik, C.J., Norman, J.M., 1999. Direct and indirect estimation of leaf area index, f(APAR), and net primary production of terrestrial ecosystems. Remote Sens. Environ. 70, 29–51. https://doi.org/10.1016/S0034-4257(99)00056-5
Guo, X., Wang, L., Tian, J., Yin, D., Shi, C., Nie, S., 2018. Vegetation Horizontal Occlusion Index (VHOI) from TLS and UAV Image to Better Measure Mangrove LAI. Remote Sens. 10, 1739. https://doi.org/10.3390/rs10111739
Heinemann, S., Siegmann, B., Thonfeld, F., Muro, J., Jedmowski, C., Kemna, A., Kraska, T., Muller, O., Schultz, J., Udelhoven, T., Wilke, N., Rascher, U., 2020. Land Surface Temperature Retrieval for Agricultural Areas Using a Novel UAV Platform Equipped with a Thermal Infrared and Multispectral Sensor. Remote Sens. 12, 1075. https://doi.org/10.3390/rs12071075
Hoppe, R., 2010. The Governance of Problems: Puzzling, Powering and Participation. Policy Press.
Huete, A., Didan, K., Miura, T., Rodriguez, E.P., Gao, X., Ferreira, L.G., 2002. Overview of the radiometric and biophysical performance of the MODIS vegetation indices. Remote Sens. Environ. 83, 195–213. https://doi.org/10.1016/S0034-4257(02)00096-2
IPCC, 2014. Climate Change 2014: Synthesis Report. Contribution of Working Groups I, II and III to the Fifth Assessment Report of the Intergovernmental Panel on Climate Change, Kristin Seyboth (USA). Gian-Kasper Plattner, Geneva, Switzerland.
IPCC, n.d. About — IPCC [WWW Document]. URL https://www.ipcc.ch/about/ (accessed 4.15.21).
Jacob, F., Lesaignoux, A., Olioso, A., Weiss, M., Caillault, K., Jacquemoud, S., Nerry, F., French, A., Schmugge, T., Briottet, X., Lagouarde, J.P., 2017. Reassessment of the temperature-emissivity separation from multispectral thermal infrared data: Introducing the impact of vegetation canopy by simulating the cavity effect with the SAIL-Thermique model. Remote Sens. Environ. 198, 160–172. https://doi.org/10.1016/j.rse.2017.06.006
Jensen, A.M., McKee, M., Chen, Y., 2014. Procedures for processing thermal images using low-cost microbolometer cameras for small unmanned aerial systems, in: International Geoscience and Remote Sensing Symposium (IGARSS). Institute of Electrical and Electronics Engineers Inc., pp. 2629–2632. https://doi.org/10.1109/IGARSS.2014.6947013
Jensen, J., 2009. Remote sensing of the environment: An earth resource perspective 2/e.
Jiang, Z., Huete, A.R., Didan, K., Miura, T., 2008. Development of a two-band enhanced vegetation index without a blue band. Remote Sens. Environ. 112, 3833–3845. https://doi.org/10.1016/j.rse.2008.06.006
Jiménez-Muñoz, J.C., Sobrino, J.A., Gillespie, A., Sabol, D., Gustafson, W.T., 2006. Improved land surface emissivities over agricultural areas using ASTER NDVI. Remote Sens. Environ. 103, 474–487. https://doi.org/10.1016/j.rse.2006.04.012
Jin, M., Liang, S., 2006. An improved land surface emissivity parameter for land surface models using global remote sensing observations. J. Clim. 19, 2867–2881. https://doi.org/10.1175/JCLI3720.1
Jones, H., 1992. Plants and Microclimate [WWW Document]. URL https://www.researchgate.net/publication/201998606_Plants_and_Microclimate (accessed 8.6.20).
Jordan, C.F., 1969. Derivation of Leaf-Area Index from Quality of Light on the Forest Floor. Ecology 50,

663–666. https://doi.org/10.2307/1936256
Kanning, M., Kühling, I., Trautz, D., Jarmer, T., 2018. High-Resolution UAV-Based Hyperspectral Imagery for LAI and Chlorophyll Estimations from Wheat for Yield Prediction. Remote Sens. 10, 2000. https://doi.org/10.3390/rs10122000
Kirkland, L., Herr, K., Keim, E., Adams, P., Salisbury, J., Hackwell, J., Treiman, A., 2002. First use of an airborne thermal infrared hyperspectral scanner for compositional mapping. Remote Sens. Environ. 80, 447–459. https://doi.org/10.1016/S0034-4257(01)00323-6
KNMI, 2021. Monthly and yearly amount of precipitation, station Twenthe [WWW Document]. URL https://cdn.knmi.nl/knmi/map/page/klimatologie/gegevens/maandgegevens/mndgeg_290_rh24.txt (accessed 2.16.21).
Kooistra, L., Salas, E.A.L., Clevers, J.G.P.W., Wehrens, R., Leuven, R.S.E.W., Nienhuis, P.H., Buydens, L.M.C., 2004. Exploring field vegetation reflectance as an indicator of soil contamination in river floodplains. Environ. Pollut. 127, 281–290. https://doi.org/10.1016/S0269-7491(03)00266-5
Kostrzewa, J., Meyer, W.H., Laband, S., Terre, W.A., Petrovich, P., Swanson, K., Sundra, C., Sener, W., Wilmott, J., 2003. Infrared microsensor payload for miniature unmanned aerial vehicles, in: Carapezza, E.M. (Ed.), Unattended Ground Sensor Technologies and Applications V. SPIE, p. 265. https://doi.org/10.1117/12.500712
Kuenzer, C., Dech, S., 2013. Thermal remote sensing Sensors, Methods, Applications, Remote Sensing and Digital Image Processing, Remote Sensing and Digital Image Processing. Springer Netherlands. https://doi.org/10.1007/978-94-007-6639-6
Kumar, D., Shekhar, S., 2015. Statistical analysis of land surface temperature-vegetation indexes relationship through thermal remote sensing. Ecotoxicol. Environ. Saf. 121, 39–44. https://doi.org/10.1016/j.ecoenv.2015.07.004
Lausch, A., Erasmi, S., King, D.J., Magdon, P., Heurich, M., 2017. Understanding forest health with Remote sensing-Part II-A review of approaches and data models. Remote Sens. https://doi.org/10.3390/rs9020129
Lee, K.S., Cohen, W.B., Kennedy, R.E., Maiersperger, T.K., Gower, S.T., 2004. Hyperspectral versus multispectral data for estimating leaf area index in four different biomes. Remote Sens. Environ. 91, 508–520. https://doi.org/10.1016/j.rse.2004.04.010
LI-COR, 2019. LAI-2200C Plant Canopz Analzyer Instruction Manual.
Li, S., Yuan, F., Ata-UI-Karim, S.T., Zheng, H., Cheng, T., Liu, X., Tian, Y., Zhu, Y., Cao, W., Cao, Q., 2019. Combining Color Indices and Textures of UAV-Based Digital Imagery for Rice LAI Estimation. Remote Sens. 11, 1763. https://doi.org/10.3390/rs11151763
Li, Z.L., Tang, B.H., Wu, H., Ren, H., Yan, G., Wan, Z., Trigo, I.F., Sobrino, J.A., 2013a. Satellite-derived land surface temperature: Current status and perspectives. Remote Sens. Environ. https://doi.org/10.1016/j.rse.2012.12.008
Li, Z.L., Wu, H., Wang, N., Qiu, S., Sobrino, J.A., Wan, Z., Tang, B.-H., Yan, G., 2013b. Land surface emissivity retrieval from satellite data. Int. J. Remote Sens. 34, 3084–3127. https://doi.org/10.1080/01431161.2012.716540
Luhmann, T., Piechel, J., Roelfs, T., 2013. Geometric calibration of thermographic cameras, in: Remote Sensing and Digital Image Processing. Springer International Publishing, pp. 27–42. https://doi.org/10.1007/978-94-007-6639-6_2
Maes, W., Huete, A., Steppe, K., 2017. Optimizing the Processing of UAV-Based Thermal Imagery. Remote Sens. 9, 476. https://doi.org/10.3390/rs9050476
Maimaitiyiming, M., Ghulam, A., Tiyip, T., Pla, F., Latorre-Carmona, P., Halik, Ü., Sawut, M., Caetano, M., 2014. Effects of green space spatial pattern on land surface temperature: Implications for sustainable urban planning and climate change adaptation. ISPRS J. Photogramm. Remote Sens. 89, 59–66. https://doi.org/10.1016/j.isprsjprs.2013.12.010
MathWorks Benelux, n.d. Partial least-squares regression - MATLAB plsregress [WWW Document]. URL https://nl.mathworks.com/help/stats/plsregress.html (accessed 2.26.21).
Matsushita, B., Xu, M., Chen, J., Kameyama, S., Tamura, M., 2004. Estimation of regional net primary productivity (NPP) using a process-based ecosystem model: How important is the accuracy of climate data? Ecol. Modell. 178, 371–388. https://doi.org/10.1016/j.ecolmodel.2004.03.012
McKinney, M.L., Schoch, R.M., 2003. Environmental Science: Systems and Solutions. Jones & Bartlett Learning.
Meerdink, S.K., Hook, S.J., Roberts, D.A., Abbott, E.A., 2019. The ECOSTRESS spectral library version 1.0. Remote Sens. Environ. 230, 111196. https://doi.org/10.1016/j.rse.2019.05.015

Meier, F., Scherer, D., Richters, J., Christen, A., 2011. Atmospheric correction of thermal-infrared imagery of the 3-D urban environment acquired in oblique viewing geometry. Atmos. Meas. Tech 4, 909–922. https://doi.org/10.5194/amt-4-909-2011

Messina, G., Modica, G., 2020. Applications of UAV thermal imagery in precision agriculture: State of the art and future research outlook. Remote Sens. https://doi.org/10.3390/RS12091491

Mitchard, E., 2016. A Review of Earth Observation Methods for Detecting and Measuring Forest Change in the Tropics.

Neinavaz, E., 2017. Sensing Vegetation Canopies in the Thermal Domain. University of Twente. https://doi.org/10.3990/1.9789036543514

Neinavaz, E., Darvishzadeh, R., Skidmore, A.K., 2020. Effects of prediction accuracy of the proportion of vegetation cover on land surface emissivity and temperature using the NDVI threshold method. Int. J. Appl. Earth Obs. Geoinf. 85, 101984. https://doi.org/10.1016/j.jag.2019.101984

Neinavaz, E., Darvishzadeh, R., Skidmore, A.K., Abdullah, H., 2019. Integration of Landsat-8 thermal and visible-short wave infrared data for improving prediction accuracy of forest leaf area index. Remote Sens. 11. https://doi.org/10.3390/rs11040390

Neinavaz, E., Darvishzadeh, R., Skidmore, A.K., Groen, T.A., 2016a. Retrieval of leaf area index in different plant species using thermal hyperspectral data. ISPRS J. Photogramm. Remote Sens. 119, 390–401. https://doi.org/10.1016/j.isprsjprs.2016.07.001

Neinavaz, E., Darvishzadeh, R., Skidmore, A.K., Groen, T.A., 2016b. Measuring the response of canopy emissivity spectra to leaf area index variation using thermal hyperspectral data. Int. J. Appl. Earth Obs. Geoinf. 53, 40–47. https://doi.org/10.1016/j.jag.2016.08.002

Ogawa, K., Schmugge, T., Rokugawa, S., 2008. Estimating broadband emissivity of arid regions and its seasonal variations using thermal infrared remote sensing, in: IEEE Transactions on Geoscience and Remote Sensing. pp. 334–343. https://doi.org/10.1109/TGRS.2007.913213

Olioso, A., 1995. Simulating the relationship between thermal emissivity and the normalized difference vegetation index. Int. J. Remote Sens. 16, 3211–3216. https://doi.org/10.1080/01431169508954625

Olioso, A., Sòria, G., Sobrino, J., Duchemin, B., 2007. Evidence of low land surface thermal infrared emissivity in the presence of dry vegetation. IEEE Geosci. Remote Sens. Lett. 4, 112–116. https://doi.org/10.1109/LGRS.2006.885857

Oltra-Carrió, R., Sobrino, J.A., Franch, B., Nerry, F., 2012. Land surface emissivity retrieval from airborne sensor over urban areas. Remote Sens. Environ. 123, 298–305. https://doi.org/10.1016/j.rse.2012.03.007

Paltridge, G.W., Barber, J., 1988. Monitoring grassland dryness and fire potential in australia with NOAA/AVHRR data. Remote Sens. Environ. 25, 381–394. https://doi.org/10.1016/0034-4257(88)90110-1

Pereira, H.M., Ferrier, S., Walters, M., Geller, G.N., Jongman, R.H.G., Scholes, R.J., Bruford, M.W., Brummitt, N., Butchart, S.H.M., Cardoso, A.C., Coops, N.C., Dulloo, E., 2013. Essential Biodiversity Variables. Science (80-.). 339, 277–278.

Pereira, H.M., Navarro, L.M., Martins, I.S., 2012. Global biodiversity change: The Bad, the good, and the unknown. Annu. Rev. Environ. Resour. https://doi.org/10.1146/annurev-environ-042911-093511

Pope, G., Treitz, P., 2013. Leaf Area Index (LAI) estimation in boreal mixedwood forest of Ontario, Canada using Light detection and ranging (LiDAR) and worldview-2 imagery. Remote Sens. 5, 5040–5063. https://doi.org/10.3390/rs5105040

Prakash, A., 2000. Thermal Remote Sensing: Concepts, Issues and Applications. Int. Arch. Photogramm. Remote Sens. XXXIII.

Quattrochi, D.A., Luvall, J.C., 1999. Thermal infrared remote sensing for analysis of landscape ecological processes: Methods and applications. Landsc. Ecol. 14, 577–598. https://doi.org/10.1023/A:1008168910634

Ribeiro da Luz, B., 2006. Attenuated total reflectance spectroscopy of plant leaves: a tool for ecological and botanical studies. New Phytol. 172, 305–318. https://doi.org/10.1111/j.1469-8137.2006.01823.x

Ribeiro da Luz, B., Crowley, J.K., 2010. Identification of plant species by using high spatial and spectral resolution thermal infrared (8.0-13.5 μm) imagery. Remote Sens. Environ. 114, 404–413. https://doi.org/10.1016/j.rse.2009.09.019

Ribeiro da Luz, B., Crowley, J.K., 2007. Spectral reflectance and emissivity features of broad leaf plants: Prospects for remote sensing in the thermal infrared (8.0-14.0 μm). Remote Sens. Environ. 109, 393–405. https://doi.org/10.1016/j.rse.2007.01.008

Rock, G., Gerhards, M., Schlerf, M., Hecker, C., Udelhoven, T., 2016. Plant species discrimination using emissive thermal infrared imaging spectroscopy. Int. J. Appl. Earth Obs. Geoinf. 53, 16–26. https://doi.org/10.1016/j.jag.2016.08.005

Ross, J., 1981. The radiation regime and architecture of plant stands. Radiat. regime Archit. plant stands.

Roujean, J.L., Breon, F.M., 1995. Estimating PAR absorbed by vegetation from bidirectional reflectance measurements. Remote Sens. Environ. 51, 375–384. https://doi.org/10.1016/0034-4257(94)00114-3

Rouse, J.W., 1974. Monitoring the vernal advancement and retrogradation (greenwave effect) of natural vegetation.

Rufino, G., Moccia, A., 2005. Integrated VIS-NIR hyperspectral / thermal-IR electro-optical payload system for a mini-UAV, in: Collection of Technical Papers - InfoTech at Aerospace: Advancing Contemporary Aerospace Technologies and Their Integration. pp. 915–923. https://doi.org/10.2514/6.2005-7009

Sagan, V., Maimaitijiang, M., Sidike, P., Eblimit, K., Peterson, K., Hartling, S., Esposito, F., Khanal, K., Newcomb, M., Pauli, D., Ward, R., Fritschi, F., Shakoor, N., Mockler, T., 2019. UAV-Based High Resolution Thermal Imaging for Vegetation Monitoring, and Plant Phenotyping Using ICI 8640 P, FLIR Vue Pro R 640, and thermoMap Cameras. Remote Sens. 11, 330. https://doi.org/10.3390/rs11030330

Schlerf, M., Atzberger, C., Hill, J., 2005. Remote sensing of forest biophysical variables using HyMap imaging spectrometer data. Remote Sens. Environ. 95, 177–194. https://doi.org/10.1016/j.rse.2004.12.016

Scholtz, A., Kaschwich, C., Krüger, A., Kufieta, K., Schnetter, P., Wilkens, C.-S., Krüger, T., Vörsmann, P., 2011. Development of a new multi-purpose uas for scientific application. Int. Arch. Photogramm. Remote Sens. Spat. Inf. Sci. XXXVIII.

Sellers, P.J., 1985. Canopy reflectance, photosynthesis and transpiration. Int. J. Remote Sens. 6, 1335–1372. https://doi.org/10.1080/01431168508948283

Shao, J., 1993. Linear model selection by cross-validation. J. Am. Stat. Assoc. 88, 486–494. https://doi.org/10.1080/01621459.1993.10476299

Shapiro, M., Shukla, J., Brunet, G., Nobre, C., Béland, M., Dole, R., Trenberth, K., Anthes, R., Asrar, G., Barrie, L., Bougeault, P., Brasseur, G., Burridge, D., Busalacchi, A., Caughey, J., Chen, D., Church, J., Enomoto, T., Hoskins, B., Hov, Ø., Laing, A., Le Treut, H., Marotzke, J., McBean, G., Meehl, G., Miller, M., Mills, B., Mitchell, J., Moncrieff, M., Nakazawa, T., Olafsson, H., Palmer, T., Parsons, D., Rogers, D., Simmons, A., Troccoli, A., Toth, Z., Uccellini, L., Velden, C., Wallace, J.M., 2010. An Earth-system prediction initiative for the twenty-first century. Bull. Am. Meteorol. Soc. 91, 1377–1388. https://doi.org/10.1175/2010BAMS2944.1

Skidmore, A.K., Pettorelli, N., 2015. Agree on biodiversity metrics to track from space. Nature 523, 5–7. https://doi.org/10.1038/523403a

Sobrino, J.A., Caselles, V., Becker, F., 1990. Significance of the remotely sensed thermal infrared measurements obtained over a citrus orchard. ISPRS J. Photogramm. Remote Sens. 44, 343–354. https://doi.org/10.1016/0924-2716(90)90077-O

Sobrino, J.A., Jiménez-Muñoz, J.C., Paolini, L., 2004. Land surface temperature retrieval from LANDSAT TM 5. Remote Sens. Environ. 90, 434–440. https://doi.org/10.1016/j.rse.2004.02.003

Sobrino, J.A., Jiménez-Muñoz, J.C., Sòria, G., Romaguera, M., Guanter, L., Moreno, J., Plaza, A., Martínez, P., 2008. Land surface emissivity retrieval from different VNIR and TIR sensors, in: IEEE Transactions on Geoscience and Remote Sensing. pp. 316–327. https://doi.org/10.1109/TGRS.2007.904834

Sobrino, J.A., Jiménez-Muñoz, J.C., Verhoef, W., 2005. Canopy directional emissivity: Comparison between models. Remote Sens. Environ. 99, 304–314. https://doi.org/10.1016/j.rse.2005.09.005

Sobrino, J.A., Raissouni, N., 2000. Toward remote sensing methods for land cover dynamic monitoring: Application to Morocco. Int. J. Remote Sens. 21, 353–366. https://doi.org/10.1080/014311600210876

Sobrino, J.A., Raissouni, N., Li, Z.L., 2001. A comparative study of land surface emissivity retrieval from NOAA data. Remote Sens. Environ. 75, 256–266. https://doi.org/10.1016/S0034-4257(00)00171-1

Somvanshi, S.S., Kumari, M., 2020. Comparative analysis of different vegetation indices with respect to atmospheric particulate pollution using sentinel data. Appl. Comput. Geosci. 7, 100032. https://doi.org/10.1016/j.acags.2020.100032

Song, C., 2013. Optical remote sensing of forest leaf area index and biomass. Prog. Phys. Geogr. Earth

Environ. 37, 98–113. https://doi.org/10.1177/0309133312471367
Stenberg, P., Rautiainen, M., Manninen, T., Voipio, P., Smolander, H., 2004. Reduced simple ratio better than NDVI for estimating LAI in Finnish pine and spruce stands. Silva Fenn. 38, 3–14. https://doi.org/10.14214/sf.431
Tonooka, H., Palluconi, F.D., 2005. Validation of ASTER/TIR standard atmospheric correction using water surfaces. IEEE Trans. Geosci. Remote Sens. 43, 2769–2777. https://doi.org/10.1109/TGRS.2005.857883
Tucker, C.J., 1979. Red and photographic infrared linear combinations for monitoring vegetation. Remote Sens. Environ. 8, 127–150. https://doi.org/10.1016/0034-4257(79)90013-0
Ullah, S., 2013. Thermal plants: characterizing vegetation parameters using mid to thermal infrared hyperspectral remote sensing.
Ullah, S., Schlerf, M., Skidmore, A.K., Hecker, C., 2012. Identifying plant species using mid-wave infrared (2.5-6μm) and thermal infrared (8-14μm) emissivity spectra. Remote Sens. Environ. 118, 95–102. https://doi.org/10.1016/j.rse.2011.11.008
Valero, M.M., Rios, O., Mata, C., Pastor, E., Planas, E., 2017. An integrated approach for tactical monitoring and data-driven spread forecasting of wildfires. Fire Saf. J. 91, 835–844. https://doi.org/10.1016/j.firesaf.2017.03.085
Valor, E., 1996. Mapping land surface emissivity from NDVI: Application to European, African, and South American areas. Remote Sens. Environ. 57, 167–184. https://doi.org/10.1016/0034-4257(96)00039-9
Van De Griend, A.A., Owe, M., 1993. On the relationship between thermal emissivity and the normalized difference vegetation index for natural surfaces. Int. J. Remote Sens. 14, 1119–1131. https://doi.org/10.1080/01431169308904400
van den Hurk, B.J.J.M., Viterbo, P., Los, S.O., 2003. Impact of leaf area index seasonality on the annual land surface evaporation in a global circulation model. J. Geophys. Res. D Atmos. 108. https://doi.org/10.1029/2002jd002846
Vertessy, R.A., Benyon, R.G., O'Sullivan, S.K., Gribben, P.R., 1995. Relationships between stem diameter, sapwood area, leaf area and transpiration in a young mountain ash forest. Tree Physiol. 15, 559–567. https://doi.org/10.1093/TREEPHYS/15.9.559
Wang, Q., Adiku, S., Tenhunen, J., Granier, A., 2005. On the relationship of NDVI with leaf area index in a deciduous forest site. Remote Sens. Environ. 94, 244–255. https://doi.org/10.1016/j.rse.2004.10.006
Watson, D.J., Watson, M.A., 1953. Comparative physiological studies on the growth of field crops. Ann Appl. Biol. 40, 1–37.
Wong, C., Blevin, W., 1967. Infrared Reflectances of Plant Leaves. Aust. J. Biol. Sci. 20, 501. https://doi.org/10.1071/bi9670501
Xue, J., Su, B., 2017. Significant remote sensing vegetation indices: A review of developments and applications. J. Sensors. https://doi.org/10.1155/2017/1353691
Zhang, D., Liu, J., Ni, W., Sun, G., Zhang, Z., Liu, Q., Wang, Q., 2019. Estimation of Forest Leaf Area Index Using Height and Canopy Cover Information Extracted From Unmanned Aerial Vehicle Stereo Imagery. IEEE J. Sel. Top. Appl. Earth Obs. Remote Sens. 12, 471–481. https://doi.org/10.1109/JSTARS.2019.2891519
Zhang, J., Huang, Y., Pu, R., Gonzalez-Moreno, P., Yuan, L., Wu, K., Huang, W., 2019. Monitoring plant diseases and pests through remote sensing technology: A review. Comput. Electron. Agric. 165, 104943. https://doi.org/10.1016/j.compag.2019.104943
Zhang, Y., Odeh, I.O.A., Han, C., 2009. Bi-temporal characterization of land surface temperature in relation to impervious surface area, NDVI and NDBI, using a sub-pixel image analysis. Int. J. Appl. Earth Obs. Geoinf. 11, 256–264. https://doi.org/10.1016/j.jag.2009.03.001
Zheng, G., Moskal, L.M., 2009. Retrieving Leaf Area Index (LAI) Using Remote Sensing: Theories, Methods and Sensors. Sensors 9, 2719–2745. https://doi.org/10.3390/s90402719
Zhu, G., Ju, W., Chen, J.M., Zhou, Y., Li, X., Xu, X., 2010. Comparison of forest leaf area index retrieval based on simple ratio and reduced simple ratio, in: 2010 18th International Conference on Geoinformatics, Geoinformatics 2010. https://doi.org/10.1109/GEOINFORMATICS.2010.5568204
Zhu, W., Huang, Y., Sun, Z., 2018. Mapping crop leaf area index from multi-spectral imagery onboard an unmanned aerial vehicle, in: 2018 7th International Conference on Agro-Geoinformatics, Agro-Geoinformatics 2018. Institute of Electrical and Electronics Engineers Inc.

https://doi.org/10.1109/Agro-Geoinformatics.2018.8475985
Zhu, W., Sun, Z., Huang, Y., Lai, J., Li, J., Zhang, J., Yang, B., Li, B., Li, S., Zhu, K., Li, Y., Liao, X., 2019a. Improving Field-Scale Wheat LAI Retrieval Based on UAV Remote-Sensing Observations and Optimized VI-LUTs. Remote Sens. 11, 2456. https://doi.org/10.3390/rs11202456
Zhu, W., Sun, Z., Huang, Y., Lai, J., Li, J., Zhang, J., Yang, B., Li, B., Li, S., Zhu, K., Li, Y., Liao, X., 2019b. Improving field-scale wheat LAI retrieval based on UAV remote-sensing observations and optimized VI-LUTs. Remote Sens. 11, 2456. https://doi.org/10.3390/rs11202456
Zhu, X., Li, C., Tang, L., Ma, L., 2019a. Retrieval and scale effect analysis of LAI over typical farmland from UAV-based hyperspectral data, in: Neale, C.M., Maltese, A. (Eds.), Remote Sensing for Agriculture, Ecosystems, and Hydrology XXI. SPIE, p. 22. https://doi.org/10.1117/12.2535478
Zhu, X., Li, C., Tang, L., Ma, L., 2019b. Retrieval and scale effect analysis of LAI over typical farmland from UAV-based hyperspectral data. SPIE-Intl Soc Optical Eng, p. 22. https://doi.org/10.1117/12.2535478

APPENDIX I

The following table shows the data measured in-situ for all plots for which TIR images were acquired.

Plot Nr.	LAI	DIFN	Trees	Dominant species	Remarks
1	3.137	0.08326	21	Beech	Some dead wood, some cut trees
2	4.676	0.0238	18	Beech	Multiple dead trees. Plot created by measuring corners, centre approximate
3	1.462	0.3838	18	Fir	A lot of dead wood and understory. Centre approximate
4	4.778	0.02175	25	Oak	Some understory and dead wood
5	3.844	0.04739	24	Oak	Understory with a lot of young birch
6	2.39	0.1556	14	Beech	Some dead wood, some cut trees
7	4.554	0.02645	25	Oak	Very mixed canopy. Lots of understory and young birches, some dead wood
8	5.286	0.0163	25	Beech	A lot of dead wood. Very tall trees
9	4.578	0.03278	30	Beech	A lot of fallen trees and dead wood
10	2.727	0.1313	22	Oak	A lot of very small understory, some dead wood
11	4.347	0.03535	36	Beech	Only tall beech, a little dead wood
12	2.408	0.1457	31	Fir	Partly understory on the south side. Some dead wood
13	5.584	0.01117	23	Beech	Some dead wood and dead trees
14	3.507	0.06313	22	Beech	Some dead wood
15	2.664	0.1212	22	Beech	Some dead wood
16	3.346	0.06856	30	Beech	Little dead wood, grass, next to open field
17	3.775	0.04794	39	Oak	Some grass, little dead wood, next to open field
18	4.272	0.03332	33	Beech	Some dead wood, some grass
19	4.809	0.02369	26	Oak	Understory with a lot of young birch
20	3.996	0.0406	26	Beech	Partly understory with young beech, dead wood
21	4.035	0.03933	36	Beech	Dead trees (lying and standing), some understory, young beech
22	5.035	0.01751	37	Beech	Dead wood, some understory
23	4.312	0.03302	24	Beech	A lot of dead wood
24	4.964	0.01956	28	Beech	Dead wood, some understory (young beech)
25	4.554	0.03007	27	Oak	Dead wood, light understory (young beech)
26	4.635	0.02576	27	Oak	Dead wood, some understory
27	3.103	0.1087	19	Oak	Dead wood, understory with young firs and bushes
28	3.423	0.08076	36	Oak/Pine	A lot of understory, dead wood. GPS less accurate (handheld)
29	5.591	0.01131	34	Beech	A lot of dead wood. GPS less accurate (handheld)
30	5.717	0.01065	32	Beech	Dead wood. GPS less accurate (handheld)

APPENDIX II

The following table shows the mean reflectance of the VNIR reflectance spectra of the Parrot Sequoia as well as the mean LST for both flight altitudes captured with the FLIR Vue Pro R. The last column shows the difference between LST_{85} and LST_{120}.

Plot Nr.	LAI	Green reflectance	Red reflectance	Red-Edge reflectance	NIR reflectance	LST_{85} (°C)	LST_{120} (°C)	Difference LST (°C)
1	3.137	0.0494	0.0238	0.2002	0.3852	23.1892	20.6971	2.4921
2	4.676	0.0420	0.0208	0.1791	0.3423	22.5999	20.0791	2.5208
3	1.462	0.0327	0.0161	0.1182	0.2155	23.3627	19.6140	3.7487
4	4.778	0.0431	0.0203	0.1757	0.3475	22.9081	19.3946	3.5135
5	3.844	0.0425	0.0206	0.1675	0.3212	19.7918	18.5376	1.2541
6	2.39	0.0383	0.0196	0.1496	0.2878	23.8094	21.8321	1.9773
7	4.554	0.0328	0.0157	0.1196	0.2319	18.3828	22.7184	4.3356
8	5.286	0.0412	0.0212	0.1656	0.3136	21.1511	20.4004	0.7507
9	4.578	0.0394	0.0190	0.1563	0.3032	21.4210	20.7142	0.7068
10	2.727	0.0383	0.0181	0.1421	0.2643	19.1000	22.9778	3.8778
11	4.347	0.0456	0.0224	0.1993	0.3662	20.5973	23.7049	3.1076
12	2.408	0.0448	0.0223	0.1556	0.2585	20.6112	24.8330	4.2218
13	5.584	0.0404	0.0213	0.1722	0.3457	23.1905	19.6580	3.5325
14	3.507	0.0386	0.0203	0.1502	0.2721	20.8969	23.2567	2.3598
15	2.664	0.0393	0.0212	0.1529	0.2760	19.0245	24.0253	5.0008
16	3.346	0.0494	0.0260	0.2090	0.3825	24.6573	20.3643	4.2930
17	3.775	0.0499	0.0274	0.2075	0.3870	25.1935	19.3574	5.8361
18	4.272	0.0460	0.0221	0.2039	0.3942	24.1552	19.9725	4.1826
19	4.809	0.0363	0.0177	0.1551	0.3064	23.3384	19.3529	3.9855
20	3.996	0.0503	0.0230	0.2016	0.3680	22.1203	23.3020	1.1817
21	4.035	0.0371	0.0193	0.1576	0.2903	19.6329	20.9074	1.2745
22	5.035	0.0363	0.0171	0.1508	0.3000	18.6936	20.6664	1.9728
23	4.312	0.0359	0.0180	0.1541	0.2961	21.3235	23.6578	2.3343
24	4.964	0.0442	0.0206	0.1875	0.3482	21.2466	23.5066	2.2600
25	4.554	0.0394	0.0188	0.1622	0.3353	20.4434	23.3125	2.8691
26	4.635	0.0457	0.0237	0.1750	0.3302	20.7776	23.7504	2.9728
27	3.103	0.0394	0.0177	0.1487	0.2912	20.9944	22.3843	1.3900
28	3.423	0.0401	0.0206	0.1349	0.2395	20.2886	19.1309	1.1576
29	5.591	0.0371	0.0176	0.1597	0.3125	21.0333	21.4270	0.3937
30	5.717	0.0420	0.0198	0.1807	0.3580	20.9265	21.7502	0.8237

APPENDIX III

Scatter plots of measured versus predicted leaf area index (LAI) for the best vegetation indices calculated from VNIR reflectance spectra. The dashed lines show the optimal 1 on 1 fit, the dotted lines show the predicted fit.

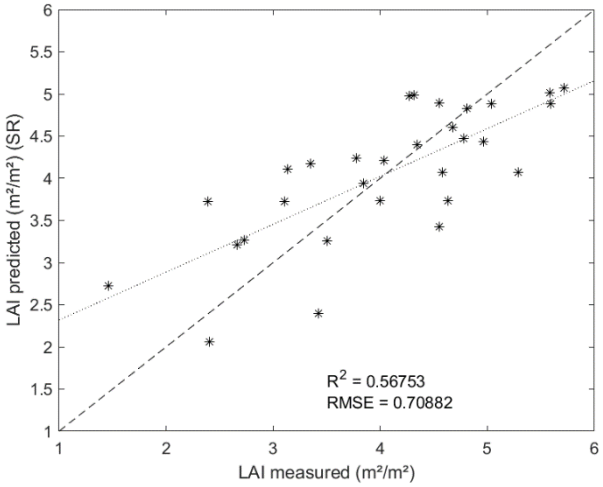

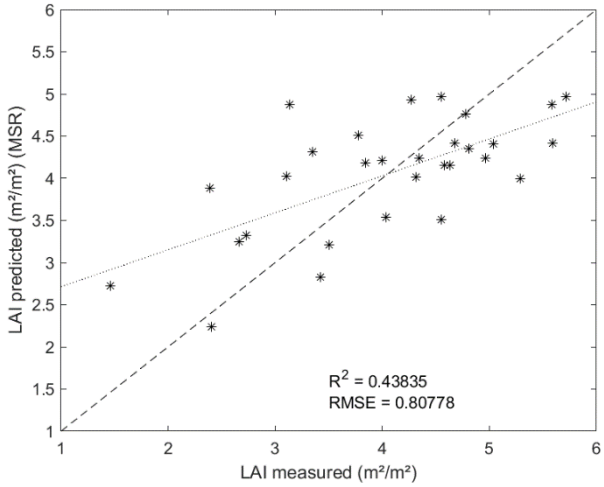

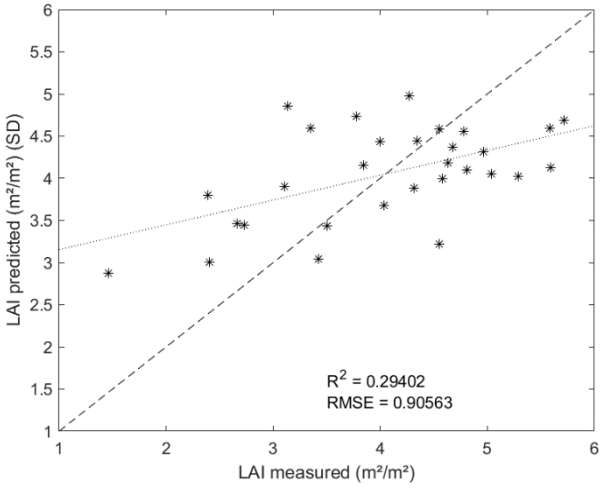

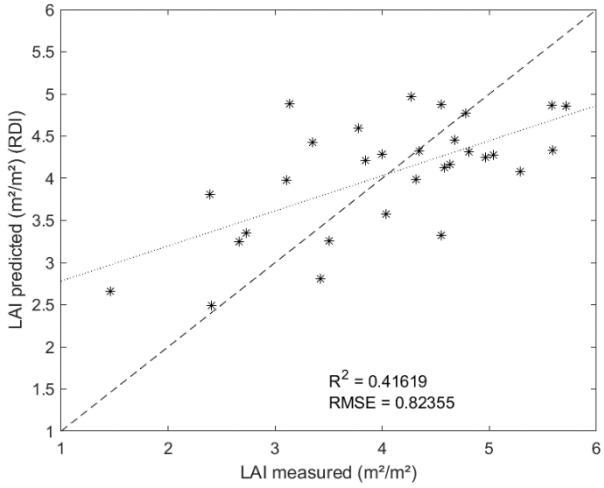

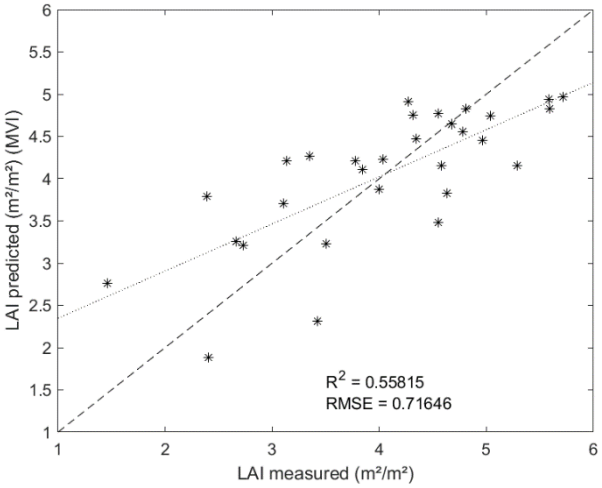
LAI predicted (m²/m²) (MVI)
LAI measured (m²/m²)
R2 = 0.55815
RMSE = 0.71646

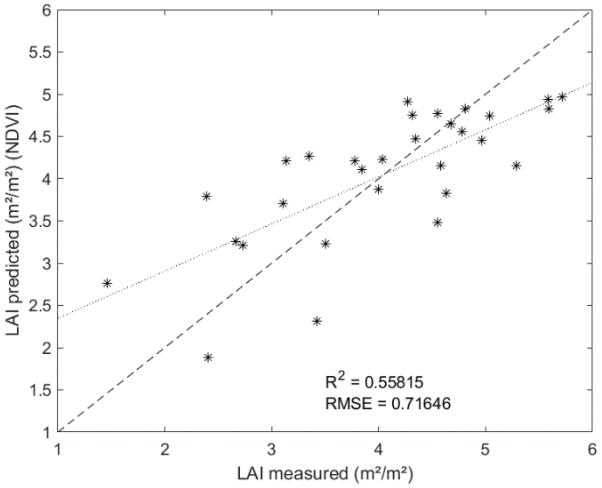
LAI predicted (m²/m²) (NDVI)
LAI measured (m²/m²)
R2 = 0.55815
RMSE = 0.71646

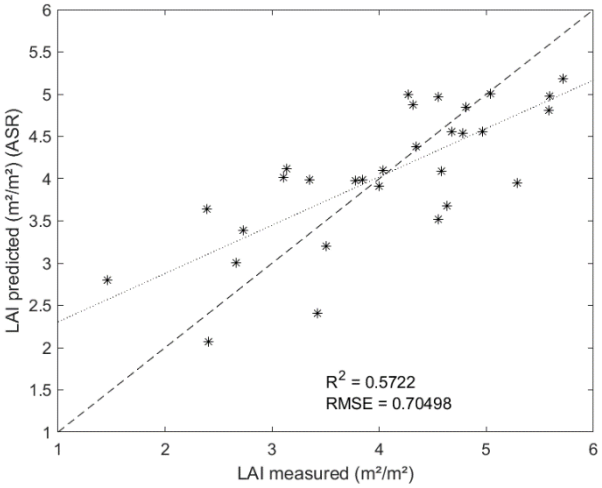
LAI predicted (m²/m²) (ASR)
LAI measured (m²/m²)
R2 = 0.5722
RMSE = 0.70498

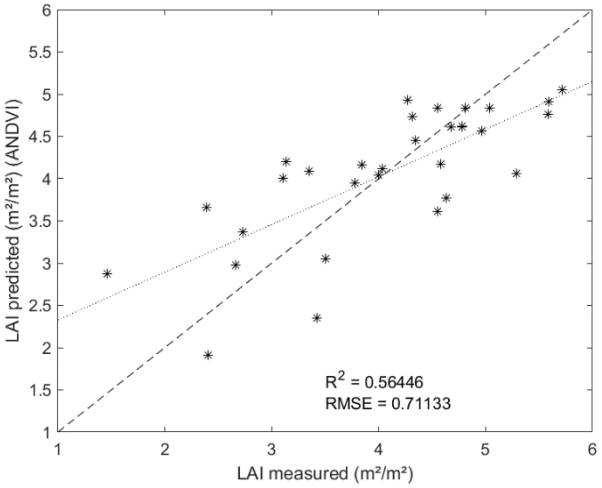
LAI predicted (m²/m²) (ANDVI)
LAI measured (m²/m²)
R2 = 0.56446
RMSE = 0.71133

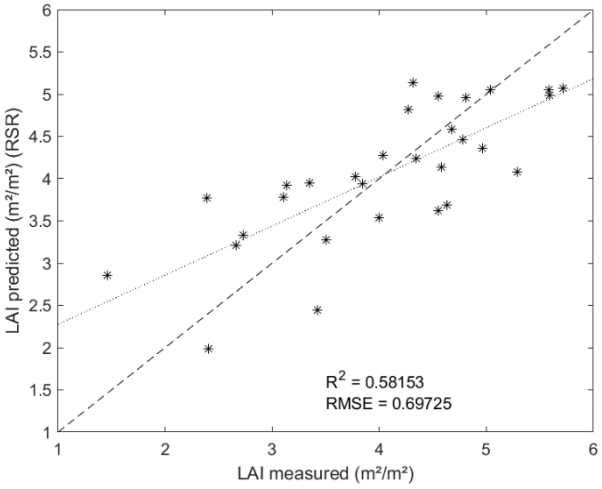
LAI predicted (m²/m²) (RSR)
LAI measured (m²/m²)
R2 = 0.58153
RMSE = 0.69725

APPENDIX IV

Scatter plots of measured versus predicted leaf area index (LAI) for the best vegetation indices calculated from VNIR reflectance spectra and land surface temperature (LST) for the flight altitudes of 85 m (LST_{85}) and 120 m (LST_{120}). The dashed lines show the optimal 1 on 1 fit, the dotted lines show the predicted fit.

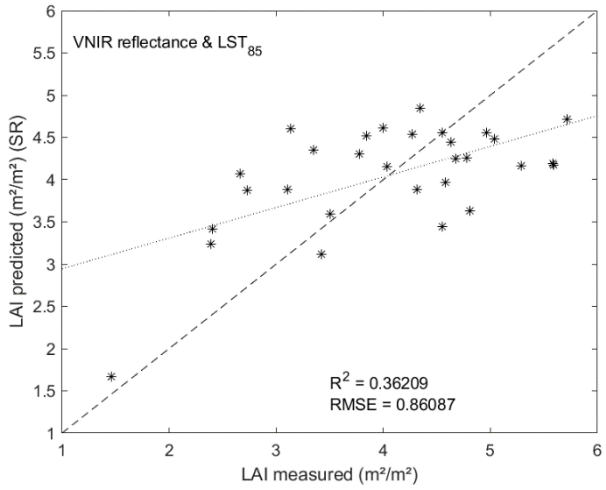

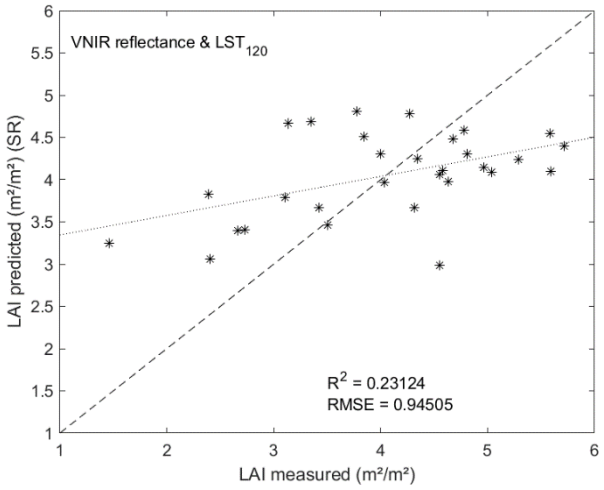

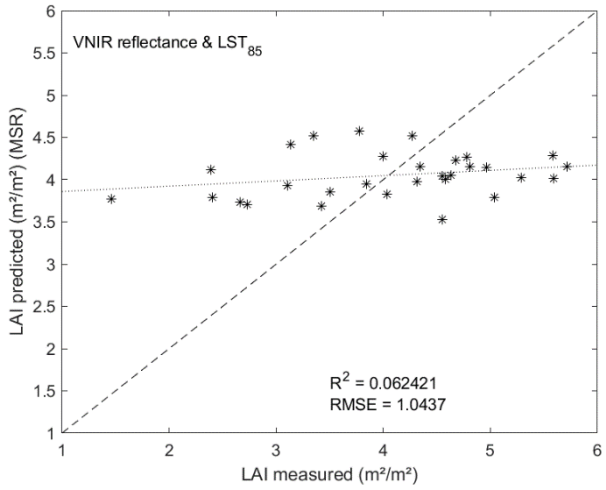

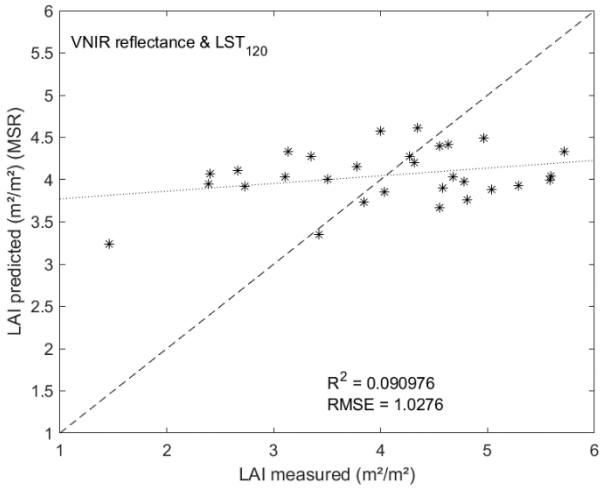

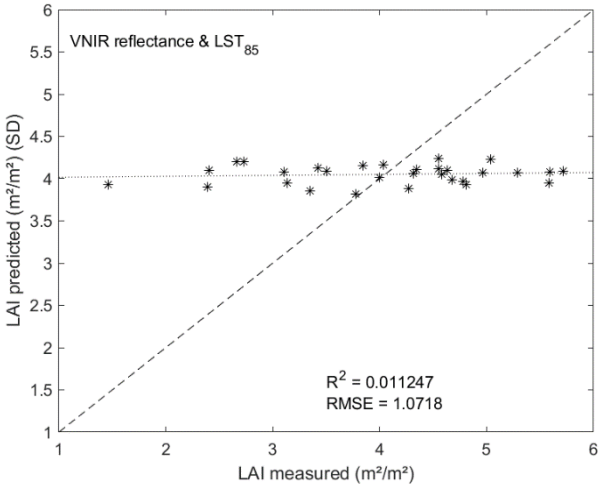
VNIR reflectance & LST85
LAI predicted (m²/m²) (SD)
LAI measured (m²/m²)
R2 = 0.011247
RMSE = 1.0718

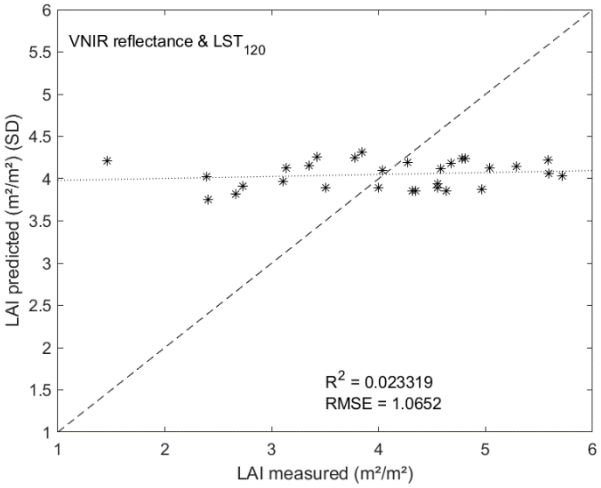
VNIR reflectance & LST120
LAI predicted (m²/m²) (SD)
LAI measured (m²/m²)
R2 = 0.023319
RMSE = 1.0652

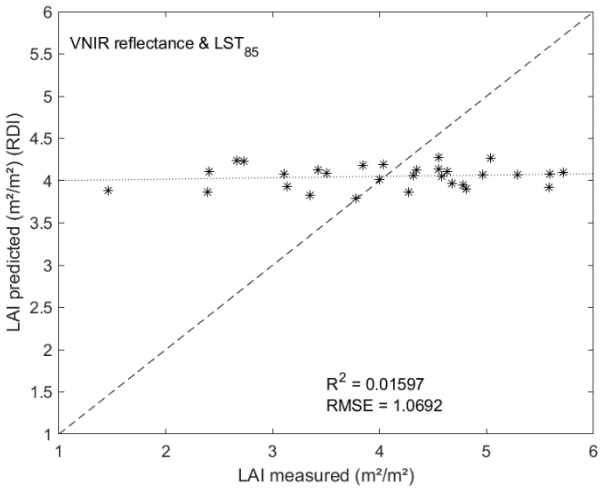
VNIR reflectance & LST85
LAI predicted (m²/m²) (RDI)
LAI measured (m²/m²)
R2 = 0.01597
RMSE = 1.0692

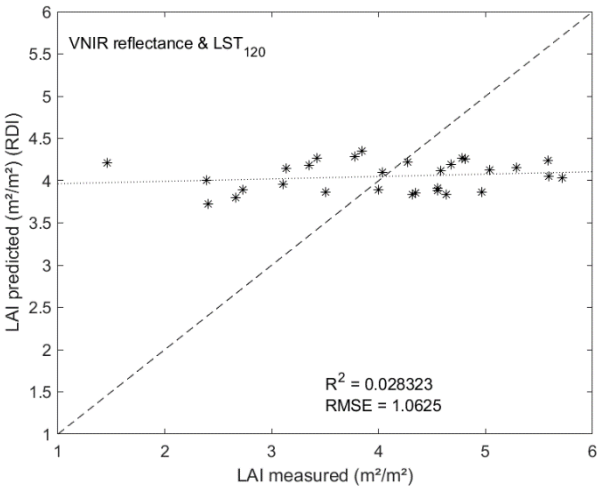
VNIR reflectance & LST120
LAI predicted (m²/m²) (RDI)
LAI measured (m²/m²)
R2 = 0.028323
RMSE = 1.0625

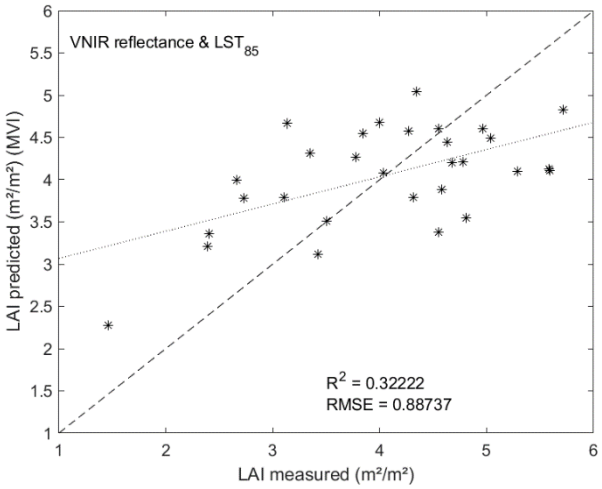
VNIR reflectance & LST85
LAI predicted (m²/m²) (MVI)
LAI measured (m²/m²)
R2 = 0.32222
RMSE = 0.88737

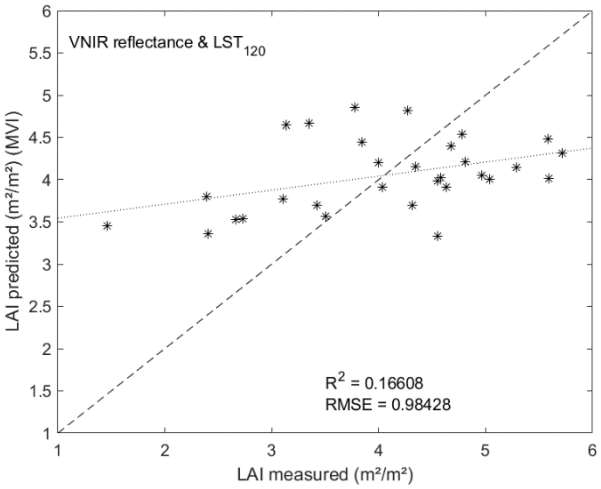
VNIR reflectance & LST120
LAI predicted (m²/m²) (MVI)
LAI measured (m²/m²)
R2 = 0.16608
RMSE = 0.98428

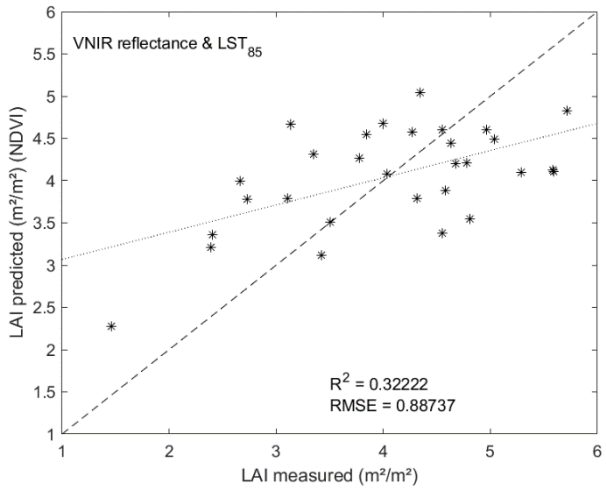
VNIR reflectance & LST85
LAI predicted (m²/m²) (NDVI)
LAI measured (m²/m²)
R2 = 0.32222
RMSE = 0.88737

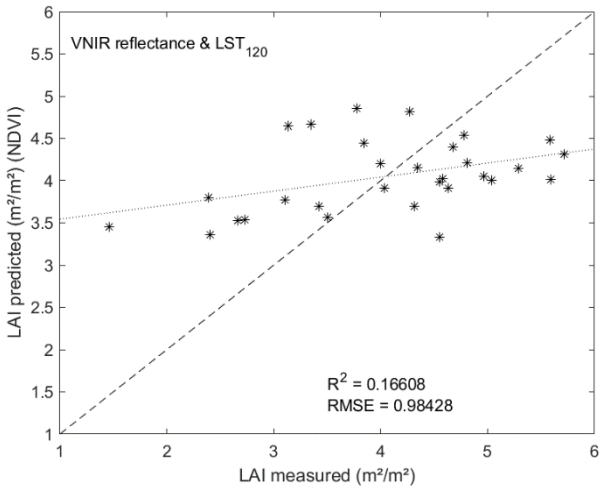
VNIR reflectance & LST120
LAI predicted (m²/m²) (NDVI)
LAI measured (m²/m²)
R2 = 0.16608
RMSE = 0.98428

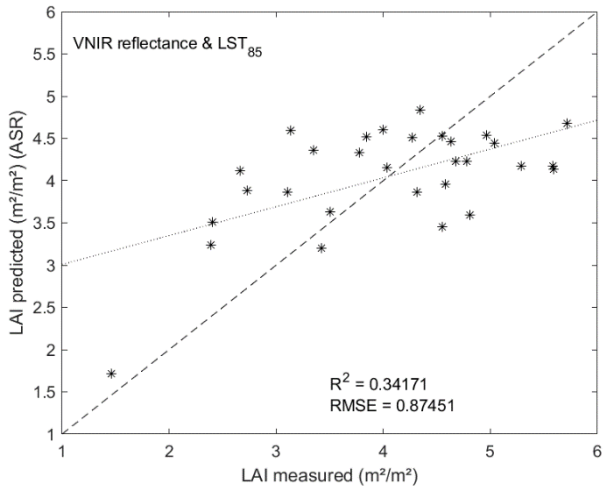
VNIR reflectance & LST85
LAI predicted (m²/m²) (ASR)
LAI measured (m²/m²)
R2 = 0.34171
RMSE = 0.87451

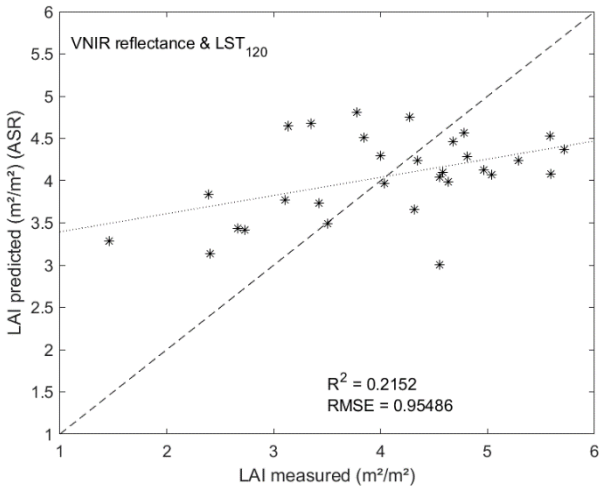
VNIR reflectance & LST120
LAI predicted (m²/m²) (ASR)
LAI measured (m²/m²)
R2 = 0.2152
RMSE = 0.95486

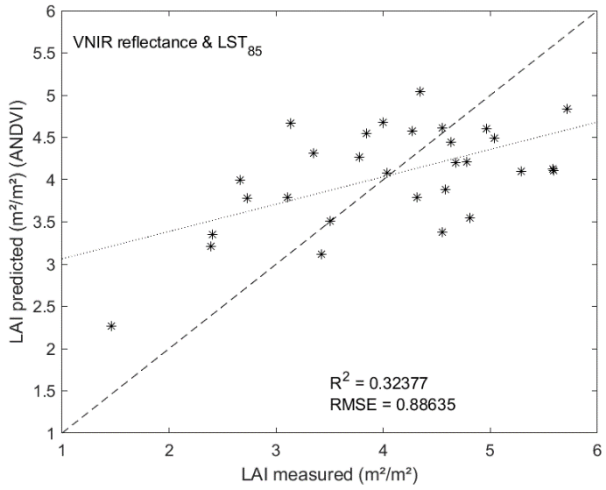
VNIR reflectance & LST85
LAI predicted (m²/m²) (ANDVI)
LAI measured (m²/m²)
R2 = 0.32377
RMSE = 0.88635

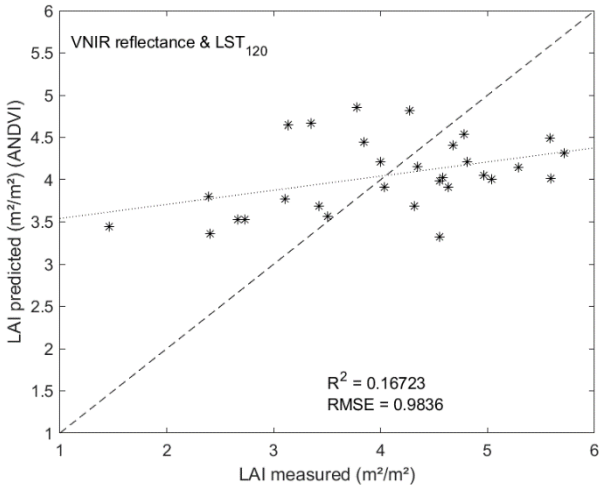
VNIR reflectance & LST120
LAI predicted (m²/m²) (ANDVI)
LAI measured (m²/m²)
R2 = 0.16723
RMSE = 0.9836

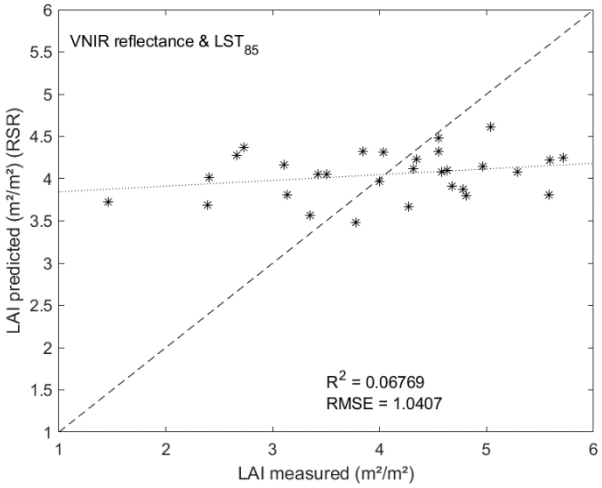
VNIR reflectance & LST85
LAI predicted (m²/m²) (RSR)
LAI measured (m²/m²)
R2 = 0.06769
RMSE = 1.0407

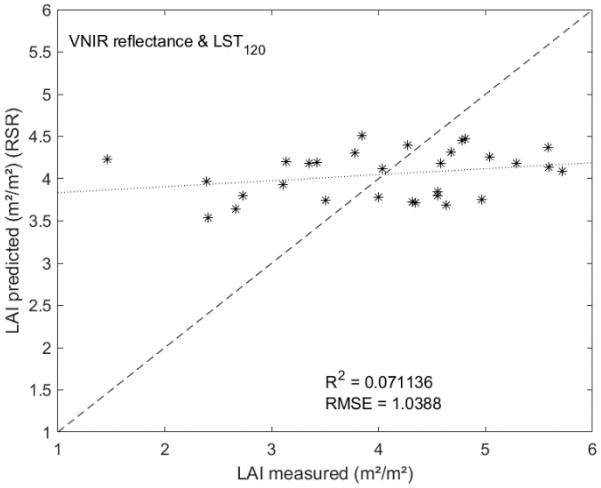
VNIR reflectance & LST120
LAI predicted (m²/m²) (RSR)
LAI measured (m²/m²)
R2 = 0.071136
RMSE = 1.0388

APPENDIX V

Scatter plots of measured versus predicted leaf area index (LAI) for the best vegetation indices calculated from VNIR reflectance spectra and land surface emissivity (LSE) calculated using different approaches (section 2.3.3): LSE_{LICOR} and LSE_{CHM}. The dashed lines show the optimal 1 on 1 fit, the dotted lines show the predicted fit.

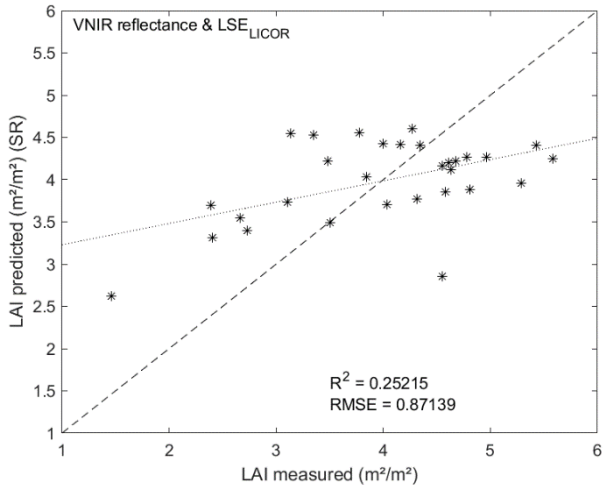

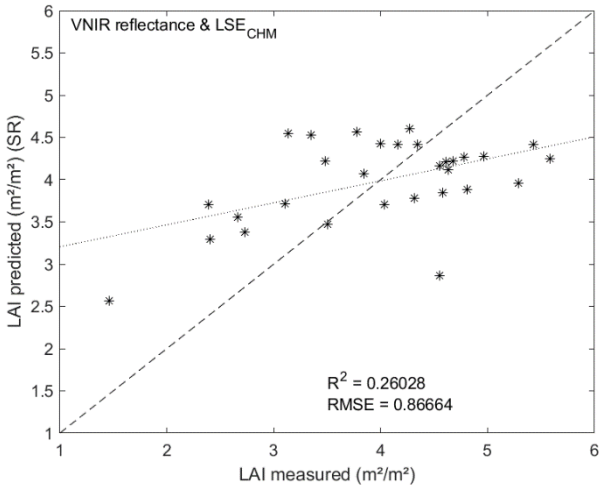

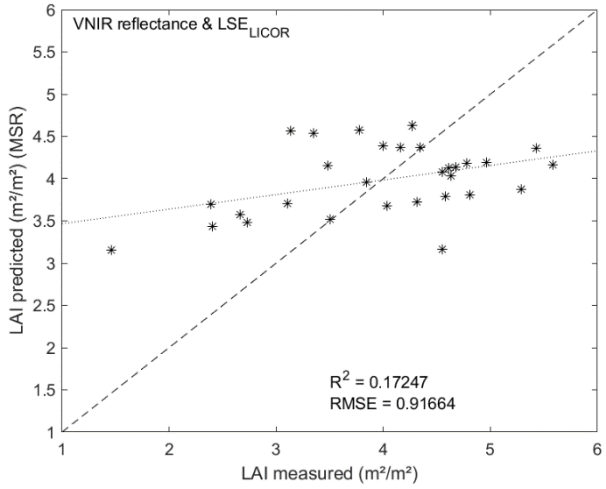

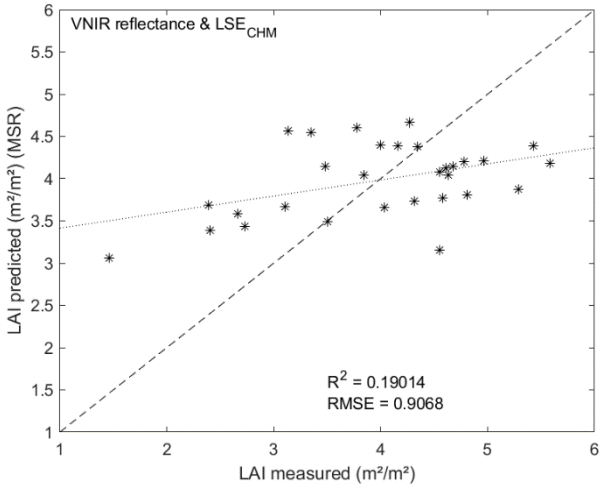

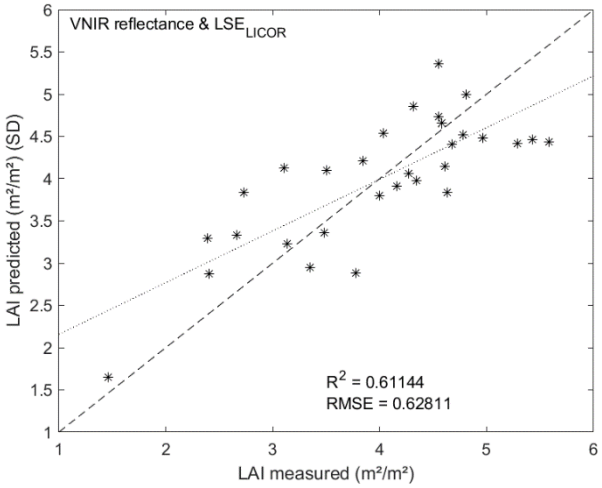
VNIR reflectance & LSE$_{LICOR}$
LAI predicted (m²/m²) (SD)
LAI measured (m²/m²)
R^2 = 0.61144
RMSE = 0.62811

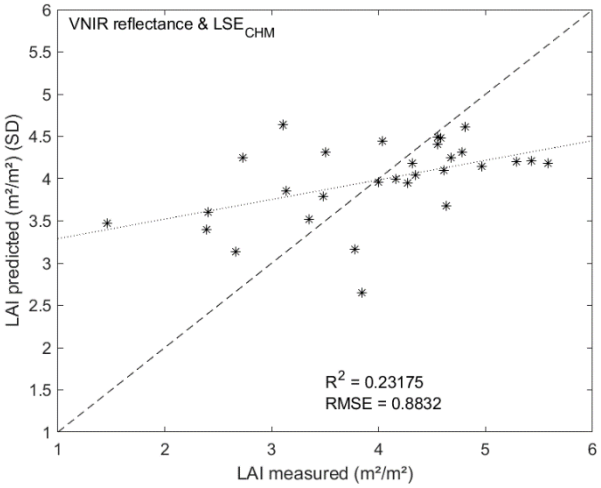
VNIR reflectance & LSE$_{CHM}$
LAI predicted (m²/m²) (SD)
LAI measured (m²/m²)
R^2 = 0.23175
RMSE = 0.8832

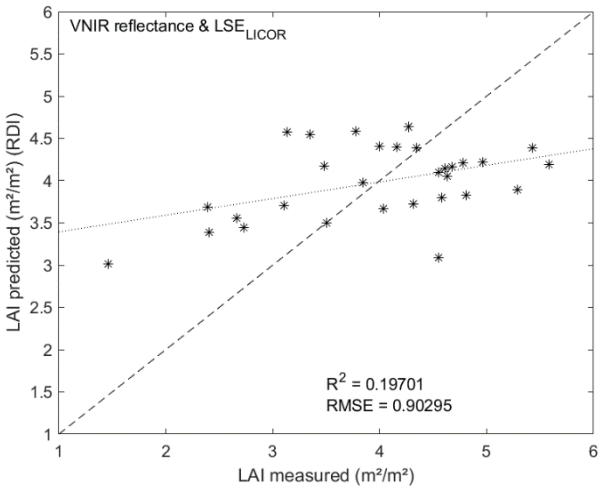
VNIR reflectance & LSE$_{LICOR}$
LAI predicted (m²/m²) (RDI)
LAI measured (m²/m²)
R^2 = 0.19701
RMSE = 0.90295

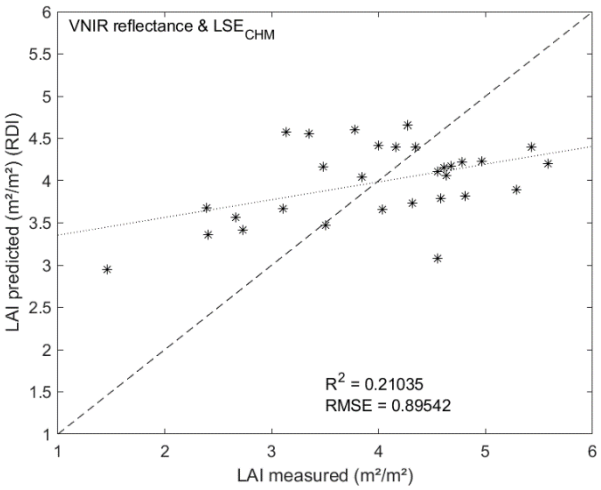
VNIR reflectance & LSE$_{CHM}$
LAI predicted (m²/m²) (RDI)
LAI measured (m²/m²)
R^2 = 0.21035
RMSE = 0.89542

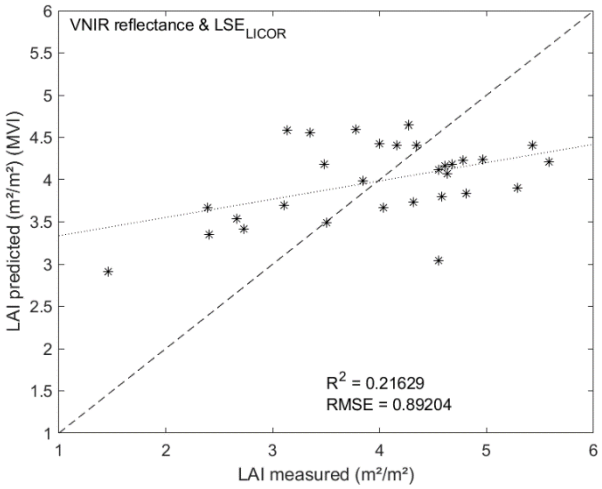
VNIR reflectance & LSE$_{LICOR}$
LAI predicted (m²/m²) (MVI)
LAI measured (m²/m²)
R^2 = 0.21629
RMSE = 0.89204

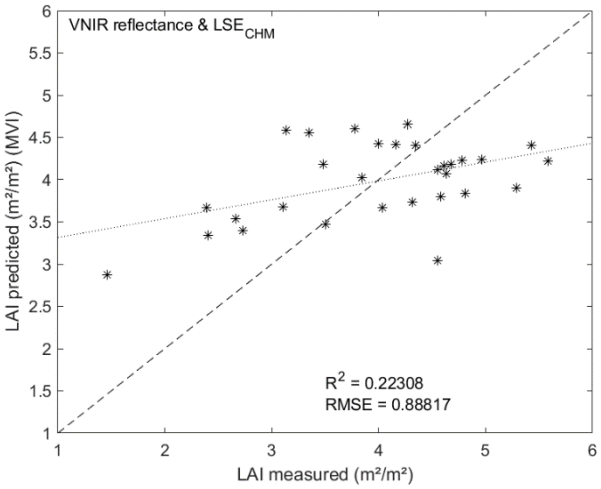
VNIR reflectance & LSE$_{CHM}$
LAI predicted (m²/m²) (MVI)
LAI measured (m²/m²)
R^2 = 0.22308
RMSE = 0.88817

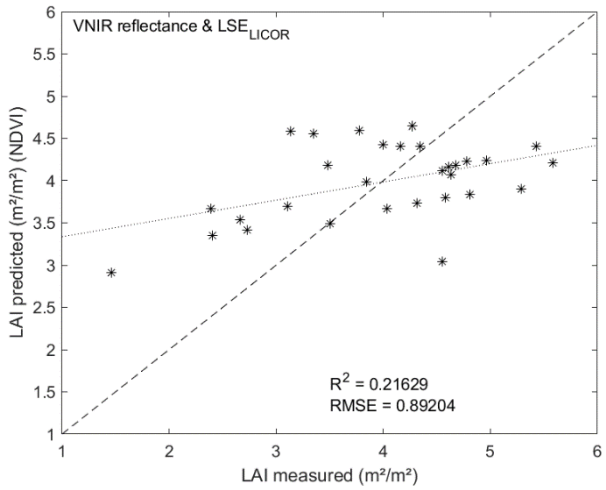
VNIR reflectance & LSE$_{LICOR}$
LAI predicted (m²/m²) (NDVI)
LAI measured (m²/m²)
R^2 = 0.21629
RMSE = 0.89204

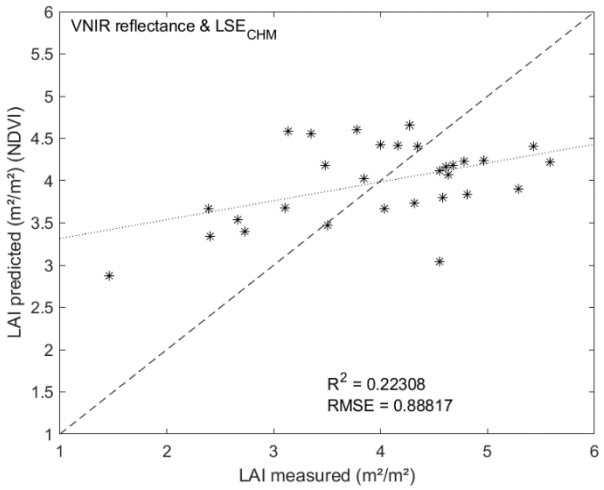
VNIR reflectance & LSE$_{CHM}$
LAI predicted (m²/m²) (NDVI)
LAI measured (m²/m²)
R^2 = 0.22308
RMSE = 0.88817

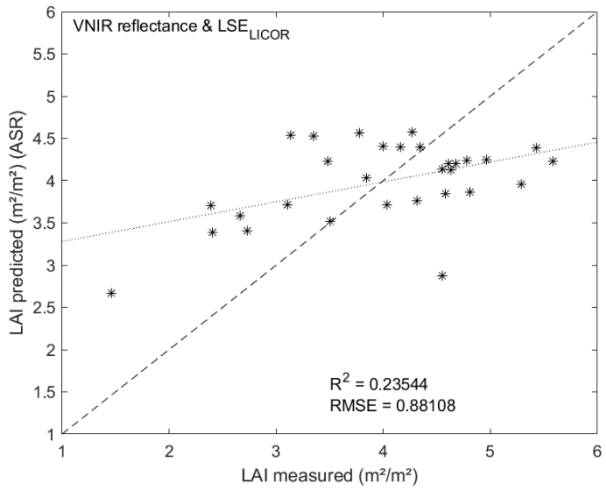
VNIR reflectance & LSE$_{LICOR}$
LAI predicted (m²/m²) (ASR)
LAI measured (m²/m²)
R^2 = 0.23544
RMSE = 0.88108

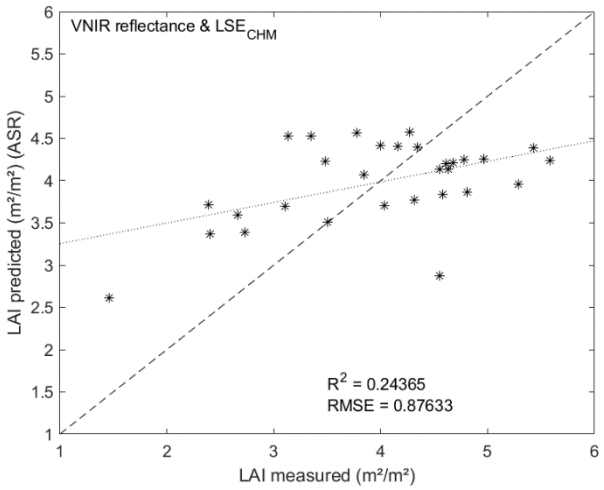
VNIR reflectance & LSE$_{CHM}$
LAI predicted (m²/m²) (ASR)
LAI measured (m²/m²)
R^2 = 0.24365
RMSE = 0.87633

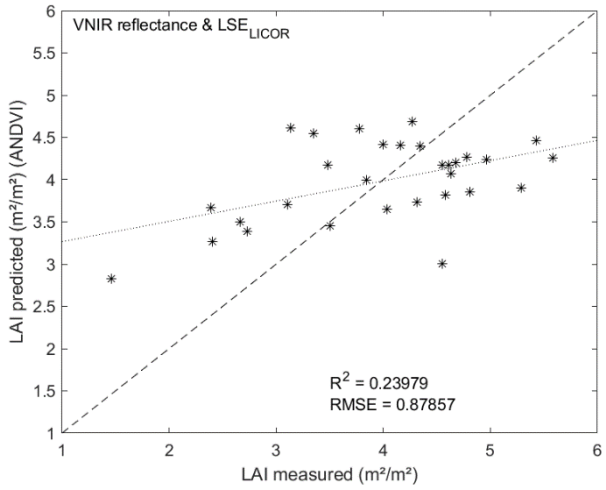
VNIR reflectance & LSE$_{LICOR}$
LAI predicted (m²/m²) (ANDVI)
LAI measured (m²/m²)
R^2 = 0.23979
RMSE = 0.87857

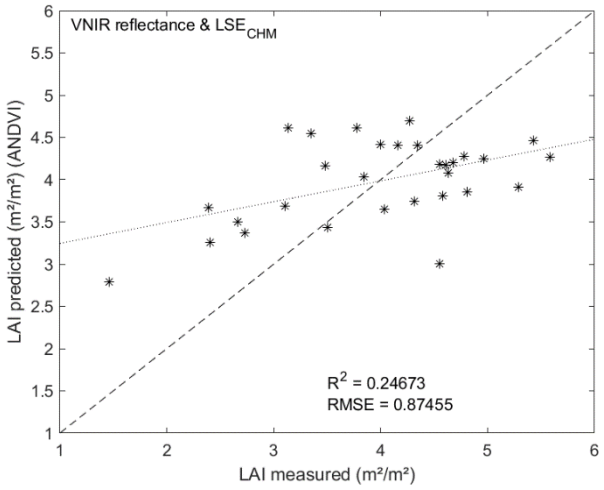
VNIR reflectance & LSE$_{CHM}$
LAI predicted (m²/m²) (ANDVI)
LAI measured (m²/m²)
R^2 = 0.24673
RMSE = 0.87455

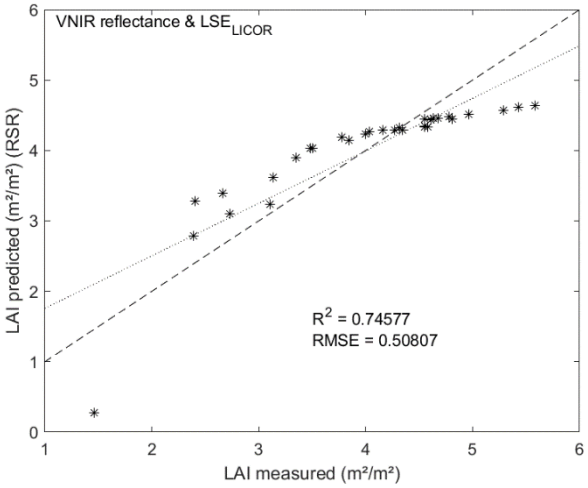
VNIR reflectance & LSE$_{LICOR}$
R^2 = 0.74577
RMSE = 0.50807
LAI predicted (m²/m²) (RSR)
LAI measured (m²/m²)

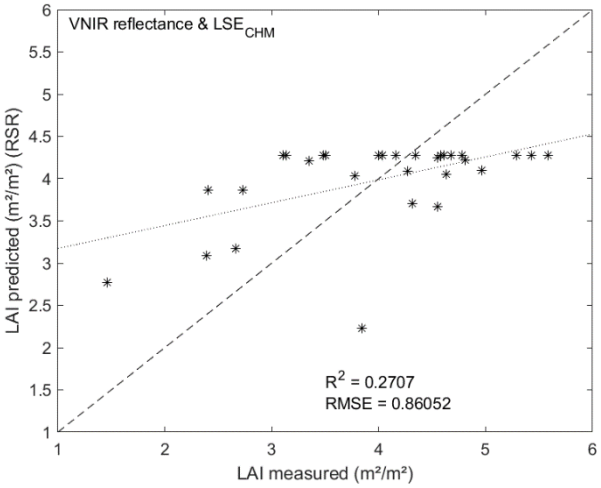
VNIR reflectance & LSE$_{CHM}$
R^2 = 0.2707
RMSE = 0.86052
LAI predicted (m²/m²) (RSR)
LAI measured (m²/m²)